

40 development of the MCT shear zone due to imbrication of distinct rock packages. Greater
41 Himalayan Crystalline garnets experienced higher-grade conditions that make extracting its P-T
42 conditions and paths a challenge. Lesser Himalayan garnets appear to behave as closed systems
43 and are ideally suited for thermodynamic approaches.

44 **1 Introduction**

45 Nineteenth-century geologists studying the Himalayas perceived an anomalous geologic
46 relationship that appeared to contradict two commonly accepted principles: the oldest rocks in a
47 sedimentary succession are found at the base of the pile, and metamorphosed strata are older than
48 unmetamorphosed. The Main Central Thrust (MCT), located at the base of the Himalayan break
49 in slope, places lower-grade Lesser Himalayan Formation (LHF) metasediments beneath high-
50 grade gneisses of the Greater Himalayan Crystallines (GHC) (Figure 1 and Figure 2).
51 Exploration of the Himal Pradesh region in northern India surprised the pioneering geologists
52 (Medicott, 1864; Oldham, 1883; Middlemiss, 1887) who saw the highest-grade, and thus
53 supposedly oldest rocks, form the tallest peaks:

54 "Now the belief which is at present so rapidly gaining ground that metamorphic strata are
55 presumably older than unmetamorphosed strata makes one at first glance assume the strong
56 probability in favor of the inner schistose series [Greater Himalayan Crystallines] being of
57 much greater age than the outer zone of formations [Lesser Himalaya]. But no sooner has this
58 a priori probability obtained a firm hold of the mind than a rude shock is given to it by the
59 discovery that at every point round the schistose area the Outer formations appear to dip
60 towards and under the schistose series at steep angles (50°-60°), whilst the schistose series
61 itself is disposed apparently...upon the top of the Outer Formations, and culminating in a
62 capping of gneissose rock on the summit of Kalogarhi mountain, the highest point in the
63 neighborhood (Middlemiss, 1887)."

64 The recognition of widespread thrusting within the Himalaya was largely based on the
65 observations (von Loczy, 1907; Pilgrim & West, 1928; Auden, 1937; Heim and Gansser, 1939)
66 and the orogen's "inverted metamorphism," an increase in metamorphic intensity towards higher
67 structural levels, appeared resolved by invoking compressional/contractual tectonics and the
68 thrusting of the GHC unit on top of the LHF. However, future studies indicated that the kyanite
69 isograd remained unbroken across the MCT, and its footwall is characterized by an inverted
70 geotherm (Figure 3) (Ray, 1947; Gansser, 1964; LeFort, 1975; Pêcher, 1989; England et al.,
71 1992). The idea of Himalayan inverted metamorphism reemerged but was relocated to the MCT
72 footwall.

73 Inverted metamorphic gradients suggest the presence of wholly overturned strata or heat
74 sources that counteract the influence of the asthenosphere (e.g., England & Molnar, 1993;
75 Jamieson et al., 1996; Grasemann & Vannay, 1999; Kidder et al., 2013). The cause of the
76 phenomenon has implications for establishing mechanisms of heat transfer within collisional
77 belts and the role of heat sources, such as shear heating in fault zones, heat advection by
78 magmas, radiogenic heating, and asthenospheric input. Inverted metamorphism has long been
79 associated with areas of extensive thrust faulting, where heat is thought to flow from a hot upper
80 plate to a colder lower plate (Ernst, 1973; Graham & England, 1976; Spear et al., 1995). Some
81 models of Himalayan orogenesis link the apparently anomalous geothermal gradient spatially
82 and temporally with motion along the MCT, whereas others suggest a juxtaposition of previously

83 metamorphosed sequences (Searle & Rex, 1989; Harrison et al., 1999; Hodges, 2000; Dasgupta
84 et al., 2004; Larson et al., 2015).

85 The MCT has accommodated a significant amount of Indo-Asian convergence (e.g.,
86 Schelling & Arita, 1991; Yin & Harrison, 2000; Yin, 2006; Tobgay et al., 2012; Roberts et al.,
87 2020), but other large-scale structures, including crustal-scale strike-slip faults to the north,
88 active thrusts to the south, and the Main Himalayan Thrust (MHT) decollement compete for
89 strain accommodation (Figure 2). The MCT has long been thought to be presently quiescent (Ye
90 et al., 1981; Ni & Barazangi, 1984; Schelling & Arita, 1991; England et al., 1992). However,
91 some earthquakes, like the 2015 Nepal (Gorkha) and 1991 Uttarkashi (Garhwal) events,
92 challenge the notion, as their epicenters and epicenters of their aftershocks are modeled to zones
93 within the LHF (Thakur & Kumar, 1994; Jain & Chander, 1995; Kayal, 1996; Gupta et al., 2015;
94 Bai et al., 2016; Catlos et al., 2020). The MCT has also been linked to the generation of
95 numerous geologic elements that characterize the Himalayan range, including hanging wall
96 anatectic granitoids and crustal-scale extension found in association with the GHC (e.g., Burg et
97 al., 1984; Valdiya, 1988; Burchfiel et al., 1992; Harrison et al., 1997; Kawakami et al., 2019).

98 Studies of the MCT hanging wall indicate the unit has discontinuities possibly related to
99 internal structures (e.g., western Nepal, Carosi et al., 2010; Montomoli et al., 2013; Braden et al.,
100 2017; central Nepal, Cottle et al., 2015; Wang et al., 2013; 2016; Rapa et al., 2018; Larson et al.,
101 2015; Sikkim, Chakraborty et al., 2019; NW India, Iaccarino et al., 2020; Benetti et al., 2021; see
102 discussions in Mukherjee et al., 2012; Larson et al., 2013; Montomoli et al., 2015). The nature of
103 these cryptic discontinuities is unclear and could be due to unmapped faults or shear zones or
104 inheritance of pre-existing basement structures (e.g., Cottle et al., 2015). Their presence
105 enhances the complexity of the Himalayan orogenic system as their activity could have
106 significantly disrupted geotherms within the GHC core during its exhumation. This is a scenario
107 that is not accounted for in the channel flow model for the extrusion of the Himalayan core (e.g.,
108 Benetti et al., 2021; Maiti & Mandal, 2021). Understanding when Himalayan fault systems were
109 active is critical for deciphering the processes involved during convergence.

110 The metamorphic history of the Himalayas has been the focus of sustained attention for
111 almost seventy-five years (e.g., Ray, 1947). Garnet-bearing assemblages have long been used to
112 test hypotheses proposed for the origin of MCT inverted metamorphism, understand the slip
113 history of the MCT and the dynamics of Himalayan convergence. The focus includes generating
114 the peak pressure-temperature (P-T) conditions and paths that rocks followed as they were
115 metamorphosed during Indo-Asia collision (e.g., Brunel and Kienast, 1986; Hodges et al., 1988;
116 Hodges and Silverberg, 1988; Hubbard, 1989; Inger and Harris, 1992; Hodges et al., 1993;
117 Metcalfe, 1993; Pognante and Benna, 1993; Kaneko, 1995; Macfarlane, 1995; Coleman, 1996;
118 Vannay and Hodges, 1996; Vannay and Grasemann, 1998; Manickavasagam et al., 1999; Catlos
119 et al., 2001; Kohn et al., 2001; Kohn, 2008; Phukon et al., 2019; Waters, 2019; Iaccarino et al.,
120 2020; Catlos et al., 2018; 2020).

121 As a universal outcome, models for the development of the Himalayas predict the P-T
122 paths that rocks follow as they track the conditions they experienced during displacement.
123 Common approaches to generate Himalayan P-T paths have included connecting peak
124 metamorphic conditions of individual rocks, inferring from mineral assemblages,
125 pseudosections, or Gibbs method thermodynamic modeling. Some rocks yield problematic P-T
126 estimates based on (1) a lack of evidence of phases in equilibrium among phases, (2) the
127 application of barometers to inappropriate (uncalibrated) mineral compositions, and (3)

128 calculated conditions that appear at odds to observed mineral assemblages and structural data
129 (e.g., Kohn & Spear, 2000; Kohn, 2008). P-T paths and absolute peak P-T conditions may not be
130 diagnostic of tectonic processes involved (e.g., Gervais & Brown, 2011). Low-resolution P-T
131 paths can be limited in their ability to test ideas regarding lithospheric response to perturbations,
132 including motion within fault zones. However, this type of information can be used to
133 supplement other data, such as the timing of deformation or strain recorded in microstructures
134 (see Kohn, 2016; Rolfo et al., 2014).

135 This paper has two goals. The first is to review the geological framework of the
136 Himalayas with a focus on the protolith of its metamorphosed assemblages. The second is to
137 describe and apply particular thermobarometric approaches to decipher the metamorphic history
138 of garnet-bearing rocks collected from the central portion of the range across the MCT using data
139 published in the literature (Darondi Khola, Figure 3, Figure 4, Figure 5) (Kohn et al., 2001). A
140 range of approaches are available to obtain P-T and time garnet growth (P-T-t data) (see review
141 by Waters, 2019). The Darondi Khola case study compares conventional and isopleth
142 thermobarometry in terms of their outcomes and insights and presents new P-T paths from
143 metamorphosed garnet-bearing rocks using previously collected data. Garnet-bearing pelitic
144 assemblages exposed in units across the Himalayas contain information regarding their history
145 that can be extracted and applied to test models developed to decipher the crustal response
146 during orogeny.

147 **2 Geological Background**

148 The Himalayan arc extends ~2400 km from Nanga Parbat (8138 m) in the west to
149 Namche Barwa (7756 m) in the east (e.g., Le Fort, 1996) (Figure 1 and Figure 2). This region
150 includes the independent kingdoms of Nepal and Bhutan and parts of Pakistan, India, and China.
151 The orogen forms a sharp transition between the average ~5 km-high, arid Tibetan plateau and
152 the warmer, wetter Indian lowlands and is comprised of roughly parallel, crustal-scale fault
153 systems that bound distinctive lithologic units along strike (DiPietro & Pogue, 2004; Yin, 2006).
154 These units have Indian affinity and experienced variable degrees of metamorphism before their
155 assembly with Asia.

156 **2.1 Geological framework before collision**

157 The Indian subcontinent initiates rifting from other continents and fragments associated
158 with Gondwana during the Early Cretaceous (140-130 Ma, e.g., Scotese et al., 1988; Jadoul et
159 al., 1998; Hu et al., 2010). Evidence for Early Cretaceous rift- and plume-related alkaline and
160 basaltic volcanism exists within the LHF, which extends the entire length of the Himalayas, and
161 is the oldest stratigraphically lowest unit (e.g., Sakai et al., 2013; Bhandari et al., 2019). The
162 LHF is considered the MCT footwall and Main Boundary Thrust (MBT) sheet (Figure 1 and
163 Figure 2) (Dey et al., 2020). It is mainly comprised of Paleoproterozoic Gondwana-associated
164 sediments that experienced deposition and granite intrusion centered around 1800 Ma (e.g.,
165 Trivedi et al., 1984; Tripathi & Singh, 1987; Parrish & Hodges, 1996; Miller et al., 2000;
166 DeCelles et al., 2004; Kohn et al., 2010; Martin et al., 2011; McKenzie et al., 2011; Long et al.,
167 2011; Sakai et al., 2013; Khanal et al., 2014; Mandal et al., 2016). The depositional environment
168 is a passive-margin, shallow-water coastal, fluvial, volcanoclastic (e.g., Parrish & Hodges, 1996;
169 Ahmad et al., 1999; Martin et al., 2011; Sakai et al., 2013; Bhandari et al., 2019). However, the
170 lower section of the LHF may have formed in a continental arc on the northern margin of the
171 Indian plate (Kohn et al., 2010; Mandal et al., 2016). In some locations, rift-related alkaline

172 trachytic lava and pillow-bearing volcanic rocks are interbedded with pebble conglomerates and
173 black shales, and signatures of significant asthenosphere upwelling are evident using
174 geochemical proxies (e.g., Ahmad et al., 1999; Larson et al., 2019; Bhandari et al., 2019).

175 The stratigraphic classification of the Proterozoic succession of Lesser Himalaya is yet to
176 be defined following the Code of Stratigraphic Nomenclature, and orogen-scale correlations
177 along strike are hindered by uncertainties (Myrow et al., 2006; Long et al., 2011; Mandal et al.,
178 2016; Dey et al., 2020). Sedimentation was long-lasting, but a lack of fossiliferous assemblages
179 makes correlating specific units problematic (Upreti, 1999; Martin et al., 2011; Long et al.,
180 2011). Detrital zircon geochronology and stable isotopic analysis of suitable assemblages assist
181 in this regard (e.g., Long et al., 2011; Martin et al., 2011; Sakai et al., 2013). A series of augen
182 gneisses (the Melung Salleri or Phaplu Augen Gneiss of eastern Nepal and NW India, the Ulleri
183 of central Nepal, or Chainpurplay in western Nepal) distinguish different levels of the MCT
184 shear zone and LHF stratigraphy (Figure 3, Figure 4, Figure 5) (Kohn et al., 2010; Dyck et al.,
185 2019; Jharendra & Paudyal, 2019). These gneisses have ages from 2.2 Ga to 900 Ma (e.g., Le
186 Fort & Rai, 1999; DeCelles et al., 2000; Catlos et al., 2002; Kohn et al., 2010) and define the
187 base of the MCT shear zone in some interpretations. A Permian-Cambrian unconformity is
188 recognized in NW India, Nepal, and Bhutan (e.g., Bhargava et al., 2011; Martin et al., 2011;
189 Long et al., 2011). Some have related its presence and Cambro-Ordovician granites found in
190 GHC and LHF units to a pre-Tertiary orogeny (Gehrels et al., 2003; 2006; Cawood et al., 2007;
191 Bhargava et al., 2011).

192 The GHC protolith is a clastic sedimentary sequence intruded by Cambro-Ordovician
193 granitoids (e.g., Trivedi et al., 1984; Bhargava & Bassi, 1994; Parrish & Hodges, 1996; Upreti &
194 Le Fort, 1999; DeCelles et al., 2004; Dyck et al., 2019). The depositional age is bracketed
195 between the age of the youngest detrital zircons (~800-600 Ma) and granite intrusions (~500-460
196 Ma) (Ahmad et al., 2000; DeCelles et al., 2000; DeCelles et al., 2004; Martin et al., 2005; Dyck
197 et al., 2019). Whole-rock Nd isotopes distinguish GHC [$\epsilon\text{Nd}(0)$ -19 to -12, average -16] from
198 LHF affinities [$\epsilon\text{Nd}(0)$ -20 to -26, average -21.5] (Robinson et al., 2001; Martin et al., 2005). The
199 GHC detrital zircons may have originated from the East African portion of the Pan-African
200 orogeny (Arabian-Nubian Shield), uplifted during the Neoproterozoic (DeCelles et al., 2000;
201 2004), or from the late Mesoproterozoic terranes of Western Australia and East Antarctica
202 (Circum-East Antarctic Orogen, Upreti & Yoshida, 2005; Yoshida & Upreti, 2006). The GHC
203 has been modeled as unconformably deposited on the LHF (Parrish & Hodges, 1996) or
204 tectonically juxtaposed (Upreti & Le Fort, 1999; DeCelles et al., 2000). The similarity in
205 Cambrian ages between the LHF and GHC suggest they may be part of a shared depositional
206 environment, with the LHF as proximal and the GHC as distal (Brookfield, 1993; Parish &
207 Hodges, 1996; Corfield & Searle, 2000; Myrow et al., 2003; Myrow et al., 2006; Long et al.,
208 2011). Alternatively, the GHC may have been a distinct basement unit separating the LHF from
209 the Tethyan metasediments (Saxena, 1971; Aharon et al., 1987) or an exotic terrane involved in a
210 pre-Himalayan collision (DeCelles et al., 2000; Gehrels et al., 2003).

211 Tethyan sedimentary and metasedimentary rocks are bounded to the north by the Indus
212 Yarlung-Tsangpo suture zone (also Yarlung Zangbo Ophiolite Zone, Liu et al. 2010) (Gansser,
213 1964; Dewey & Bird, 1970; Burg et al., 1984; Yin et al., 1994; Quidelleur et al., 1997; Zhang et
214 al., 2004; Yin, 2006; Zhabrev et al., 2008), and to the south by the GHC or South Tibetan
215 Detachment System (STDS) (Figure 1 and Figure 2) (e.g., Makovsky & Klempnerer, 1996; Wu et
216 al., 1998; Searle, 2010; Long et al., 2017; Montomoli et al., 2017; Hughes et al., 2018; Kellett et

217 al., 2018; Long et al., 2019). The Great Counter Thrust (or the Renbu-Zedong Thrust or
 218 Himalayan Backthrust) is mapped south of the zone also works to accommodate crustal
 219 shortening (Yin et al., 1999; Yin, 2006; Aikman et al., 2008). The Tethyan unit has long been
 220 considered as a contiguous stratigraphic cover of the GHC (Bodenhausen et al., 1964; Bordet et
 221 al., 1971; Stöcklin, 1980; Garzanti & Pagni Frette, 1991; Brookfield, 1993; Liu & Einsele, 1994;
 222 Fuchs & Linner, 1995; Vannay & Steck, 1995; Garzanti, 1999; Dyck et al., 2019), and the suture
 223 zone marks the geological boundary separating rocks of Indian and Asian affinity (e.g., Gansser,
 224 1981; Yin & Harrison, 2000). In NW India, the Tethyan Formation may be in thrust contact with
 225 the LHF (Webb et al., 2007). The Tethyan Formation consists of Paleoproterozoic to Eocene
 226 Indian shelf sediments (marine, fossiliferous strata) interbedded with Paleozoic and Mesozoic
 227 volcanic assemblages (Bassoulet et al., 1980; Brookfield, 1993; Yin, 2006; Bhargava & Singh,
 228 2020). The unit has been divided into four sequences: a Proterozoic to Devonian pre-rift, a
 229 Carboniferous–Lower Jurassic rift and post-rift, Jurassic–Cretaceous passive continental margin
 230 sequence, and an uppermost Cretaceous–Eocene syn-collision sequence (Liu & Einsele, 1994;
 231 Garzanti, 1999; Yin, 2006). Tethyan Formation lithostratigraphy changes both along and
 232 perpendicular to the Himalayan orogeny (Brookfield, 1993; Yin, 2006). In some locations, the
 233 unit has undergone pre-Himalaya low-grade to greenschist facies metamorphism (e.g., Crouzet et
 234 al., 2007; Dunkl et al., 2011; Montomoli et al., 2017) and the latest Cretaceous to Paleocene
 235 sequence of the formation records the obduction of ophiolitic material (Allègre et al., 1984; Burg
 236 et al., 1987; Willems et al., 1996; Gnos et al., 1997; Makovsky et al., 1999; Aitchison et al.,
 237 2000; Ding et al., 2005).

238 **2.2 Timing of major metamorphic events and fault systems**

239 **2.2.1 Collision and metamorphism in the Tethyan Formation**

240 The Indian subcontinent moves over 60° latitude north towards Asia during the mid-
 241 Mesozoic to Eocene, closing the ancient Neo-Tethyan Ocean (e.g., Burg, 2011). The Early
 242 Cretaceous (140-130 Ma) is often cited as the time when the Indian subcontinent initiates rifting
 243 from other continents and fragments associated with Gondwana (e.g., Scotese et al., 1988; Jadoul
 244 et al., 1998; Hu et al., 2010). Remnants of Neo-Tethyan ophiolites are present across the
 245 Himalayas and provide information regarding the timing and processes involved during Indo-
 246 Asia collision and the nature of Neo-Tethyan ocean crust and upper mantle (e.g., Hébert et al.,
 247 2012; Hu et al., 2016; Catlos et al., 2019). Based on data from these ophiolites, a Late
 248 Cretaceous intra-oceanic arc has been suggested to be present within the Neo-Tethyan Ocean
 249 near the paleo-equator (e.g., Reuber, 1986; Abrajevitch et al., 2005; Metcalfe, 2009; Dai et al.,
 250 2011; Siddiqui et al., 2012; Siddiqui et al., 2017) or ~30°N (Zhu et al., 2013). The arc is recorded
 251 by the Samail (Oman), Zagros (Iran), Chagai–Raskoh (western Pakistan, southern Iran, eastern
 252 Afghanistan), Kandahar and Kohistan–Ladakh, Dazhuqu, and Zhongba arcs (Brookfield and
 253 Reynolds, 1981; Bhutani et al., 2004; Abrajevitch et al., 2005; Dai et al., 2011; Siddiqui et al.,
 254 2012; Baxter et al., 2016). Paleogeographic reconstructions of Lawver et al. (2018) restrict the
 255 location of the intra-oceanic arc to the south of the Lhasa Terrane, although others suggest the
 256 Lhasa Terrane had already accreted onto other Tibetan-related continental fragments by the Late
 257 Jurassic–Early Cretaceous (Rolland, 2002; Kapp et al., 2003, 2007; Guynn et al., 2006; Zhu et
 258 al., 2013). Alternatively, the Lhasa Terrane accreted just before the final collisional event in the
 259 Paleocene (54.9±2.3 Ma and 40.0±3.3 Ma; Yang et al., 2015; 61 Ma and ~53–48 Ma; Yuan et al.,
 260 2020). Multiple arcs, besides the Lhasa Terrane, may also have been present (e.g., Zyabrev et al.,
 261 2008). The oldest portion of the Neo-Tethyan domain is Late Triassic to Late Cretaceous (Sinha-

262 Roy, 1982; Şengör and Atayman, 2009; Cao et al., 2018) and is sometimes termed the Ceno-
263 Tethyan Ocean (Metcalf, 1999; Matsuoka et al., 2002; Wakita and Metcalfe, 2005). The
264 Yarlung-Tsangpo suture zone itself is mapped as the zone of the closure of the Ceno-Tethyan
265 Ocean (e.g., Metcalfe, 1999; 2009; 2013).

266 The timing of initial collision varies along strike of the range but is often cited as during
267 the Paleocene (Patriat & Achache, 1984; Klootwijk et al., 1992; Rowley, 1996; Yin & Harrison,
268 2000; Najman et al., 2001, 2002, 2003; Zhu et al., 2005; Ding et al., 2005; Yang et al., 2015; Hu
269 et al., 2016). Much younger constraints are also suggested (e.g., Eocene/Oligocene boundary,
270 Aitchison et al., 2007) and a division between a soft (Paleocene) and hard collision (25-20 Ma,
271 van Hinsbergen et al. 2012; see review in Parsons et al., 2020). In the hard scenario of Indo-Asia
272 collision, the Tethyan unit represents the northern extension of the Indian subcontinent
273 (Brookfield, 1993; Yin & Harrison, 2000; Myrow et al., 2003, Hughes et al., 2005; Myrow et al.,
274 2009; Myrow et al., 2015; Hughes, 2016). Others suggest the Tethyan formation may have been
275 an independent terrane in the Mesozoic (DeCelles et al., 2000; see review in Yuan et al., 2020).
276 Parsons et al. (2020) note that little progress has been made to resolve the differences between
277 models of Indo-Asia collision. Gehrels et al. (2003) indicates that ascertaining the relative
278 contributions of early Paleozoic versus Tertiary tectonism poses a significant challenge in
279 understanding the Himalayan orogen. To understand which model is relevant requires
280 understanding the metamorphic and timing history of fault systems that were active during
281 collision. The Great Counter Thrust, which bounds the upper portion of the Tethyan Formation
282 along much of its strike (Figure 1), is significantly younger than the Paleocene ages of Indo-Asia
283 collision. This structure shows activity primarily during the Miocene (20-13 Ma) across the
284 western and central Himalayas (see review in Yin, 2006).

285 Compilations regarding the Tethyan Formation's metamorphic history collected along
286 strike suggest the Tethyan sequences have experienced multiple (4-5) deformation events,
287 although the timing of these episodes is poorly constrained (Aikman et al., 2008; Dunkl et al.,
288 2011). Studies focusing on the low-grade history reveal Early Cretaceous pre-collisional
289 metamorphism (e.g., Crouzet et al., 2007; Dunkl et al., 2011). Eocene greenschist to amphibolite
290 facies metamorphism is recorded in portions of the unit and record conditions likely related to
291 the onset of collision (580-600°C, 5-8 kbar) (Dunkl et al., 2011; Catlos et al., 2020). Paleocene
292 radiometric ages related to collision are found in the Spongtang ophiolite (Figure 1) (64.3 ± 0.8
293 Ma and 42.4 ± 0.5 Ma, zircon U-Pb ages, Catlos et al., 2019) and in a Tethyan Formation garnet
294 (50.3 ± 0.6 Ma; Catlos et al., 2020). The collisional event is also recorded by eclogite, high-
295 pressure (HP) and ultra-high pressure (UHP) rocks documented within the Tethyan Formation
296 near the suture zone (e.g., Guillot et al., 2008; Laskowski et al., 2016). In some locations, HP
297 assemblages record multiple metamorphic stages (e.g., Chen et al., 2021). Oligo-Miocene anchi-
298 to epizonal metamorphism and alteration are related to crustal shortening during this time,
299 whereas rocks at the base of the unit record Miocene STDS motion and gneiss dome exhumation
300 (e.g., Dunkl et al., 2011). Oligocene- to Miocene-age contact metamorphism marks the onset of
301 the intrusion of some North Himalayan granitic bodies and gneiss domes (e.g., Guillot et al.,
302 1995, 1999; Liu et al., 2016; Gao et al., 2016; Lihter et al., 2020). The onset of the north-dipping
303 STDS and its associated imbrications (Figure 1) is often constrained to the Miocene (Carosi et
304 al., 1998, 1999a, 1999b; Searle, 1999; Sachan et al., 2010; Iaccarino et al., 2017; Long et al.,
305 2017; Montomoli et al., 2017; Kellett et al., 2018; Iaccarino et al., 2020). However, at some
306 locations, the GHC shows a transitional relationship with limestone of the Tethys sediments and
307 metamorphic grade remains unchanged across the STDS with stratigraphy and lithology

308 excluding a distinct fault boundary (e.g., Bordet et al., 1975; Stöcklin, 1980; Fuchs et al., 1988;
309 Schneider & Masch, 1993; Vannay & Steck, 1995; Cooper et al., 2012; Long et al., 2017). Long
310 et al. (2019) suggest that extensional motion associated with the STDS in Bhutan occurs both
311 within the GHC and Tethyan units.

312 **2.2.2 The GHC Eohimalayan and Neohimalayan events**

313 The GHC is mainly comprised kyanite- to sillimanite- grade gneisses intruded by High
314 Himalayan leucogranites in structurally higher levels (e.g., Upreti, 1999; Searle et al., 2006;
315 Sachan et al., 2010; Wu et al., 2020). The GHC is generally divided into different units, although
316 the assemblages that comprise its sections differ along strike (Le Fort, 1975; Myrow et al., 2003;
317 Yin, 2006). In central Nepal (Guillot, 1999), the upper Formation III consists of augen
318 orthogneisses, whereas the middle Formation II are calc-silicate gneisses and marbles, and the
319 basal Formation I are kyanite- and sillimanite-bearing metapelites, gneisses, and
320 metagreywackes with abundant quartzite. The division of the package into three units mirrors the
321 nomenclature ~250 km east (Lombardo et al., 1993; Pognante & Benna, 1993; Carosi et al.,
322 1999a), although the assemblages differ from that of central Nepal. In eastern Nepal, the upper
323 Black Gneiss is comprised of biotite-sillimanite paragneisses with metaconglomerates and
324 quartzite layers. The middle Namche Migmatite Orthogneiss contains granite-granodiorite
325 sillimanite-bearing orthogneisses. The Barun Gneiss at the base is a migmatized paragneiss with
326 minor metabasites, calc-silicate rocks, and marbles. In the Garhwal Himalaya, the Vaikrita
327 Group is the analog to the GHC (e.g., Ahmad et al., 2000). Early observations, the unit's
328 complex metamorphic history, and possibility of out-of-sequence thrusting at higher levels led
329 Stöcklin (1980) to doubt the assumption of a three-tiered, laterally-continuous,
330 tectonostratigraphic framework. More recent thermobarometric data and P-T-t paths from garnet-
331 bearing assemblages from the GHC unit indicate the unit itself has discontinuities related to
332 internal structures that overlap in age with MCT motion (Carosi et al., 2010; Montomoli et al.,
333 2013; Wang et al., 2013; Larson et al., 2015; Montomoli et al., 2015; Carosi et al., 2016; Wang
334 et al., 2016; Braden et al., 2017; Rapa et al., 2018; Chakraborty et al., 2019; Benetti et al., 2021).

335 A Tertiary history involving two metamorphic episodes has been proposed for the GHC
336 (see Pêcher & Le Fort, 1986; Metcalfe, 1993; Pognante & Benna, 1993; Wiesmayr &
337 Grasemann, 2002; Carosi et al., 1999b; Lombardo & Rolfo, 2000; Hodges, 2000; Wiesmayr &
338 Grasemann, 2002; Cottle et al., 2009; Kohn, 2014; Robyr & Lanari, 2020). The first stage
339 (Eocene-Oligocene) of Barrovian-type metamorphism, termed the Eohimalayan event,
340 corresponds to the nappe's burial beneath Asia and is best preserved near the base of the unit
341 (e.g., Pêcher, 1989; Hodges et al., 1994; Wiesmayr & Grasemann, 2002). During this stage, the
342 base of the unit reached garnet-grade conditions (550-750°C and at least 8-10 kbar, e.g.,
343 Pognante & Benna, 1993; Hodges et al., 1994). Thrusting may have been accommodated by a
344 fault system considered a proto-STDS that reactivated as a normal fault during the second stage
345 in the Miocene (e.g., Vannay & Hodges, 1996; Wiesmayr & Grasemann, 2002; DiPietro &
346 Pogue, 2004). The locations where this scenario has been proposed show mylonitic contractional
347 fabrics overprinted by extensional structures and include the Himachal Pradesh, NW India
348 (Vannay & Grasemann, 1998), Zaskar, NW India (Patel et al., 1993), and the Kali Gandaki,
349 central Nepal (Vannay & Hodges, 1996). Note that even earlier events may have preceded
350 Himalayan orogenesis and can be challenging to distinguish from Cenozoic tectonics (see
351 Gehrels et al., 2003).

352 The Eohimalayan event occurred between 50-35 Ma coincides with a dramatic decrease
353 in convergence rate between India and Asia from ~ 15 to ~ 4 cm/yr (Copley et al., 2010). During
354 the Miocene Neohimalayan event, the base of the GHC experienced 550-600°C and the top
355 records lower pressures and/or temperatures (3-7 kbar, 575-850°C) (e.g., Hodges et al., 1994;
356 Simpson et al., 2000; Daniel et al., 2003). The Neohimalayan event has been associated with
357 MCT slip and with the development of Miocene-age High Himalayan leucogranites found in
358 close association with STDS (Pêcher, 1989; Harris et al., 1993; Metcalfe, 1993; Hopkinson et al.,
359 2017; Liu et al., 2018; Yang et al., 2019; Wu et al. 2020).

360 The duration and onset of MCT movement varies along strike and is often attributed
361 sometime during the Miocene. To time fault activity, monazite [(Ce, La,Th)PO₄] is often
362 targeted, a mineral that appears in these rocks at garnet grades and is ideal for timing
363 metamorphism (e.g., Catlos, 2013). In western Bhutan, the duration of MCT displacement is
364 bracketed by monazite ages between 20.8 ± 1.1 and 15.0 ± 2.4 Ma (Togbay et al., 2012). However,
365 in eastern Bhutan, prograde metamorphism and deformation is reported to have been underway
366 along the structure by c. 23 Ma (Daniel et al., 2003). Monazite ages from the lower portions of
367 the GHC in western Nepal yield younger ages timed to fault motion at 17-13 Ma (Montomoli et
368 al., 2013). Depth profiling of unpolished monazite indicate that the MCT hanging wall was
369 deforming in central Nepal between 24-22 Ma (Harrison et al., 1995). The 22 Ma age is also
370 attributed to MCT activity in central Nepal (Hodges et al., 1996; Coleman & Hodges, 1998)

371 In NW India (Garhwal region), the MCT shear zone is thought to be active from 20 Ma to
372 5 Ma (Iaccarino et al., 2020) or even younger to 1 Ma (Catlos et al., 2007; 2020). Mukhopadhyay
373 et al. (2017) suggest activity on the MCT itself in the Sikkim region occurred in pulses over an
374 extended period of time from 26 to 11 Ma. Monazite grains from the MCT shear zone in the
375 Sikkim indicate the structure was active at c. 22 Ma, 14-15 Ma, and 12-10 Ma (Catlos et al.,
376 2007) and from 21-13 Ma (Mottram et al., 2014). Younger ages are attributed to structures south
377 of the GHC-LHF contact, and are often found at lower structural levels within the shear zone
378 elsewhere. For example, Figure 5 shows the distribution of in situ secondary ion mass
379 spectrometry (SIMS) Th-Pb monazite and muscovite $^{40}\text{Ar}/^{39}\text{Ar}$ total gas ages along the Darondi
380 Khola (Catlos et al., 2001). The oldest early Miocene monazite ages are found in upper LHF
381 units (21.7 ± 1.2 Ma to 21.1 ± 0.8 Ma), but they decrease towards lower structural levels to 7.6 ± 0.2
382 Ma to 6.9 ± 0.5 Ma. In Arun valley of eastern Nepal Himalayas, Oligocene activity within the
383 upper portions of the MCT shear zone has been reported (~ 31 Ma, Groppo et al., 2010). Late
384 Eocene to Oligocene monazite ages have been found in GHC samples from central Nepal
385 (37.6 ± 3.8 Ma to 30.4 ± 0.5 Ma, Catlos et al., 2001; see also Gibson et al., 2016 for the same
386 transect) and NW India (37.9 ± 0.9 Ma to 34.3 ± 0.8 Ma, Catlos et al., 2007). The Oligocene ages
387 are consistent with the events related to the Eohimalayan time frame of Himalayan orogenesis
388 and may not be related to activity along the MCT.

389 Distinguishing between the Eohimalayan and Neohimalayan events is challenging, and
390 the Eohimalayan event may only be recorded in GHC and Tethyan units in particular locations
391 (Aikman et al., 2008; Stickroth et al., 2019). North-east verging folds of the Tethys Formation
392 may have developed during the Eohimalayan event (e.g., Godin et al. 1999a, 1999b), whereas
393 these and others reported in the GHC (Bhargava & Bassi, 1994; Carosi et al., 1999b) may be the
394 result of gravity sliding along the STDS (e.g., Burchfiel et al., 1992; Hodges et al., 1996; Vannay
395 & Hodges, 1996; Searle, 2010). Large-scale folding that aligns preexisting isograds into an
396 apparent inverted metamorphic position was attributed as a significant factor in the metamorphic

397 history of the GHC (Searle & Rex, 1989). In a petrochronology study of GHC monazite-bearing
 398 assemblages, Gibson et al. (2016) suggest that Eocene-Oligocene monazite ages represent
 399 prograde burial, which was followed by Miocene retrograde metamorphism and Miocene-
 400 Pliocene exhumation. Wu et al. (2020) suggest the High Himalayan leucogranites can be
 401 classified as Eohimalayan (46-25 Ma), Neohimalayan (25-14 Ma), and post-Himalayan (<14
 402 Ma) based on their relationship with particular detachment systems, ages, and compositions.
 403 Some North Himalayan granites that intrude Indian shelf sediments are similar in age to their
 404 post-Himalayan stage (Harrison et al., 1997; 1998; Lee et al., 2004; Zhang et al., 2004).

405 **2.2.3. Metamorphism in the LHF**

406 At their base, the GHC is thrust over Middle Proterozoic phyllites, metaquartzites, and
 407 mylonitic augen gneisses of LHF along the broad-scale 8-12 km thick MCT shear zone (Le Fort,
 408 1975; Gansser, 1981; Arita, 1983; Brunel & Kienast, 1986; Pêcher, 1989; Searle & Rex, 1989;
 409 England et al., 1992; Schelling, 1992; Le Fort, 1996; Henry et al., 1997; Harrison et al., 1998;
 410 Kohn et al., 2004; Bollinger et al., 2006; Carosi et al., 2013; Parsons et al., 2016; Martin,
 411 2017a,b; Mukhopadhyay et al., 2017; Yin & Harrison, 2000; Catlos et al., 2001; Catlos et al.,
 412 2018; 2020). The onset of MCT activity occurred during the early Miocene (Pêcher, 1991;
 413 Vannay et al., 2004; Yin, 2006), at a time when Indo-Asia convergence slows (>40% between
 414 20-10 Ma, Molnar and Stock, 2009) and had a significant impact on the extrusion of the GHC
 415 orogenic wedge (Maiti et al., 2020). The MCT fault system plays a central role in many models
 416 for the evolution of the Himalayas (e.g., Le Fort, 1975; Searle & Rex, 1989; England et al., 1992;
 417 Henry et al., 1997; Harrison et al., 1998; Bollinger et al., 2006; Kohn, 2008; Carosi et al., 2013;
 418 Beaumont et al., 2001; 2004; Jamieson et al., 2004; 2006; Searle et al., 2006; Long &
 419 McQuarrie, 2010; Wang et al., 2013; Cottle et al., 2015).

420 Lack of an apparent break in metamorphic grade between the GHC and LHF makes the
 421 placement of the boundaries of the MCT shear zone difficult to discern. Definitions of the
 422 structure center around age, metamorphic history, rheology, and role as separating units of
 423 different depositional environments (see Martin, 2017a). As the GHC and LHF evolved in
 424 different depositional environments, geochemical and geochronological evidence aids in its
 425 placement (e.g., Parrish & Hodges, 1996; Ahmad et al., 2000; Martin, 2017a,b; Khanal et al.,
 426 2014). The original Pêcher (1989) MCT definition involved three criteria in identifying the MCT
 427 in the field: (1) the boundary between hanging wall gneisses and upper carbonate-rich formations
 428 of the Lesser Himalaya, (2) where Lesser Himalaya shear fabric (L-S) is replaced by the
 429 flattening fabric of the Greater Himalayan Crystallines, and (3) where the rotational deformation
 430 that increases progressively through the Lesser Himalaya reaches a maximum. In central Nepal,
 431 Arita (1983) places two thrusts (MCT-I and MCT-II) on each side of the MCT shear zone. The
 432 MCT-II corresponds to that described by Pêcher (1989), whereas the MCT-I separates a
 433 mylonitic augen gneiss from other Lesser Himalaya metasedimentary rocks. The MCT-I
 434 correlates to the Ramgarh Thrust, which accommodates the Ramgarh Thrust sheet within the
 435 LHF duplex (DeCelles et al., 2001; Robinson et al., 2003; Pearson & DeCelles, 2005; Robinson
 436 et al., 2006; Matin and Mukul, 2010; Khanal et al., 2014; Mandal et al., 2015). Some researchers
 437 do not recognize the MCT-I anywhere in the Nepal Himalaya (see Upreti, 1999). Along the
 438 Dudh Kosi-Everest transect, the MCT corresponds to the contact between the GHC gneisses and
 439 the upper LHF pelitic schists, whereas the MCT-I separates the mylonitic Phaplu augen gneiss
 440 from low-grade Lesser Himalaya metasedimentary rocks. Along the Bhagirathi River, Garhwal
 441 region, the Vaikrita Thrust (=MCT) and Munsiri Thrust (=MCT-I) bound the MCT shear zone,

442 but no equivalent to the Phaplu augen gneiss is exposed (e.g., Valdiya, 1980; Pêcher, 1991;
443 Metcalfe, 1993; Searle et al., 1993; Ahmad et al., 2000; Singh & Thakur, 2001).

444 The MCT footwall is characterized and defined by inverted metamorphism, where
445 metamorphic grade increases toward structurally shallower levels (e.g., Ray, 1947; Pêcher, 1989;
446 Larson et al., 2015; Chakraborty et al., 2016; Searle et al., 2008; Iaccarino et al., 2020).
447 Understanding the origin this phenomenon has implications for establishing the role of various
448 crustal heat sources and mechanisms of heat transfer within collisional belts (e.g., radiogenic,
449 asthenospheric input, shear heating, addition of melts) (e.g., England et al., 1992) and is
450 facilitated by obtaining metamorphic P-T conditions and paths from shear zone garnet-bearing
451 assemblages (Stäubli, 1989; Metcalfe, 1993; Kaneko, 1995; Vannay & Hodges, 1996; Vannay &
452 Grasemann, 1998; Manickavasagam et al., 1999; Kohn et al., 2001; Catlos et al., 2001; Imayama
453 et al., 2010; Corrie et al., 2010; Larson et al., 2013; Anczkiewicz et al., 2014; Kohn, 2014;
454 Mottram et al., 2014; Mukhopadhyay et al., 2017; Catlos et al., 2018; Waters, 2019; Catlos et al.,
455 2020).

456 The MCT has also been considered to be an expression of the Main Himalayan Thrust
457 (MHT) (Bollinger et al., 2004; Mahajan et al., 2010), a pervasive décollement that separates the
458 downgoing Indian plate from the Himalayan orogenic wedge (Figure 2) (Bilham et al., 1997;
459 Nelson et al., 1996; Subedi et al., 2018; Zhao et al., 1993). Other surface expressions of the MHT
460 include the MBT and Main Frontal Thrust (MFT) (Figure 1 and Figure 2). The STDS may be a
461 local phenomenon, occurring when the Tethys dissociated from the GHC and slid along N-
462 dipping planes due to gravity following uplift (e.g., Pêcher & Le Fort, 1986; Fuchs, 1987),
463 although some models for channel flow connect this fault system to the MHT (e.g., Beaumont et
464 al., 2001; 2004; Jamieson et al., 2004; 2006). The MHT is one of the largest and fastest slipping
465 continental megathrusts on Earth (e.g., Duputel et al., 2016; Rajendran et al., 2017; Searle et al.,
466 2017). Understanding its geometry, history, and fault systems that splay into the structure has
467 implications for assessing and predicting the initiation, propagation, and termination of major
468 event Himalayan earthquakes (e.g., Wang et al., 2017). The topography of the MHT is uncertain
469 (e.g., Caldwell et al., 2013; Denolle et al., 2015; Elliott et al., 2016; Hazarika et al., 2017;
470 Hubbard, 2016; Nábělek et al., 2009; Whipple et al., 2016; Wang et al., 2017; Zhou et al., 2019),
471 due in part to the lack of recognition that fault systems within the LHF duplex or MCT shear
472 zone have the potential to accommodate present-day slip (Catlos et al., 2020). The LHF duplex
473 has long been known to be a ~50-km-wide seismogenic zone of predominately moderate
474 earthquakes (Bai et al., 2016; Cattin & Avouac, 2000; Khattri & Tyagi, 1983; Mahajan et al.,
475 2010). Bai et al. (2016) suggest that a thrust system within the LHF is the most seismically active
476 region in the Himalayas and accommodates most of its elastic strain accumulation. Alternatively,
477 the shallower events are explained by a segmented MHT that includes a ramp (He et al., 2018;
478 Hubbard, 2016; Pandey et al., 1995).

479 **2.2.4 The MBT and MFT**

480 South of the MCT, the MBT separates the Lesser Himalaya from Neogene molasse, the
481 Siwalik Formation (Figure 1) (Valdiya, 1992; Meigs et al., 1995; Mukul, 2000; Thakur et al.,
482 2010; Goswami & Deopa, 2017; Dhamodharan et al., 2020). South of the MBT, the MFT is the
483 boundary between the Siwalik Formation and the northern Indo-Gangetic Plains (e.g., Mugnier
484 et al., 1999; Mukul et al., 2007; Burgess et al., 2012; Bollinger et al., 2014). The MBT has few
485 timing constraints, but is primarily thought to have been initiated during the Late Miocene (13-
486 10 Ma, Meigs et al., 1995; Chirouze et al., 2012; Patra & Saha, 2019), although it may have been

487 active since 5 Ma in Nepal (DeCelles et al. 2020). The Siwalik formation overall is a 7-10 km-
 488 thick succession of dominantly fluvial sedimentary rocks located along the entire length of the
 489 Himalaya from the Potwar plateau to the Brahmaputra in the east, likely due to the evolution of
 490 the Ganga river system (Bora and Shukla, 2005; Sanyal & Sinha, 2010; Khan et al., 2019;
 491 Dhamodharan et al., 2020). The Siwalik unit itself is divided into several sectors due to
 492 lineaments related to normal faulting in the Indian basement that reactivated as thrust faults
 493 during Himalayan collision (Raiverman et al., 1983; Dubey, 1997; Sanyal & Sinha, 2010). The
 494 Siwalik formation records key information regarding Himalaya erosional history, paleoclimate,
 495 transitions in paleobotany, and exhumation rates (e.g., Quade et al., 1989, 1995; Acharya, 1994;
 496 Najman et al., 2009; Sanyal & Sinha, 2010; Najman et al., 2017; Ghosh et al., 2018; Khan et al.,
 497 2019). In some locations, the MBT has nearby active steep faults that show normal or strike-slip
 498 senses of motion as they accommodate a critical taper (Mugnier et al., 1994; Patra & Saha,
 499 2019). The MFT cuts Siwalik strata in places and is often manifested as growing anticlines
 500 (Yeats et al., 1992; Powers et al., 1998; Srivastava et al., 2018). These crustal-scale faults sole
 501 into the MHT (Figure 2) (Zhao et al., 1993; Nelson et al., 1996).

502 **3. Models for the extrusion of the Himalayan core**

503 The MCT fault system has long played a central role in models for the evolution of the
 504 Himalaya. Initial models presume that activity along the MCT only occurred during the Early
 505 Miocene (Figure 6) (Le Fort, 1975; Searle & Rex, 1989; Hubbard, 1996; England et al., 1992;
 506 Hodges et al., 1993; Harris & Massey, 1994). LeFort (1975) conceived that the inverted
 507 metamorphism in the LHF footwall was caused by the transfer of thermal energy due to large-
 508 scale underthrusting of the LHF beneath the GHC (the “Hot-Iron model” Figure 6A). In this
 509 scenario, fluids released from the MCT footwall migrate through the hanging wall and flux a
 510 leucogranite belt. The alternative was proposed by Hubbard (1996), in which the inverted
 511 mineral isograds result from ductile shearing a pre-existing zone of right-way-up metamorphism
 512 (Figure 6B). Searle and Rex (1989) delegated a significant role to STDS and suggested that the
 513 present-day distribution of metamorphic facies and leucogranite bodies are caused by
 514 overprinting earlier isograds during MCT-related anatexis and folding (Figure 6C). Fluids
 515 released from the MCT footwall assist with the formation of leucogranite. The STDS has
 516 appeared prominently in almost every model since. Hodges et al. (1993) proposed that the wedge
 517 GHC extruded via synchronous STDS and MCT movement (Figure 6D), and Harris & Massey
 518 (1994) suggested extensional collapse led to rapid GHC exhumation and decompression melting
 519 of kyanite-bearing schists that led to melts emplaced near the STDS (Figure 6E).

520 As more data became available, more numerical solutions and quantitative models
 521 appeared (Figure 7). Molnar and England (1990) matched P-T conditions obtained by Hubbard
 522 (1996) by solving a one-dimensional time-dependent heat equation for an inclined fault (Figure
 523 7A). The model derived thermal energy from three sources: (1) radioactive nuclides, (2) the
 524 asthenosphere, and (3) frictional heating along the MCT, and suggested that shear stresses >100
 525 MPa can account for peak $T < 600^{\circ}\text{C}$ at the MCT and contributes $\sim 13^{\circ}\text{C}/\text{km}$ to the inverted
 526 geotherm. Huerta et al. (1998) introduced the idea that MCT inverted metamorphism was caused
 527 by accretion and erosion acting on a crust enriched with radiogenic elements (Figure 7B). The
 528 presence of post-Miocene mineral crystallization ages in the LHF and MCT shear zone led
 529 Harrison et al. (1998) to model footwall inverted metamorphism as the accretion of tectonic
 530 slivers of the LHF to the hanging wall (Figure 7, Figure 8A). This model was one of the first to
 531 suggest the concept of critical taper as an important control in developing inverted

532 metamorphism and the geometry of the fold-and-thrust belt. In this scenario, anatexis is linked to
533 shear heating on along the MHT. This model is also the first in a series that suggested the
534 Himalaya is an outcome of stacked thrust systems within and below the GHC (Figure 8) (e.g.,
535 Kohn, 2008; Corrie & Kohn, 2011; Cottle et al., 2015; Catlos et al., 2020).

536 Large-scale imaging of the Himalayan and Tibet crust led Nelson et al. (1996) to
537 advocate that thrusting within the Himalaya results from anatexis (Figure 7D). The Tibetan
538 middle crust is assumed to be partially molten today, and the region between the MCT and STDS
539 is earlier extruded equivalent. This model is the foundation of others that suggest the GHC is the
540 result of gravity-driven lateral mid-crustal flow (Gruijic et al., 1996; Beaumont et al., 2001;
541 Jamieson et al., 2006; Searle, 2010; Webb et al., 2011; Cottle et al., 2015). Channel flow was
542 initially conceived as a Neohimalayan event, with the extrusion of the GHC due to synchronous
543 MCT and STDS activity with focused erosion along the topographic front (e.g., Beaumont et al.,
544 2001; 2004; Jamieson et al., 2004; 2006; Robinson et al., 2006; Searle et al., 2006; Long &
545 McQuarrie, 2010; Wang et al., 2013; Cottle et al., 2015). This model can be combined with the
546 scenario where LHF footwall slivers are accreted to the hanging wall as GHC channel flow
547 progressed (Figure 8B). LHF footwall inverted metamorphism may also be an outcome of
548 channel flow experienced by the GHC (Daniel et al. 2003; Searle et al., 2008).

549 Channel flow has also been invoked to model the inverted metamorphic sequence within
550 the MCT footwall, where discrete fault systems within the LHF and the MCT or other faults
551 within the GHC are active during the Miocene (Imayama et al., 2010; Goswami-Banerjee et al.,
552 2014). The alternative to channel flow is the critical taper model, where the GHC is exhumed
553 through a series of stacked thrust systems within and below the GHC (Figure 8A) (Kohn, 2008;
554 Corrie & Kohn, 2011). Critical taper has also been applied to explain thrusting with fault systems
555 associated with the MFT (Mukul et al., 2007; Hirschmiller et al., 2013). In addition, the
556 recognition that in NW India, the LHF and Tethyan Formation appear in thrust contact suggests
557 that the GHC may have acted as a tectonic wedge (Figure 8C and D) (Webb et al., 2007; Webb
558 et al., 2011; Cottle et al., 2015). One outcome of these models has been a wholesale re-
559 distribution and re-defining of the MCT from a fault system that separates the GHC and LHF to
560 one in which portions of the GHC are involved in large-scale thrust movement (Searle et al.,
561 2008; Carosi et al., 2018). The inverted metamorphic sequence is redelegated from the LHF and
562 MCT footwall to lower levels of the GHC (Figures 8E and F). Thermal heating along faults
563 within the GHC may have played a role in accommodating wedge extrusion and developing
564 inverted metamorphism (e.g., Goscombe et al., 2006; Searle et al., 2008). Figure 8G shows a
565 scenario in which the MCT shear zone develops due to imbrication and activity is accommodated
566 by fault systems within the GHC (Carosi et al., 2016). GHC structures include the Kalopani
567 shear zone (KSZ) at 41-30 Ma (Eohimalayan time frame) and High Himalayan Discontinuity
568 (HHD) at 26-24 Ma (Neohimalayan).

569 Although lines of evidence exist that the LHF inverted metamorphism involved multiple
570 episodes of post-Miocene imbrication and deformation with the MCT shear zone or LHF duplex
571 (e.g., Figure 5) (Caddick et al., 2007; Catlos et al., 2001; Kohn et al., 2001; Groppo et al., 2009;
572 2010; Herman et al., 2010; Mosca et al., 2012; Montomoli et al., 2013; Mottram et al., 2014;
573 Carosi et al., 2016; Braden et al., 2018; Catlos et al., 2018; Montemagni et al., 2018; Catlos et
574 al., 2020; Montemagni et al., 2020), the idea of tectonic inversion of a coherent rock package
575 that experienced a single Barrovian Neohimalayan-related metamorphic event remains (Hubbard,
576 1996; Martin et al., 2010; Gaidies et al., 2015). Multiple episodes of ductile overthrusting of the

577 GHC over the LHF are proposed as an explanation (Goscombe & Hand, 2000), as well as post
 578 and tectonic overpressure that changed fundamental rock properties (Thakur et al., 2015; model
 579 of Schmalholz & Podladchikov, 2013). The originally-proposed “hot iron” model in which the
 580 primary heat source for inverted metamorphism is GHC thermal energy transferred as Miocene
 581 MCT emplacement occurred (England & Molnar, 1993) has an alternative end-member, where
 582 no contribution of dissipative to downward conductive heating from the GHC is required
 583 (Stephenson et al., 2000).

584 The Himalaya is often framed as a large-hot orogen that may have grown by distributed
 585 extrusion (channel flow) or discrete thrusting (critical taper) (Beaumont et al., 2006; Jamieson &
 586 Beaumont, 2013; Mukherjee, 2013; Iaccarino et al., 2020; review in Wang et al., 2013). In fact,
 587 both scenarios may be relevant to the Himalayan core, depending on the location within the
 588 range and the time frame of metamorphism (Larson et al., 2010; Mukherjee, 2013; Cottle et al.,
 589 2015). The Himalaya may indeed represent a scenario in which the two ‘end-member models
 590 apply and are not mutually exclusive (Beaumont & Jamieson, 2010; Larson et al., 2010, 2013;
 591 Corrie et al., 2012; Jamieson & Beaumont 2013; Cottle et al., 2015). Evaluating models for GHC
 592 extrusion requires understanding of the P-T-t paths of its rocks as they experienced the transition
 593 from convergence and subduction to their final exhumation (e.g., Catlos et al., 2001; Caddick et
 594 al., 2007; Kohn, 2008; Corrie et al., 2010; Goswami-Banerjee et al., 2014; Catlos et al., 2018,
 595 2020).

596 Kohn (2008) presents particle paths predicted by end-member critical taper and channel
 597 flow models in the end-member models. Channel flow predicts the GHC experienced isothermal
 598 exhumation, and the LHF experiences isobaric heating. Critical taper predictions imply isobaric
 599 cooling for GHC rocks and “hair-pin” LHF P-T paths (Kohn, 2008). The metamorphic field
 600 gradients predicted by the models also differ. Complicating this scenario is the observation that
 601 P-T conditions from garnet-bearing assemblages collected from the MCT hanging wall indicate
 602 the unit has cryptic discontinuities related to unmapped faults, shear zones, or inheritance of pre-
 603 existing basement structures (see discussions in Mukherjee et al., 2012; Larson et al., 2013;
 604 Montomoli et al., 2015; Cottle et al., 2015; Carosi et al., 2016). Understanding when these
 605 possible fault systems, termed High Himalayan discontinuities (HHD), were active is critical for
 606 deciphering the processes involved during convergence. Their age may similar to activity along
 607 the MCT (28-18 Ma; e.g., Carosi et al., 2010; Montomoli et al., 2013, Larson et al., 2015;
 608 Montomoli et al., 2015; Carosi et al., 2016; Carosi et al., 2018; Benetti et al., 2021). This is a
 609 scenario that is not accounted for in the channel flow model (e.g., Benetti et al., 2021; Maiti &
 610 Mandal, 2021).

611 **4 Himalayan Metamorphism and Contractional Tectonics (Daroni Khola, Central Nepal)**

612 As indicated in the previous sections, garnet-bearing assemblages are valuable recorders
 613 of compressional/contractional metamorphism and help constrain models for the Himalaya’s
 614 uplift history. P-T data from garnet-bearing Himalayan assemblages can be generated using
 615 several approaches (see review in Waters, 2019). This section compares conditions generated
 616 using conventional thermobarometers and the Gibb’s method (Kohn et al., 2001) to those
 617 obtained using isochemical phase diagrams, isopleth thermobarometry, and the garnet zoning
 618 method (e.g., de Capitani & Petrakakis, 2010; Moynihan & Pattison, 2013; Catlos et al., 2018;
 619 2020). The approaches were applied to the same samples and data from rocks collected from the
 620 GHC and LHF units along the Daroni Khola in central Nepal (Figure 3, Figure 4, Figure 5). The
 621 TheriaG model of Gaides et al. (2008) is also used to predict garnet zoning based on Gibb’s P-T

622 paths for some samples. The reason for any discrepancies in the P-T paths and conditions within
623 the context of equilibrium thermodynamics is evaluated, and the impact of the results on models
624 for Himalayan orogenesis is explored. Regardless of calibrations used, the P-T conditions and
625 paths coupled with previously-reported timing constraints from Darondi Khola assemblages
626 suggest the MCT shear zone developed during pulses of movement that resulted in progressive
627 transfer of rock packages as the MCT shear zone developed (Catlos et al., 2001; Kohn et al.,
628 2001).

629 **4.1 Methods, samples, and assumptions**

630 **4.1.1 Samples**

631 Kohn et al. (2001) report rim P-T conditions from eighteen garnet-bearing assemblages
632 exposed along the Darondi Khola and divides LHF samples into lowermost (n=3), lower to mid
633 (n=6), and upper MCT zones (n=4) (Figure 4 and Figure 5, Table 1). Five GHC rocks were also
634 analyzed. We use the definition of the MCT shear zone following this nomenclature, but also
635 note that based on the placement of the Phaplu and Ulleri augen gneisses, others would allocate
636 all of these samples squarely in the GHC unit (e.g., Searle et al., 2008).

637 Mineral assemblages, X-ray element maps, and compositional transects were made across
638 garnets and are reported in Kohn et al. (2001). Petrographic images of some samples are shown
639 in Figure 9. All samples contain garnet and prograde quartz, muscovite, biotite, and ilmenite. All
640 are metamorphosed pelites, except DH38, which is a metabasite and contains hornblende and
641 plagioclase. All lower LHF rocks contain prograde chlorite and plagioclase, but DH75A and
642 DH75B also have retrograde chlorite (Figure 9). The upper LHF and GHC rocks do not have
643 chlorite (DH38, DH60, DH61, DH63, DH66, DH67) or contain only retrograde chlorite (DH57,
644 DH58, DH71). All samples, except upper LHF rock DH57, contain plagioclase. Most plagioclase
645 show core-rim zoning with higher-Ca cores and lower-Ca rims, expected if garnet grew in a
646 closed chemical system (Spear et al., 1990). Samples DH26, DH75A, and DH75B have
647 plagioclase with relict albite cores overgrown by an oligoclase mantle that is either unzoned or
648 slightly zoned to lower Ca towards its rim. The mantle was assumed to be metamorphic and
649 reflects garnet growth and uptake of Ca. Sample DH57 has both staurolite and kyanite, whereas
650 DH63 has staurolite. Other rocks for this study do not show any of these index minerals. No
651 chloritoid or carbonate minerals are reported in the samples. All samples appear syntectonic and
652 the presence of strain shadows are common. As seen in Figure 9, micas and quartz appear
653 deflected around the garnet porphyroblasts. Some garnets are inclusion free, however, middle
654 LHF sample DH30 has quartz inclusions in the center of the garnet that appear thinner and
655 elongated compared to the larger, anhedral grains in its outer-rim region. GHC samples DH61,
656 DH63, and DH67 have inclusion filled cores and inclusion free outer rims. Inclusions of ilmenite
657 and quartz in middle LHF samples DH51 and DH75B are aligned in relatively straight tracks
658 into the rock matrix, consistent with syntectonic growth.

659 Figure 10 shows garnet compositional transects for LHF samples in which high-
660 resolution P-T paths (DH17, DH19, DH22, DH23, DH26, DH75B) were obtained and Figure 11
661 shows compositional transects across garnets in two GHC samples (DH61 and DH66). LHF
662 samples show typical prograde bell-shaped profiles in Mn, with no evidence of retrogression at
663 the rims. The garnets all show a smooth decrease in grossular and increase in pyrope and
664 almandine from core to rim. GHC garnets, however, show evidence of retrogression with sharp
665 increases in Mn contents at the rim. These garnets also show significant fluctuations in grossular,

666 pyrope, and almandine from core to rim. GHC samples are not ideal candidates for high-
 667 resolution P-T path modeling because their zoning profiles suggests modification of prograde
 668 garnet compositions after growth, open-system behavior, and the potential of major changes in
 669 rock bulk composition after growth. These situations are assumed not to occur when modeling
 670 and developing high-resolution P-T paths.

671 **4.1.2 Conventional thermobarometry and Gibbs method P-T paths**

672 The garnet-biotite thermometer calibrated by Ferry and Spear (1978) with the Berman
 673 (1990) Ca-in garnet solution model and the garnet-muscovite-biotite-plagioclase barometer of
 674 Hoisch (1990) were applied to the assemblages with pelitic bulk compositions (Kohn et al.,
 675 2001). Sample DH38 is a metabasite, so the garnet-hornblende thermometer of Graham and
 676 Powell (1984) and the garnet amphibolite barometer of Kohn & Spear (1990) were used. Results
 677 are summarized in Table 1. The conditions are internally consistent, and Kohn et al. (2001)
 678 emphasize that different calibrations would change estimated P and T by $\pm 25^\circ\text{C}$ and $\pm 0.5\text{--}1$ kbar
 679 and would not alter overall trends. The conditions were estimated using minimum garnet Mn
 680 contents. Note that these garnet compositions are the same used for the estimating the garnet rim
 681 conditions using isopleth thermobarometry as described in the next section (Table 2; polygons in
 682 Figure 12, Figure 13, Figure 14, Figure 15, Figure 16, Figure 17).

683 The Gibb's method to generate the P-T paths from zoned garnets and their co-existing
 684 matrix mineral assemblages is outlined in Spear & Selverstone (1983), Spear (1986, 1993), Spear
 685 et al. (1984), and Spear & Rumple (1986). P-T paths were only generated from LHF rocks with
 686 pelitic bulk compositions (DH16, DH17, DH22, DH23, DH26, DH75A, and DH75B) that
 687 preserved prograde compositional zoning best. The rocks were modeled with the observed solid
 688 assemblage garnet + biotite + chlorite + muscovite + plagioclase + quartz in the
 689 MnNCKFMASH system. Compositional changes were derived from garnet and plagioclase
 690 compositional zoning produced as the garnet grew. Garnet core and rim conditions were selected
 691 for samples DH17, DH19, DH22, and DH26, whereas an intermediate point was also included
 692 for samples DH23, DH75A, and DH75B. This intermediate garnet composition was used to
 693 better account for nonlinearity in the garnet zoning pattern. In the case of DH23 and DH75B, its
 694 inclusion results in hair-pin P-T paths (Figure 13A, Figure 14C, and Figure 17). A pure H₂O
 695 fluid at lithostatic pressure was assumed to have been present. Kohn et al. (2001) emphasize that
 696 activity models would not significantly affect the trends of retrieved P-T paths.

697 The P-T results obtained using conventional and Gibb's method show an inverted
 698 metamorphic signature in the LHF, with P-T conditions increasing up section from near the
 699 garnet isograd at $520\pm 25^\circ\text{C}$ and 5.0 ± 1.0 kbar (DH16) to $640\pm 25^\circ\text{C}$ and 11.5 ± 2 kbar (samples
 700 DH57 and DH58) just below the mapped MCT. GHC rocks were collected near the mapped
 701 MCT (Figure 4 and Figure 5) and record the highest P-T conditions ($660\text{--}715^\circ\text{C}$ and $7.6\text{--}11.5$
 702 kbar). Samples DH17, DH19, and DH75A have P-T paths consistent with burial (increasing in
 703 both P and T), whereas those from DH22 and DH26 yield exhumation paths (decreasing P with
 704 increasing T). P-T paths from DH75B and DH23 are "hair-pin" and are interpreted as recording
 705 both burial and exhumation during imbrication of the MCT shear zone. Monazite inclusions in
 706 DH75B garnets range from 11.1 ± 0.7 Ma to 7.6 ± 0.2 Ma (Th-Pb secondary ion mass
 707 spectrometry, SIMS, $\pm 1\%$) and were interpreted as constraining Late Miocene reactivation of the
 708 MCT shear zone (Figure 5). These Late Miocene monazite inclusions in garnet are also found in
 709 other samples along the transect as well as young (Pliocene-Late Miocene) $^{40}\text{Ar}/^{39}\text{Ar}$ muscovite
 710 total gas ages (Catlos et al., 2001; Kohn et al., 2001).

711 4.1.3 Isopleth core thermobarometry

712 The approach to obtain isopleth P-T conditions and paths is the same as that outlined in
 713 Catlos et al. (2018, 2020) and Etzel et al. (2019). Bulk rock compositions were obtained from
 714 rock chips of the DH samples using inductively coupled plasma spectrometry (ICP) at Activation
 715 Laboratories (Canada) (Table 3 and Table 4). No modifications in these compositions were made
 716 for the approach. Samples DH22 and DH23 were collected nearby, and the same bulk
 717 composition is used for both rocks. Compositions vary from low SiO₂ (~45 wt % samples DH17,
 718 DH22, and DH23) to higher SiO₂ (69-76 wt% DH26, DH75A). In general, upper LHF and GHC
 719 rocks have mid to high SiO₂ contents (56-80 wt%). Their molar values are used as direct input
 720 for the effective bulk composition needed to create the isochemical phase diagrams using the
 721 software package Theriak-Domino (de Capitani and Brown, 1987; de Capitani and Petrakakis,
 722 2010) (Figure 12, Figure 13, Figure 14, Figure 15, Figure 16, Figure 17). The Holland and
 723 Powell (1998 with updates to solution models through 2010) thermodynamic dataset and
 724 appropriate mixing models in the system MnO-Na₂O-CaO-K₂O-FeO-MgO-Al₂O₃-SiO₂-H₂O-
 725 TiO₂ were used. The specific solid solution models used are the same as in Catlos et al. (2018).
 726 H₂O saturation is assumed for these samples (i.e., H₂O (100) in Theriak Domino), as is
 727 appropriate for these assemblages. Fe³⁺ was not estimated but did not significantly affect results.

728 For samples where compositional data were available from the garnet's central section,
 729 isopleths of ±0.01-0.02 mole fraction spessartine, almandine, pyrope, grossular, and ±0.01-0.02
 730 Mg-# (Mg/Fe+Mg), are plotted on the phase diagram as grey-shaded bars. Their intersection
 731 corresponds with our closest approximation of garnet core P-T conditions as indicated by a
 732 polygon. Although isopleth intersections occurred over small regions, the uncertainty in the
 733 conditions is likely approaching that of conventional methods (i.e., ±25°C and ±1 kbar).
 734 Overlapping garnet core isopleths are only found for LHF samples DH17, DH19, DH22, DH23,
 735 DH26, DH75A, DH75B, DH58, and GHC sample DH61 (Figures 12, Figure 13, Figure 14,
 736 Figure 15, Figure 16). The core was defined as the portion of the garnet with the highest Mn
 737 content and is the best approximation of the chemical system when garnet began growth. In all
 738 cases, the intersections are located in mineral stability fields consistent with their assemblages
 739 (feldspar + garnet + biotite + phengite + ilmenite ± rutile ± chlorite + quartz + H₂O) and
 740 anticipated conditions. Core metamorphic conditions increase up section over a north-south
 741 distance of ~5 km from a low of 4-4.5 kbar and 520-540°C in lower LHF samples DH17 and
 742 DH19 to 6.8-7.5 kbar and 540-550°C in middle LHF samples DH75A and DH75B (Table 2).
 743 Upper LHF sample DH58 collected directly beneath the MCT yields overlapping core isopleths
 744 at ~550°C and 6.0 kbar. Core isopleths for GHC sample DH61 overlap at ~7 kbar and 580°C,
 745 similar to those from some LHF rocks (Table 2).

746 The garnet-in reaction line and garnet growth contours (volume 0.5% increments) are
 747 overlaid on each isochemical phase diagram (Figure 12, Figure 13, Figure 14, Figure 15, Figure
 748 16). The topology of the diagrams and the location of the garnet core suggest that garnet appears
 749 in all samples through chlorite dehydration. Only samples DH75A and DH75B yield core P-T
 750 conditions that overlap the garnet-in reaction line (Figure 14). The other samples yield
 751 overlapping isopleths on or near the 0.5% (DH17, Figure 12A), 1% (DH19, DH61, DH58, Figure
 752 12C, Figure 15A and Figure 15C), and 1.5-2% volume contours (DH22 and DH23, Figures 12E
 753 and Figure 13A). The results suggest that the true core was missed during the analysis of these
 754 garnets. The lack of retrograde zoning in the LHF samples suggests that the effect of diffusional

755 homogenization is minimal (Figure 10), although this process likely modified GHC DH61 garnet
756 compositions (Figure 11B).

757 **4.1.4 High-resolution and Gibb's P-T path modeling**

758 For samples DH17, DH19, DH22, DH23, DH26, DH75A, and DH75B, the garnet's core
759 isopleth P-T conditions can be directly compared to those obtained using the Gibb's approach
760 (Figure 17). Sample DH26 yields the same pressure using both methods (~6.5 kbar), but the
761 thermal conditions are lower using the Gibb's method by 50°C. Sample DH23 yields the same
762 thermal conditions using both approaches (~525°C), but the isopleth barometry suggests the
763 sample experienced lower pressures by ~2 kbar (5.1 kbar compared to 7.0 kbar). In all other
764 samples, isopleth thermobarometry results in the samples recording lower P (from 0.5 kbar to 1.7
765 kbar, samples DH75A and DH75B) and higher T (from 10°C to 50°C, samples DH75A and
766 DH75B) compared to than those generated by the Gibb's method. The discrepancies of 10°C and
767 0.5 kbar are within the stated uncertainties of both methods (Kohn, 1993), but those approaching
768 50°C and 1.5 kbar are significant differences that would influence understanding their depth of
769 exhumation and metamorphic reaction history. For example, in sample DH26, the Gibb's core P-
770 T condition shows similar P, but the low Gibb's T starting conditions lie in a region where
771 chlorite, not garnet, is stable (Figure 13C).

772 High-resolution P-T paths (Moynihan and Pattison, 2013) were generated for lower LHF
773 samples where garnet transect data were available, suggested prograde conditions, and minimal
774 modification since growth. In generating the high-resolution P-T paths, zoning profiles are
775 smoothed using a Savitzky-Golay function to minimize the impact of missing analyses due to
776 inclusions or cracks (Figure 10). The Matlab script starts with the bulk composition and initial
777 smoothed core garnet composition and calls Theriak-Domino to calculate an isochemical phase
778 diagram. A Matlab optimization function searches the P-T grid for the smallest misfit between a
779 modeled garnet composition and the smoothed composition. It then calculates the portion of the
780 bulk composition sequestered in the first step of garnet growth. Sequestered components are
781 subtracted from the bulk composition to estimate an effective bulk composition for the next step
782 of growth. A new diagram is calculated from the effective bulk composition, and the process is
783 repeated for all steps along the garnet zoning profile from core to rim. Each step yields an
784 estimate of the P-T conditions of incremental garnet growth, culminating in a P-T path. This data
785 is available in the repository.

786 Two independently estimated high-resolution P-T paths can be obtained from a rim-to-
787 rim compositional transect across the garnet using the garnet zoning method. The expectation is
788 that the P-T paths from the same garnet should record similar trajectories, and was the case for
789 samples DH17, DH19, and DH23 (Figures 12A and C, Figure 13A). The starting and endpoints
790 may differ due to the proximity of the initial condition near the garnet core and the extent of
791 garnet rim preservation. In addition, garnet zoning can be predicted by the high-resolution P-T
792 path and is indicated as a bolder grey line in Figure 10. The high-resolution P-T paths reproduce
793 the original garnet zoning to ± 0.01 mole fraction in most cases and for most compositions, which
794 is expected if the garnet behaved in a closed system and had no significant changes in bulk rock
795 composition as it grew.

796 As with the core conditions, the shapes of the high-resolution P-T paths for samples
797 DH17, DH19, DH22, DH23, DH75A, and DH75B can be directly compared to those obtained
798 using the Gibb's approach (Figure 17). The length of the high-resolution and Gibb's P-T paths are

799 similar (ranges from 14°C to 52°C) but do not show the same trajectories. For example, instead
 800 of hair-pin trajectories (increase in P followed a P decrease as T increases) predicted by DH23
 801 and DH75B Gibb's P-T paths, their high resolution P-T paths suggest that these rocks only
 802 experience an increase in P as T increased. The Gibb's P-T path in sample DH17 shows an
 803 increase in P, but the high-resolution P-T path from the same rock using the same data decreases
 804 in P as T increases. Minor fluctuations in P in the high-resolution P-T paths (± 10 -50 bars) in
 805 sample DH19 and near the core of sample DH22 are likely due to small compositional changes
 806 as the program seeks the best fit and should not be interpreted tectonically. DH19 shows an
 807 overall similar P-T path shape as the one reported using the Gibb's approach, but the conditions
 808 are different with the high-resolution P-T path showing much lower P (by ~ 2 kbar) and higher T
 809 (by $\sim 50^\circ\text{C}$). The high-resolution P-T paths from samples DH22 and DH23 are similar in that
 810 they show minor increases in P as T increased, but the Gibb's P-T path from sample DH22
 811 suggests decompression, a result not observed with this sample. A P-T path from sample DH26
 812 could not be generated due to a lack of garnet zoning data, but core and rim isopleth conditions
 813 suggest it could have followed the decompression path as T increased. A decrease in P as T
 814 increased is the same trajectory suggested by the Gibb's P-T path but at higher T conditions.

815 To gauge how well Gibb's P-T paths reproduce garnet zoning, the Gibb's P-T path was
 816 used as input in the program TheriaG (Gaides et al., 2008) using the bulk composition indicated
 817 in Table 3. The time of garnet growth over the P-T path is regularly spaced over durations of 5
 818 m.y., 10 m.y., and 15 m.y. Modeling parameters are available in supplementary files. In each
 819 case, the predicted Gibb's P-T path was identical and would predict garnet zoning inconsistent
 820 with what is observed in the sample (Figure 10). Results may change if different size classes than
 821 those used were selected (10 μm successive shells in 2000 μm garnet radius), if garnet growth
 822 did not occur over regular space durations, or if the selected exhumation path was different.
 823 Using the chosen parameters, the Gibb's P-T path predictions for samples DH17, DH19, and
 824 DH22 show similar trends with the garnet zoning but significantly different compositions (Figure
 825 10). The Gibb's P-T paths predictions for those samples that produced hair-pin P-T paths
 826 (DH75B and DH23) resulted in significantly different garnet zoning and compositions and did
 827 not replicate observed garnet compositions.

828 **4.1.5 Isopleth rim thermobarometry**

829 Garnet rim isopleth conditions were estimated using the same garnet compositions used
 830 to generate conventional P-T conditions. Rim isopleths also include those from the sample's
 831 average composition of matrix plagioclase (± 0.01 mole fraction Ca), chlorite, and biotite [± 0.01
 832 Mg-number, $\text{Mg\#} = \text{Mg}/(\text{Mg}+\text{Fe})$], when available. The last effective bulk composition generated
 833 by the high-resolution P-T paths was used for LHF samples DH17, DH19, DH22, DH23, and
 834 DH75B. For other LHF samples where garnet transect data is not available and for the GHC
 835 rocks, the bulk composition was used (DH26, DH75A, DH58, DH60, DH61, DH63, DH66,
 836 DH67) (Table 3 and Table 4). Only three GHC samples (DH61, DH63, and DH66) yield
 837 overlapping garnet compositional isopleths (Figure 15D, Figure 16A and B), and those from
 838 upper LHF sample DH58 did not overlap.

839 The extent of overlap of garnet rim with matrix mineral compositions varies for the GHC
 840 and LHF rocks. Garnet rim isopleths for GHC sample DH61 rim overlapped with all matrix
 841 mineral compositions, but DH66 show no overlap of the garnet rim with any of the matrix
 842 mineral compositions. The garnet rim isopleths for GHC sample DH63 overlapped with ± 0.01
 843 Mg-number chlorite, but not with the biotite or plagioclase compositions. As seen with some

844 footwall samples, the overlaps for the GHC assemblages are located far from the garnet-in
845 reaction line as seen by the garnet growth contours (>1.5 vol%) (Figure 15 and Figure 16). The
846 garnet rim isopleths for LHF samples DH17, DH19, DH22, DH23, and DH75B overlap with
847 Mg# biotite, but not plagioclase. No matrix mineral isopleths overlap with the garnet rim
848 isopleths for samples DH26 and DH75A within the compositional ranges applied here (± 0.01
849 mole fraction Ca and Mg#).

850 For samples where garnet and matrix mineral isopleths overlap, conditions are consistent
851 with their mineral assemblages and are similar to the garnet core assemblages (feldspar + garnet
852 + biotite + phengite + ilmenite \pm rutile \pm chlorite + quartz + H₂O). As with the core conditions,
853 the rim P-T conditions increase up section over a north-south distance of ~ 5 km from a low of
854 4.5-4.8 kbar and 550-560°C in lower LHF samples DH17 and DH19 to 5.5-8.8 kbar and 560-
855 590°C in middle LHF samples (Table 2). Although garnet compositional data is not available for
856 Upper LHF sample DH51, its mineral assemblage of coexisting staurolite and kyanite allows for
857 an approximation of rock conditions using only its bulk rock composition and observations
858 conditions where these mineral coexist (Figure 15E), which appears at ~ 7.0 kbar and $\sim 650^\circ\text{C}$.
859 Rim isopleths for GHC samples DH60, DH61, and DH66 yield similar P of ~ 7 kbar, but T
860 ranges from 550-600°C. GHC sample DH63 yields the highest P-T isopleth conditions of ~ 10.5
861 kbar and 650°C.

862 Comparisons are made between the conventional rim P-T conditions and isopleth rim
863 conditions. As seen in Figure 17B, the lower LHF samples yield higher T (by 25-30°C) and
864 lower P (by 1.4-2.3 kbar). All middle LHF samples (Figure 17D and F) overlap in P conditions
865 within uncertainty, but the isopleth T for samples DH22 and DH26 is higher than the
866 conventional results by 5-85°C, depending on how uncertainty is applied. For GHC sample
867 DH61, the approaches yield similar T conditions, but P differ by 1-2 kbar, depending on
868 uncertainty (Figure 17F). The opposite observation is seen with GHC sample DH66, where P is
869 similar, but the isopleth conditions suggest significantly lower T (Figure 17F). Some overlap is
870 seen with GHC sample DH63, but the conventional results suggest higher P-T than the isopleth
871 results.

872 **5 Discussion**

873 Using the same samples and data, Darondi Khola MCT footwall P-T paths using the
874 Gibb's method and high-resolution garnet modeling do not yield the same conditions or shapes
875 (Figure 17), even within the estimated uncertainties of the Gibb's method (e.g., Kohn, 1993). In
876 addition, the lowest-grade footwall samples record higher T and lower P isopleth rim P-T
877 conditions than those generated using conventional thermometers and barometers. Conventional
878 garnet rim P-T conditions and isopleth thermobarometry for GHC samples yield absolute
879 conditions that differ, although overlap exists within uncertainty ($\pm 25^\circ\text{C}$ and ± 1 kbar). An
880 important check on the feasibility of the P-T conditions generated using any approach is if the
881 results seem geologically reasonable and consistent with mineral assemblages (e.g., Moynihan
882 and Pattison, 2013; Kelly et al., 2015; Catlos et al., 2018; Etzel et al., 2019; Craddock Affinati et
883 al., 2020). However, this is the case with all conditions reported for the Darondi Khola samples,
884 regardless of approach.

885 Several assumptions underlie many P-T estimates generated using thermodynamic
886 modeling. For all thermobarometric methods applied here, a critical assumption is that the
887 minerals in a sample experienced equilibrium, which can never be proven for any rock system

888 (e.g., Spear & Peacock, 1989; Lanari & Duesterhoeft, 2019). The samples are also assumed to
889 have experienced closed system behavior, and the original compositions of the mineral phases
890 and the bulk rock have not changed significantly since metamorphism (e.g., Lanari and Engi,
891 2017). LHF assemblages appear to have preserved their original garnet compositions, as shown
892 by their prograde zoning profiles (Figure 10). Garnets with preserved divalent cation zoning
893 based on previously reported thermal conditions of generally $<600^{\circ}\text{C}$ (e.g., Carlson, 1989, Spear,
894 1993; Carlson 2002), consistent with the results shown here. GHC samples show fluctuations in
895 garnet compositions from core to rim and have evidence of diffusional modification by an
896 increase of Mn at the rims (Figure 11).

897 Multiple sources of error are inherent in conventional P-T conditions and include
898 uncertainty in the accuracy of end-member reactions, electron microprobe analyses, calibration
899 errors, variations in activity models, and compositional heterogeneity (e.g., Kohn & Spear,
900 1991). The precise uncertainty with approaches that involve isochemical phase diagrams is
901 likewise challenging to determine due to the same factors incorporated into their creation as well
902 as uncertainty associated with the thermodynamic properties inherent in the choice of internally
903 consistent database (e.g., molar enthalpy of formation, molar entropy, molar volume, heat
904 capacity, bulk modulus, Landau parameters, and Margules parameters, e.g., White et al., 2014;
905 Lanari & Duesterhoeft, 2019). The error suggested by the grid created due to overlapping
906 mineral compositional isopleths likely underestimates the actual uncertainty in the identified
907 conditions. Applying a standard values of uncertainty ($\pm 25^{\circ}\text{C}$ and ± 1 kbar) to the overlapping
908 isopleth conditions as those used for conventional results appears appropriate, and is commonly
909 reported (e.g., Spear & Peacock, 1989; Kohn, 1993; Kohn et al., 2001).

910 Ultimately, each approach to generating P-T conditions discussed here transforms the
911 sample into a model representing the true rock and mineral assemblage but restricts its behavior
912 as if it was in a closed system that experienced particular boundary conditions. Confidence in
913 conventional and Gibb's P-T paths increases when conditions agree with minerals assemblages
914 and if the P-T paths reproduce broad-scale trends in garnet zoning from core to rim. Samples
915 collected from the same outcrop or nearby should yield similar P-T conditions and paths.
916 Although Kohn et al. (2001) only report one Gibb's P-T path per sample, the expectation is that
917 multiple paths collected from the same garnet or multiple garnets in the same rock would agree
918 in terms of shapes and conditions. The high-resolution P-T path approach and the garnet isopleth
919 thermobarometry use these same criteria to evaluate the estimated result's appropriateness.
920 However, they have two additional values in critically evaluating results. First, a user can gauge
921 the extent of overlapping mineral isopleths in P-T space. Second, a user can identify how well
922 the high-resolution P-T paths predict the trends and values of garnet compositional zoning
923 (Figure 10). A significant value of the high-resolution P-T path and isopleth approaches is that a
924 user can detect when systems stray from the equilibrium and closed system assumptions.

925 These samples illustrate that not all garnets are suitable candidates for high-resolution P-
926 T path modeling and isopleth thermobarometry. Garnets with significant changes in composition
927 over short distances from core to the rim and those affected by diffusion cannot be modeled.
928 Garnets in samples that experienced significant changes in bulk composition or multiple
929 deformation episodes resulting in modification of composition are also unable to be modeled.
930 Not all field areas are ideal candidates, and the GHC samples show that they often fail
931 assumptions required for isopleth thermobarometry and high-resolution P-T path modeling. For
932 example, overlapping garnet core isopleths were only found for one GHC sample DH61, and this

933 was located far from the garnet-in reaction line (Figure 15C). In fact, the intersections for all
934 samples, except DH75A and DH75B, are far from the garnet-in reaction line (>1 vol%), although
935 all overlap mineral stability fields consistent with rock assemblages. The compositional core may
936 not coincide with the geometric garnet center (e.g., Spear & Daniel, 1998), shown for most
937 samples. Overlapping garnet compositional rim isopleths were found for three GHC samples
938 (DH61, DH63, DH66), but only GHC sample DH61 appears ideal as garnet rim isopleths also
939 intersect those of the matrix minerals (± 0.01 mole fraction Ca in anorthite and ± 0.01 Mg#
940 chlorite and biotite). Confidence in isopleth conditions increases when matrix mineral
941 compositions overlap the garnet rim conditions, as these mineral compositions are independent.

942 The high-resolution P-T paths should be considered approximations of how a garnet with
943 a specific type of compositional zoning would behave in a closed system of a known bulk
944 composition as it evolves during increasing T. Rocks are open systems, but LHF garnet-bearing
945 assemblages appear as if they approach an ideal scenario of a closed system. This appearance of
946 equilibrium is shown by overlapping isopleths of compositions from the garnet core and from
947 those of the garnet rim with matrix minerals. In addition, predictions of garnet zoning made by
948 the high-resolution P-T paths closely match the original garnet for these samples (Figure 10).
949 Multiple paths from the same sample yield similar conditions and shapes. The inability to
950 reproduce garnet zoning using Gibb's P-T path trajectories using TheraG modeling suggests
951 these paths may not be relevant to the samples using the applied parameters.

952 Regardless of calibrations used, the P-T conditions and paths along with previously-
953 reported timing constraints, are consistent with an imbrication model that suggest the MCT shear
954 zone developed as rock packages within the LHF were progressively transferred (Catlos et al.,
955 2001; Kohn et al., 2001). For example, Figure 18 shows P-T path predictions for one such
956 imbrication model described in Catlos et al. (2018) and (2020). In this model, thermobarometric
957 histories are calculated using a two-dimensional finite-difference solution to the diffusion-
958 advection equation. Samples within the LHF travel along the MCT at a 5 km/Ma speed rate from
959 25 to 18 Ma (Figure 18A). The hanging wall speed rate is 10 km/Ma, and topography
960 progressively accumulates until a maximum height of 3.5 km. The increase in topography is
961 required to accommodate the pressure changes recorded by the garnets while matching their
962 thermal histories. Once the topography is achieved at 18 Ma, a period of cessation is applied to
963 the MCT between 18 and 15 Ma, and topography is reduced at a rate of 1.5 km/Ma. The model
964 returns to activity within the MCT shear zone with the activation of the MCT footwall slivers
965 from 8 to 2 Ma (Figure 18B). P-T changes recorded by the footwall garnets are the direct result
966 of thermal advection combined with alterations in topography. Changes in the timing of fault
967 motion would affect the model outcomes. However, the model's current constraints and
968 boundary conditions appear to match the observed high-resolution P-T paths. For example, the
969 P-T diagram in Figure 18 C-E are model predictions for samples that experienced imbrication in
970 the MCT footwall. High-resolution P-T paths are also plotted in these panels from samples
971 collected from the LHF along the Darondi (Figure 18C) and Marsyangdi (Figure 18D) rivers in
972 central Nepal and from along the Bhagirathi River in NW India (Figure 18E). For most samples,
973 the P-T paths match the model predictions remarkably well. P-T paths for sample DH75B (Panel
974 18C) suggests the possibility of very high exhumation rates (>12mm/year) within the MCT shear
975 zone since the Pliocene, which is a scenario predicted by this imbrication model.

976 **6 Conclusions**

977 This paper reviews the geological framework of the Himalayas and describes and applies
 978 particular thermobarometric approaches to decipher the metamorphic history of garnet-bearing
 979 rocks collected across the MCT along the Darondi Khola in central Nepal using previously
 980 reported data (Kohn et al., 2001). A comparison is made between the results of conventional and
 981 isopleth thermobarometry for all samples and high-resolution and Gibb's P-T paths for MCT
 982 footwall rocks only. A significant value of the high-resolution P-T path and isopleth approaches
 983 is that a user can detect when systems stray from the equilibrium assumption. Confidence in
 984 conditions exists when mineral assemblages predicted by thermodynamic modeling appear
 985 consistent with the actual rock and when the P-T paths reproduce broad-scale trends in garnet
 986 zoning from core to rim. The expectation is that multiple paths collected from the same garnet or
 987 multiple garnets in the same rock would agree in terms of shapes and conditions and that samples
 988 collected from the same outcrop or nearby should record similar P-T conditions and paths. Using
 989 isopleth thermobarometry, a user can gauge the extent of overlapping mineral compositions and
 990 where the overlap occurs with respect to the garnet-in reaction line and garnet volume % growth
 991 contours. MCT footwall garnet compositions predicted by Gibb's P-T paths using the software
 992 package TheriaG fail to reproduce the original garnet zoning. However, high-resolution P-T
 993 paths reproduce the original garnet zoning to ± 0.01 mole fraction in most cases and for most
 994 compositions, expected if the garnet behaved in a closed system and had no significant changes
 995 in bulk rock composition as it grew. Although the assumption of equilibrium has long been
 996 known can never be proven for any rock system (e.g., Spear & Peacock, 1989), isopleth
 997 thermobarometry and high-resolution P-T path modeling applied to garnet-grade Himalayan
 998 MCT footwall assemblages show they appear to behave as if they evolved in a closed system that
 999 experienced particular P-T path trajectories. Ultimately, the P-T conditions and paths generated
 1000 for rocks across the MCT along the Darondi Khola, regardless of calibrations used, are consistent
 1001 with the imbrication model that suggest the MCT shear zone developed as rock packages within
 1002 the LHF were progressively transferred (Catlos et al., 2001; Kohn et al., 2001).

1003 **Figure Captions**

1004 **Figure 1.** Geological map of the Himalayas after Yin (2006). See Figure 2 for a cross-section
 1005 through central Nepal and Figure 3, Figure 4, and Figure 5 for the sample transect taken across
 1006 the MCT shear zone along the Darondi Khola.

1007 **Figure 2.** Generalized cross-section through the Himalayas in central Nepal after DeCelles
 1008 (2015) and Robinson et al. (2006). See additional cross-sections in the range in DeCelles et al.
 1009 (2020).

1010 **Figure 3.** Generalized geological map of the Annapurna-Manaslu-Ganesh region of central
 1011 Nepal after Colchen et al. (1980). Isograds are dashed and labeled: bt= biotite, grt= garnet; ky=
 1012 kyanite; sta= staurolite; sil= sillimanite; pyx= pyroxene, carbonate lithologies. STDS? = the
 1013 presence of the South Tibetan Detachment is debated; MCT= Main Central Thrust; MCT-I?= the
 1014 presence of Arita's (1983) thrust at the base of the MCT shear zone is debated.

1015 **Figure 4.** Sample location map from rocks collected along the Darondi Khola. The contour
 1016 interval is 500 ft. See Figure 3 for the location of this transect on the geological map of the
 1017 Himalayas. Samples are indicated by "DH#" in the text. Isograds are dashed and labeled (grt=
 1018 garnet; stau= staurolite). See Figure 5 for a cross-section along A-A'.

1019 **Figure 5.** Cross-section across the Darondi Khola section showing available muscovite $^{40}\text{Ar}/^{39}\text{Ar}$
 1020 and Th-Pb ages after Catlos et al. (2001). See Figure 4 for line of section.

1021 **Figure 6.** Cross-sections of early models of Himalayan inverted metamorphism and leucogranite
 1022 formation. (A) The “hot-iron” model of LeFort 1975. (B) Juxtaposing right-way-up metamorphic
 1023 isograds after Hubbard (1996). (C) A combination of models in panels (A) and (B) after Searle
 1024 and Rex (1989). Wedge extrusion models after (D) Hodges et al. (1993) and (E) Harris &
 1025 Massey (1994).

1026 **Figure 7.** Cross-sections of early kinematic models of Himalayan inverted metamorphism and
 1027 leucogranite formation. (A) After Molnar and England (1990). (B) After Huerta et al. (1998). (C)
 1028 After Harrison et al. (1989). (D) After Nelson et al. (1996).

1029 **Figure 8.** (A) An illustration of the critical taper model. (B) Schematic of channel flow and
 1030 wedge extrusion. (C) A combination of critical taper and tectonic wedging of the GHC. A “*”
 1031 indicates an incipient fault. (D) Illustration of GHC tectonic wedging after Webb et al. (2011).
 1032 Panels (E) and (F) show the final geometry of the range, which has affected the position and
 1033 definition of the MCT. Panels (A), (B), (C), and (E) are after Cottle et al. (2015), and panel (F) is
 1034 after Searle et al. (2008).

1035 **Figure 9.** Selected petrographic (plane polarized light) images of samples along the Darondi
 1036 Khola showing the relationship of the garnet porphyroblasts and rock textures. Garnets are
 1037 outlined using bold lines. Pressure shadows and inclusion trails are indicated by lighter and
 1038 dashed lines, respectively. Mineral abbreviations after Whitney and Evans (2010). Panels are
 1039 labeled with sample number. The scale bar for each image is 200 μ m. See Figure 4 and 5 for
 1040 sample locations.

1041 **Figure 10.** Compositional transects across garnets in lower LHF samples (A) DH17 and (B)
 1042 DH19, and middle LHF samples (C) DH22, (D) DH23, and (E) DH75B. Distance is in analytical
 1043 points, and the spacing between the points is $\sim 20 \mu$ m. The larger black squares are the raw
 1044 electron microprobe data, whereas the smaller black squares near the EPMA data points are the
 1045 smoothed data used for input into the model to generate the high-resolution P-T paths. The high-
 1046 resolution P-T paths predict garnet zoning, which is shown by the bold gray lines. TheriaG was
 1047 used to predict the garnet zoning for the Gibb’s P-T paths, and these are also indicated.

1048 **Figure 11.** Compositional transects across garnets in GHC samples DH66 (two transects) in (A)
 1049 spessartine, (C) grossular, (E) pyrope, and (G) almandine. Panels (B), (D), (F), and (H) are
 1050 compositional transects in spessartine, grossular, pyrope, and almandine, respectively, across a
 1051 garnet in sample DH61. Distance from the garnet core is in analytical points, and the spacing
 1052 between the points is $\sim 20 \mu$ m.

1053 **Figure 12.** Isochemical phase diagrams from lower LHF samples DH17 (A) garnet core and (B)
 1054 garnet rim, DH19 (C) core and (D) rim), and mid-LHF sample DH22 (E) core and (F) rim. See
 1055 Figures 4 and 5 for sample locations. Garnet-in reaction line (+Grt) and garnet growth contours
 1056 (volume 0.5% increments) are overlaid on each diagram. Each core diagram was created using
 1057 the rock bulk compositions reported in Table 3 and the software program Theriak-Domino. Some
 1058 mineral stability fields are labeled using abbreviations after de Capitani and Petrakakis (2010)
 1059 and include quartz and H₂O. For the core diagrams, isopleths of ± 0.01 - 0.02 mole fraction
 1060 spessartine (XMn), grossular (XCa), pyrope (XMg), almandine (XFe), and ± 0.01 - 0.02 Mg-
 1061 number (Mg/Fe+Mg, Mg#) of the compositional data point selected from the garnet’s highest
 1062 Mn content are overlain (Kohn et al., 2001). They intersect as indicated by the polygon and
 1063 labeled as “T-D core.” High-resolution P-T paths (DH17, n=2; DH19, n=2; DH22, n=1) were
 1064 generated from garnet core-to-rim transects after the approach of Moynihan & Pattison (2013).

1065 These are compared to the P-T paths obtained using the Gibb's method for the samples using the
 1066 same data by Kohn et al. (2001). The starting point of the Gibb's P-T paths is labeled with
 1067 "Gibb's core." Isochemical phase diagrams for the garnet rim were created using the final
 1068 effective bulk composition generated by Theriak-Domino. In this case, isopleths for the garnet
 1069 compositions reported for garnet rims are overlain on the diagram, as well as matrix mineral
 1070 compositions isopleths for An-content for plagioclase, Mg-number for biotite and chlorite,
 1071 (Mg/Fe+Mg, Mg#-bt and Mg#-chl) (Kohn et al. 2001), when available. They intersect as
 1072 indicated by the polygon and labeled as "T-D rim." These are compared to the rim P-T
 1073 conditions (GB-GBMP conditions) for the samples using the same data and conventional
 1074 thermobarometric approaches by Kohn et al. (2001).

1075 **Figure 13.** Isochemical phase diagrams from middle LHF samples DH23 (A) garnet core and
 1076 (B) rim and DH26 (C) core and (D) rim. See Figures 4 and 5 for sample locations. Detailed
 1077 caption is the same as in Figure 12. High-resolution P-T paths for sample DH23 were generated
 1078 from two garnet core-to-rim transects after the approach of Moynihan & Pattison (2013). These
 1079 are compared to the P-T paths obtained using the Gibb's method for the samples using the same
 1080 data by Kohn et al. (2001). No data was available for the garnet transect for sample DH26, so a
 1081 high-resolution P-T path was not created. In this case, the rock bulk composition (Table 3) was
 1082 used for both core and rim panels.

1083 **Figure 14.** Isochemical phase diagrams from middle LHF samples DH75A (A) garnet core and
 1084 (B) rim and DH75B (C) core and (D) rim. See Figures 4 and 5 for sample locations. Detailed
 1085 caption is the same as in Figure 12. High-resolution P-T paths for sample DH75B were generated
 1086 from garnet core-to-rim transects after the approach of Moynihan & Pattison (2013). These are
 1087 compared to the P-T paths obtained using the Gibb's method for the samples using the same data
 1088 by Kohn et al. (2001). The Gibb's path was also reported for sample DH75A. The starting point
 1089 of the Gibb's P-T paths is labeled with "Gibb's core." The isochemical phase diagram for the
 1090 garnet rim in sample DH75B was created using the final effective bulk composition generated by
 1091 Theriak-Domino. In this case, isopleths for the garnet compositions reported for garnet rims are
 1092 overlain on the diagram, as well as matrix mineral compositions isopleths for ± 0.01 An-content
 1093 for plagioclase (Kohn et al. 2001). Intersecting isopleths are indicated by the polygon and labeled
 1094 as "T-D rim." No data was available for the garnet transect for sample DH75A, so a high-
 1095 resolution P-T path was not created, and the rock bulk composition (Table 3) was used for both
 1096 core and rim panels. In the rim panels, data are compared to the conventional P-T conditions for
 1097 the samples (grey polygon) using the same data reported by Kohn et al. (2001).

1098 **Figure 15.** Isochemical phase diagrams from upper LHF samples DH58 (A) garnet core and (B)
 1099 rim and (E) DH51 showing the mineral reactions only. The figure also includes isochemical
 1100 phase diagrams from GHC sample DH61 (C) core and (D) rim, and DH60 (F) garnet rim data
 1101 only. See Figures 4 and 5 for sample locations. Garnet-in reaction line (+Grt) and garnet growth
 1102 contours (volume 0.5% increments) are overlaid on each diagram. Each diagram was created
 1103 using the rock bulk compositions reported in Table 3 and the software program Theriak-Domino.
 1104 Detailed caption is the same as in Figure 12. All labeled stability fields include quartz and H₂O,
 1105 except in panel (B), where the quartz-out reaction line is noted. The isopleths did not intersect in
 1106 panels (B) and (F) but did in panel (D), as indicated by the polygon labeled as "T-D rim." In the
 1107 rim panels, data are compared to the rim P-T conditions for the samples (labeled polygon) using
 1108 the same data and conventional thermobarometric approaches by Kohn et al. (2001). No mineral
 1109 data is available for sample DH51, so the isochemical phase diagram in panel (E) shows only

1110 reaction lines with staurolite, sillimanite, garnet, and kyanite reaction lines in bold. This sample
 1111 has co-existing kyanite and staurolite, so the shaded area indicates the field where both of these
 1112 minerals are stable.

1113 **Figure 16.** Isochemical phase diagrams from GHC samples (A) DH63, (B) DH66, and (C)
 1114 DH67. See Figures 4 and 5 for sample locations. Garnet-in reaction line (+Grt) and garnet
 1115 growth contours (volume 0.5% increments) are overlaid on each diagram. Each diagram was
 1116 created using the rock bulk compositions reported in Table 3 and the software program Theriak-
 1117 Domino. Some mineral stability fields are labeled using abbreviations after de Capitani and
 1118 Petrakakis (2010). All labeled stability fields include quartz and H₂O. For each diagram,
 1119 isopleths of ± 0.01 - 0.02 mole fraction spessartine (XMn), grossular (XCa), pyrope (XMg),
 1120 almandine (XFe), and ± 0.01 - 0.02 Mg-number (Mg/Fe+Mg, Mg#) of the compositional data
 1121 point selected from the garnet's rim are overlain (Kohn et al., 2001). Isopleths of An-content for
 1122 matrix plagioclase (A) and Mg# for matrix chlorite are also overlaid on the diagrams in panels
 1123 (A) and (C), respectively. Mineral isopleths intersect in panels (A) and (B) as indicated by the
 1124 polygon and labeled as "T-D rim." These isopleths did not intersect in panel (C). In each panel,
 1125 data are compared to the rim P-T conditions for the samples (grey polygon) using the same data
 1126 and conventional thermobarometric approaches by Kohn et al. (2001).

1127 **Figure 17.** Summary of the P-T conditions and paths reported in Figures 12-16. In panels (A),
 1128 (C), and (E), Gibb's P-T paths are shown as bold arrows and high-resolution P-T paths are
 1129 labeled with core and rim points. In panels (B), (D), and (F), rim data generated using isopleth
 1130 (white polygons) and conventional thermobarometry (grey polygons) are compared. Uncertainty
 1131 scales in T ($\pm 25^\circ\text{C}$) and P (± 1 kbar) are shown as insets in each panel.

1132 **Figure 18.** (A) Thermal-kinematic model cross-section after Catlos et al. (2018) showing the
 1133 MCT (dark line) and MBT (white line) from 25 to 8 Ma. The MCT and MBT sole into the MHT
 1134 at depth. Isothermal sections in degree increments are indicated by the scale bar. The isotherms
 1135 show the thermal situation at 18 Ma after MCT slip. Example sample trajectories on the diagram
 1136 are represented by arrows with dots at the initial and heads at the final position. The MCT is
 1137 active from 25 to 18 Ma, whereas slip transfers to the MBT from 15 to 8 Ma. (B) The model
 1138 cross-section of the reactivation of the MCT shear zone from 8 to 2 Ma. Both the MCT and
 1139 MCT-I sole into the MHT at depth. This panel represents the thermal situation at 6 Ma right
 1140 before the development of MCT shear zone inverted metamorphism. Example sample
 1141 trajectories are shown. (C) P-T diagram showing the trajectories of the model predictions for
 1142 samples panels A and B and high-resolution P-T paths for the Darondi Khola samples. Sample
 1143 DH75B is identified. Panels (D) and (E) show the same model predictions but high-resolution P-
 1144 T paths from the Marsyangdi River (Catlos et al., 2018) and Bhagirathi River transects (Catlos et
 1145 al., 2020).

1146 Acknowledgments

1147 I appreciate Matt Kohn (Boise State University) for supplying the data from the Darondi Khola
 1148 samples and Mark Harrison (UCLA) for access to the rock samples so they could be subjected to
 1149 further analysis. Discussions and assistance from Eric D. Kelly helped to refine the ideas in the
 1150 manuscript. I thank Theresa Perez (UT Austin), who helped in generating some of the P-T
 1151 diagrams and Jeffrey Horowitz (UT Austin) for drafting assistance. Comments from two
 1152 reviewers improved the original version.

1153 Data Availability Statement

1154 Supplementary data used in the paper will be made available in the Texas Data Repository, a
1155 platform for publishing and sharing datasets, and is included here for review purposes only.

1156 **References**

- 1157 Abrajewitch, A.V., Ali, J., Aitchison, J.C., Badengzhu, Davis, A.M., Liu, J. & Ziabrev, S.V.
1158 (2005). Neotethys and the India–Asia collision: insights from a palaeomagnetic study of
1159 the Dazhuqu ophiolite, southern Tibet. *Earth and Planetary Science Letters*, 233, 87–102.
- 1160 Acharyya, S.K. (1994). The Cenozoic foreland basin and tectonics of the eastern sub-Himalaya:
1161 problems and prospects. *Himalayan Geology*, 15, 3– 21.
- 1162 Aharon, P., Schidlowski, M. & Singh, I. (1987). Chronostratigraphic markers in the end-
1163 Precambrian carbon isotope record of the Lesser Himalaya. *Nature*, 327, 699–702.
1164 <https://doi.org/10.1038/327699a0>
- 1165 Ahmad, T., Harris, N., Bickle, M., Chapman, H., Bunbury, J., & Prince, C. (2000). Isotopic
1166 constraints on the structural relationships between the Lesser Himalayan Series and High
1167 Himalayan Crystalline Series, Garhwal Himalaya. *Geological Society of America*
1168 *Bulletin*, 112, 467-477.
- 1169 Ahmad, T., Mukherjee P.K., & Trivedi, J.R. (1999). Geochemistry of Precambrian mafic
1170 magmatic rocks of the Western Himalaya, India: petrogenetic and tectonic implications.
1171 *Chemical Geology*, 160, 103-119.
- 1172 Aikman, A.B., Harrison, T.M., & Lin, D. (2008). Evidence for Early (>44 Ma) Himalayan
1173 crustal thickening, Tethyan Himalaya, southeastern Tibet. *Earth and Planetary Science*
1174 *Letters*, 274, 14-23. <https://doi.org/10.1016/j.epsl.2008.06.038>
- 1175 Aitchison, J.C., & Badengzhu, Davis, A.M., Liu, J., Luo, H., Malpas J.G., McDermid, I.R.C.,
1176 Wu, H., Ziabrev, S.V., & Zhou, M-f. (2000). Remnants of a Cretaceous intra-oceanic
1177 subduction system within the Yarlung–Zangbo suture (southern Tibet). *Earth and*
1178 *Planetary Science Letters*, 183, 231–244.
- 1179 Aitchison, J.C., Ali, J.R., & Davis, A.M. (2007). When and where did India and Asia collide?
1180 *Journal of Geophysical Research*, 112, B05423. <https://doi.org/10.1029/2006JB004706>
- 1181 Allègre, C.J., et al. (1984). Structure and evolution of the Himalayan–Tibet orogenic belt.
1182 *Nature*, 307, 17-22.
- 1183 Anczkiewicz, R., Chakraborty, S., Dasgupta, S., Mukhopadhyay, D., & Kołtonik, K. (2014).
1184 Timing, duration and inversion of prograde Barrovian metamorphism constrained by high
1185 resolution Lu–Hf garnet dating: A case study from the Sikkim Himalaya, NE India. *Earth*
1186 *and Planetary Science Letters*, 407, 70-81. <https://doi.org/10.1016/j.epsl.2014.09.035>
- 1187 Arita, K. (1983). Origin of the inverted metamorphism of the Lower Himalaya, central Nepal.
1188 *Tectonophysics*, 95, 43-60.
- 1189 Auden, M.A. (1937). The structure of the Himalaya in Garhwal. *Records of the Geological*
1190 *Survey of India*, 71, 407-433.
- 1191 Bai, L., Liu, H.B., Ritsema, J. Mori, J., Zhang, T.Z., Ishikawa, Y., & Li, G.H. (2016). Faulting
1192 structure above the Main Himalayan Thrust as shown by relocated aftershocks of the
1193 2015 Mw7.8 Gorkha, Nepal, earthquake. *Geophysical Research Letters*, 43, 637-642.
1194 <https://doi.org/10.1002/2015GL066473>
- 1195 Bassoullet, J.P., Colchen, M., Juteau, T., Marcoux, J., & Mascle, G. (1980). L’edifice de nappes
1196 du Zaskar (Ladakh, Himalaya). *Comptes rendus de l’Académie des Sciences, Series D*,
1197 290, 389-392.

- 1198 Baxter, A.T., Aitchison, J.C., Ali, J.R., Chan, J.S.-L., & Chan, G.H.N. (2016). Detrital chrome
 1199 spinel evidence for a Neotethyan intra-oceanic island arc collision with India in the
 1200 Paleocene. *Journal of Asian Earth Sciences*, 128, 90–104.
- 1201 Beaumont, C., Nguyen, M., Jamieson, R., & Ellis, S. (2006). Crustal flow modes in large hot
 1202 orogens. In: Law, R.D., & Searle, M.P., & Godin, L. (Eds). *Channel Flow, Ductile*
 1203 *Extrusion and Exhumation in Continental Collision Zones*. Geological Society, London,
 1204 *Special Publications*, 268, 91–146.
- 1205 Beaumont, C., & Jamieson, R.A. (2010). Himalayan-Tibetan orogeny: channel flow versus
 1206 (critical) wedge models, a false dichotomy, in Leech, M.L., and others, eds., *Proceedings*
 1207 *for the 25th Himalaya-Karakoram-Tibet Workshop* : U.S. Geological Survey, Open-File
 1208 *Report 2010-1099*, 2p. <http://pubs.usgs.gov/of/2010/1099/beaumont>
- 1209 Beaumont, C., Jamieson, R.A., Nguyen, M.H., & Lee, B. (2001). Himalayan tectonics explained
 1210 by extrusion of a low-viscosity crustal channel coupled to focused surface denudation.
 1211 *Nature*, 414, 738–742.
- 1212 Beaumont, C., Jamieson, R.A., Nguyen, M.H., & Medvedev, S. (2004). Crustal channel flows: 1.
 1213 Numerical models with applications to the tectonics of the Himalayan–Tibetan orogen.
 1214 *Journal of Geophysical Research*, 109. <https://doi.org/10.1029/2003JB002809>
- 1215 Benetti, B., Montomoli, C., Iaccarino, S., Langone, A., & Carosi, R. (2021). Mapping tectono-
 1216 metamorphic discontinuities in orogenic belts: implications for mid-crust exhumation in
 1217 NW Himalaya. *Lithos*, 392–393. <https://doi.org/10.1016/j.lithos.2021.106129>.
- 1218 Berman, R.G. (1990). Mixing properties of Ca-Mg-Fe-Mn garnets. *American Mineralogist*, 75,
 1219 328-344.
- 1220 Bhandari, S., Xiao, W., Ao, S., Windley, B.F., Zhu, R., Li, R., Wang, H.Y.C., & Esmaili, R.
 1221 (2019). Rifting of the northern margin of the Indian craton in the Early Cretaceous:
 1222 Insight from the Aulis Trachyte of the Lesser Himalaya (Nepal). *Lithosphere*, 11(5), 643–
 1223 651. <https://doi.org/10.1130/L1058.1>
- 1224 Bhargava, O.N., & Bassi, U.K. (1994). The crystalline thrust sheets of the Himachal Himalaya
 1225 and the age of amphibolite facies metamorphism. *Journal of the Geological Society of*
 1226 *India*, 43, 343-352.
- 1227 Bhargava, O.N., & Singh, B.P. (2020). Geological evolution of the Tethys Himalaya. *Episodes*,
 1228 43(1), 404-416. <https://doi.org/10.18814/epiugs/2020/020025>
- 1229 Bhargava, O.N., Frank, W., & Bertle, R. (2011). Late Cambrian deformation in the Lesser
 1230 Himalaya. *Journal Asian Earth Sciences*, 40, 201–212.
- 1231 Bhutani, R., Pande, K. & Venkatesan, T.R. (2004). Tectono-thermal evolution of India–Asia
 1232 collision zone based on ^{40}Ar – ^{39}Ar thermochronology in Ladakh, India. *Proceedings of the*
 1233 *Indian Academy of Sciences (Earth and Planetary Sciences)*, 113, 737–754.
- 1234 Bilham, R., Larson, K., Freymueller, J., & Project Idylhim members (1997). GPS measurements
 1235 of present-day convergence across the Nepal Himalaya. *Nature*, 386, 61-64.
- 1236 Bodenhausen, J.W.A., DeBooy, T., Egelar, C.G., & Nijhuis, H.J. (1964). On the geology of
 1237 Central west Nepal- A preliminary note. 22nd International Geological Congress, New
 1238 Delhi. *Special publication*, 11, 101–122.
- 1239 Bollinger, L., Avouac, J., Cartin, R., & Pandey, M.R. (2004). Stress buildup in the Himalaya.
 1240 *Journal of Geophysical Research*, 109, 1-8. <https://doi.org/10.1029/2003JB002911>
- 1241 Bollinger, L., Henry, P., & Avouac, J.P. (2006). Mountain building in the Nepal Himalaya:
 1242 Thermal and kinematic model. *Earth and Planetary Science Letters*, 244, 58–71.

- 1243 Bollinger, L., Soma Nath Sapkota, S.N., P. Tapponnier, P., Yann Klinger, Y., Magali Rizza, M.,
1244 et al. (2014). Estimating the return times of great Himalayan earthquakes in eastern
1245 Nepal: Evidence from the Patu and Bardibas strands of the Main Frontal Thrust. *Journal*
1246 *of Geophysical Research*, 119(9), 7123-7163.
- 1247 Bora, D. S., & Shukla, U. K. (2005). Petrofacies implication for the Lower Siwalik Foreland
1248 Basin evolution, Kumaun Himalaya, India. *Special Publication of the Palaeontological*
1249 *Society of India*, 2, 163–179.
- 1250 Bordet, P., Colchen, M., & LeFort. P. (1971). Esquisse géologique = Geological sketch map Nyi-
1251 Shang (Népal central) / Mission géologiques du centre national de la recherche
1252 scientifique (R.C.P. Nepal) avec le patronage de la Fédération française de la montagne et
1253 du Club Alpin ; les contours géologiques ont été levés par P. Bordet, M. Colchen, P. Le
1254 Fort, ca. 1:75 000 (E 83°50'--E 84°15'/N 28°49'--N 28°32').
1255 <https://www.sudoc.fr/131377973>
- 1256 Bordet, P., Colchen, M., & LeFort. P. (1975). *Recherches géologiques dans l'Himalaya du Nepal,*
1257 *region du Nyi-Shang. Paris Centre National de la Recherche Scientifique*, 138pp.
- 1258 Braden, Z., Godin, L., & Cottle, J.M. (2017). Segmentation and rejuvenation of the Greater
1259 Himalayan sequence in western Nepal revealed by in situ U–Th/Pb monazite
1260 petrochronology, *Lithos*, 284–285, 751-765. <https://doi.org/10.1016/j.lithos.2017.04.023>
- 1261 Braden, Z., Godin, L., Cottle, J., & Yakymchuk, C. (2018). Renewed late Miocene (< 8 Ma),
1262 hinterland ductile thrusting, western Nepal Himalaya. *Geology*, 46, 503-506.
- 1263 Brookfield, M.E. (1993). The Himalayan passive margin from Precambrian to Cretaceous.
1264 *Sedimentary Geology*, 84, 1–35.
- 1265 Brookfield, M.E., & Reynolds, P.H. (1981). Late Cretaceous emplacement of the Indus suture
1266 zone ophiolitic melanges and an Eocene–Oligocene magmatic arc on the northern edge of
1267 the Indian plate. *Earth and Planetary Science Letters*, 55, 157–162.
- 1268 Brunel, M. & Kienast, J.R. (1986). Etude pétro-structurale des chevauchements ductiles
1269 himalayens sur la transversale de l'Everest-Makalu (Nepal oriental). *Canadian Journal of*
1270 *Earth Sciences*, 23, 1117-1137.
- 1271 Burchfiel, C.B., Zhiliang C., Hodges K.V., Yuping L., Royden L.H., Changrong D., & Jiene X.
1272 (1992). The South Tibetan Detachment System, Himalayan orogen: extension
1273 contemporaneous with and parallel to shortening in a collisional mountain belt. *USGS*
1274 *Special Paper*, 269, 1-40.
- 1275 Burg, J.-P. (2011). The Asia–Kohistan–India collision: Review and discussion. In: Brown, D. &
1276 Ryan, P.D. (eds) *Arc–Continent Collision. Frontiers in Earth Sciences*. Springer, Berlin,
1277 279–309.
- 1278 Burg, J.-P., Brunel, M., Gapais, D., Chen G.M., & Liu, G.H. (1984). Deformation of
1279 leucogranites of the crystalline Main Central Sheet in southern Tibet (China). *Journal of*
1280 *Structural Geology*, 6, 535-542.
- 1281 Burg, J.-P., Leyrelop, A., Girardeau, J., & Chen, G.M. (1987). Structure and metamorphism of
1282 a tectonically thickened continental crust—the Yalu Tsangpo suture zone (Tibet).
1283 *Philosophical Transactions of the Royal Society of London Series A*, 321, 67– 86.
- 1284 Burgess, W.P., Yin, A., Dubey, C.S., Shen, Z-K., & Kelty, T.K. (2012). Holocene shortening
1285 across the Main Frontal Thrust zone in the eastern Himalaya. *Earth and Planetary Science*
1286 *Letters*, 357–358, 152-167. <https://doi.org/10.1016/j.epsl.2012.09.040>
- 1287 Caddick, M.J., Bickle, M.J., Harris, N.B.W., Holland, T.J.B., Horstwood, M.S.A., Parrish, R.R.,
1288 & Ahmad, T. (2007). Burial and exhumation history of a Lesser Himalayan schist:

- 1289 recording the formation of an inverted metamorphic sequence in NW India. *Earth and*
 1290 *Planetary Science Letters*, 264, 375-90. <https://doi.org/10.1016/j.epsl.2007.09.011>
- 1291 Caldwell, W.B., Klemperer, S.L., Lawrence, J.F., & Rai, S.S. (2013). Characterizing the Main
 1292 Himalayan Thrust in the Garhwal Himalaya, India with receiver function CCP stacking.
 1293 *Earth and Planetary Science Letters*, 367, 15-27.
 1294 <https://doi.org/10.1016/j.epsl.2013.02.009>
- 1295 Cao, H., Huang, Y., Li, G., Zhang, L., Wu, J., Dong, L., Dai, Z., & Lu, L. (2018). Late Triassic
 1296 sedimentary records in the northern Tethyan Himalaya: Tectonic link with Greater India.
 1297 *Geoscience Frontiers*, 9(1), 273-291. <https://doi.org/10.1016/j.gsf.2017.04.001>
- 1298 Carlson, W. D. (1989). The significance of intergranular diffusion to the mechanisms and
 1299 kinetics of porphyroblast crystallization. *Contributions to Mineralogy and Petrology*, 103,
 1300 1–24.
- 1301 Carlson, W. D. (2002). Scales of disequilibrium and rates of equilibration during metamorphism.
 1302 *American Mineralogist*, 87, 185–204.
- 1303 Carosi, R., Lombardo, B., Molli, G., Musumeci, G., & Pertusati, P.C. (1998). The South Tibetan
 1304 Detachment System in the Rongbuk valley, Everest region. Deformation and geological
 1305 implications. *Journal of Asian Earth Sciences*, 16, 299-311.
- 1306 Carosi, R., Lombardo, B., Musumeci, G., & Pertusati, P.C. (1999a). Geology of the Higher
 1307 Himalayan Crystallines in Khumbu Himal (eastern Nepal). *Journal of Asian Earth*
 1308 *Sciences*, 17, 785-803.
- 1309 Carosi, R., Montomoli, C., & Iaccarino, S. (2018). 20 years of geological mapping of the
 1310 metamorphic core across Central and Eastern Himalayas. *Earth-Science Reviews*, 177,
 1311 124–138. <https://doi.org/10.1016/j.earscirev.2017.11.006>
- 1312 Carosi, R., Montomoli, C., Iaccarino, S., Massonne, H. J., Rubatto, D., Langone, A., et al.
 1313 (2016). Middle to late Eocene exhumation of the Greater Himalayan sequence in the
 1314 central Himalayas: Progressive accretion from the Indian plate. *Bulletin of the Geological*
 1315 *Society of America*, 128, 1571–1592. <https://doi.org/10.1130/B31471.1>
- 1316 Carosi, R., Montomoli, C., Rubatto, D., & Visonà, D. (2010). Late Oligocene high-temperature
 1317 shear zones in the core of the Higher Himalayan Crystallines (Lower Dolpo, western
 1318 Nepal), *Tectonics*, 29, TC4029. <https://doi.org/10.1029/2008TC002400>
- 1319 Carosi, R., Montomoli, C., Rubatto, D., & Visonà, D. (2013). Leucogranite intruding the South
 1320 Tibetan Detachment in western Nepal: implications for exhumation models in the
 1321 Himalayas. *Terra Nova*, 25, 478– 489, 2013
- 1322 Carosi, R., Musumeci, G., & Pertusati, P.C. (1999b). Extensional tectonics in the higher
 1323 Himalayan crystallines of Khumbu Himal, Eastern Nepal. In Macfarlane, A., Sorkhabai,
 1324 R.B., and Quade, J. (Eds.), *Himalaya and Tibet: Mountain roots to mountain tops*.
 1325 *Geological Society of America Special Paper*, 328, pp. 211-223.
- 1326 Catlos, E.J. (2013). Versatile Monazite: resolving geological records and solving challenges in
 1327 materials science: Generalizations about monazite: Implications for geochronologic
 1328 studies. *American Mineralogist*, 98 (5-6), 819–832. <https://doi.org/10.2138/am.2013.4336>
- 1329 Catlos, E.J., Dubey, C.S., Marston, R.A., & Harrison, T.M. (2007). Geochronologic constraints
 1330 across the Main Central Thrust shear zone, Bhagirathi River (NW India): Implications for
 1331 Himalayan tectonics. In M. Cloos, W.D. Carlson, M.C. Gilbert, J.G. Liou, S.S. Sorensen,
 1332 Eds., *Convergent Margin Terranes and Associated Regions: A Tribute to W.G. Ernst*.
 1333 *Geological Society of America Bulletin*, 419, 135-151. <https://doi.org/10.1130/SPE419>

- 1334 Catlos, E. J., Perez, T. J., Lovera, O. M., Dubey, C. S., Schmitt, A. K., & Etzel, T. M. (2020).
 1335 High-resolution P-T-Time paths across Himalayan faults exposed along the Bhagirathi
 1336 transect NW India: Implications for the construction of the Himalayan orogen and
 1337 ongoing deformation. *Geochemistry, Geophysics, Geosystems*, 21, e2020GC009353.
 1338 <https://doi.org/10.1029/2020GC009353>
- 1339 Catlos, E.J., Harrison, T.M., Kohn, F.J., Grove, Z.M., Ryerson, F.J., Manning, C.E., & Upreti,
 1340 B.N. (2001). Geochronologic and thermobarometric constraints on the evolution of the
 1341 Main Central Thrust, central Nepal Himalaya. *Journal of Geophysical Research*, 106,
 1342 16177-16204. <https://doi.org/10.1029/2000JB900375>
- 1343 Catlos, E.J., Harrison, T.M., Manning, C.E., Grove, M., Rai, S.M., Hubbard, M.S., & Upreti,
 1344 B.N. (2002). Records of the evolution of the Himalayan Orogen from in situ Th-Pb ion
 1345 microprobe dating of monazite; eastern Nepal and western Garhwal. *Journal of Asian
 1346 Earth Sciences*, 20, 459-479. [https://doi.org/10.1016/S1367-9120\(01\)00039-6](https://doi.org/10.1016/S1367-9120(01)00039-6)
- 1347 Catlos, E.J., Lovera, O.M., Kelly, E.D., Ashley, K.T., Harrison, T.M., & Etzel, T. (2018).
 1348 Modeling High-resolution Pressure-Temperature paths across the Himalayan Main
 1349 Central Thrust (central Nepal): Implications for the dynamics of collision. *Tectonics*, 37,
 1350 2363-2388.
- 1351 Catlos, E.J., Pease, E.C., Dygert, N., Brookfield, M., Schwarz, W.H., Bhutani, R., Pande, K., &
 1352 Schmitt, A.K. (2019). Nature, age and emplacement of the Spongtang ophiolite, Ladakh,
 1353 NW India. *Journal of the Geological Society*, 176, 284-305.
 1354 <https://doi.org/10.1144/jgs2018-085>
- 1355 Cattin, R., & Avouac, J. (2000). Modeling mountain building and the seismic cycle in the
 1356 Himalaya of Nepal. *Journal of Geophysical Research*, 105, 13389-13407.
 1357 <https://doi.org/10.1029/2000JB900032>
- 1358 Cawood, P.A., Johnson, M.R.W., & Nemchin, A.A. (2007). Early Palaeozoic orogenesis along
 1359 the Indian margin of Gondwana: Tectonic response to Gondwana assembly. *Earth and
 1360 Planetary Science Letters*, 255, 70-84. <https://doi.org/10.1016/j.epsl.2006.12.006>
- 1361 Chakraborty, S., Anczkiewicz, R., Gaidies, F., Rubatto, D., Sorcar, N., Faak, K., Mukhopadhyay,
 1362 D., & Dasgupta D. (2016). A review of thermal history and timescales of
 1363 tectonometamorphic processes in Sikkim Himalaya (NE India) and implications for rates
 1364 of metamorphic processes. *Journal of Metamorphic Geology*, 34, 785-803.
 1365 <https://doi.org/10.1111/jmg.12200>
- 1366 Chakraborty, S., Mukul, M., Mathew, G., & Pande, K. (2019). Major shear zone within the
 1367 Greater Himalayan Sequence and sequential evolution of the metamorphic core in
 1368 Sikkim, India. *Tectonophysics*, 770, 228183. <https://doi.org/10.1016/j.tecto.2019.228183>
- 1369 Chen, X., Schertl, H-P., Gu, P., Zheng, Y., Xu, R., Zhang, J., Cai, P., & Lin, C. (2021). Newly
 1370 discovered MORB-Type HP garnet amphibolites from the Indus-Yarlung Tsangpo suture
 1371 zone: Implications for the Cenozoic India-Asia collision, *Gondwana Research*, 90, 102-
 1372 117. <https://doi.org/10.1016/j.gr.2020.11.006>
- 1373 Chirouze, F., Dupont-Nivet, G., Huyghe, P., van der Beek, P., Chakraborti, T., Bernet, M., &
 1374 Erens, V. (2012). Magnetostratigraphy of the Neogene Siwalik Group in the far eastern
 1375 Himalaya: Kameng section, Arunachal Pradesh, India. *Journal of Asian Earth Sciences*,
 1376 44, 117-135. <https://doi.org/10.1016/j.jseaes.2011.05.016>
- 1377 Colchen, M., Le Fort, P., and Pêcher, A. (1980). Annapurna-Manaslu-Ganesh Himal, Centre
 1378 National de la Recherches Scientifiques, Paris, 136pp.

- 1379 Coleman, M.E. (1996). Orogen-parallel and orogen-perpendicular extension in the central
1380 Nepalese Himalayas. *Geological Society of America Bulletin*, 108, 1594-1607.
- 1381 Coleman, M.E., & Hodges, K.V. (1998). Contrasting Oligocene and Miocene thermal histories
1382 from the hanging wall and footwall of the South Tibetan detachment in the central
1383 Himalaya from $^{40}\text{Ar}/^{39}\text{Ar}$ thermochronology, Marsyandi Valley, central Nepal. *Tectonics*,
1384 17(5), 726– 740. <https://doi.org/10.1029/98TC02777>.
- 1385 Cooper, F.J., Adams, B.A., Edwards, C.S., & Hodges, K.V. (2012). Large normal-sense
1386 displacement on the South Tibetan fault system in the eastern Himalaya. *Geology*, 40
1387 (11), 971–974. <https://doi.org/10.1130/G33318.1>
- 1388 Copley, A., Avouac, J.-P., & Royer, J.-Y. (2010). India-Asia collision and the Cenozoic
1389 slowdown of the Indian plate: Implications for the forces driving plate motions. *Journal*
1390 *of Geophysical Research*, 115, B03410. <https://doi.org/10.1029/2009JB006634>
- 1391 Corfield, R.L., & Seale, M.P. (2000). Crustal shortening across the north Indian continental
1392 margin, Ladakh, India. In: Khan, M.A., Treloar, P.J., Searle, M.P., Jan, M.Q. (Eds.),
1393 *Tectonics of the Nanga Parbat syntaxis and the Western Himalaya*. The Geological
1394 Society Special Publication, vol. 170, pp. 395– 410.
- 1395 Corrie, S.L., & Kohn, M.J. (2011). Metamorphic history of the central Himalaya, Annapurna
1396 region, Nepal, and implications for tectonic models, *Geological Society of America*
1397 *Bulletin*, 123(9–10), 1863– 1879.
- 1398 Corrie, S.L., Kohn, M.J., McQuarrie, N., & Long S. (2012). Flattening the Bhutan Himalaya.
1399 *Earth and Planetary Science Letters*, 349-350, 67-74.
- 1400 Corrie, S.L., Kohn, M.J., & Vervoort, J.D. (2010). Young eclogite from the Greater Himalayan
1401 Sequence, Arun Valley, eastern Nepal; P-T-t path and tectonic implications. *Earth and*
1402 *Planetary Science Letters*, 289, 406-416. <https://doi.org/10.1016/j.epsl.2009.11.029>
- 1403 Cottle, J.M., Larson, K.P., & Kellett, D.A. (2015). How does the mid-crust accommodate
1404 deformation in large, hot collisional orogens? A review of recent research in the
1405 Himalayan orogen. *Journal of Structural Geology*, 78, 119-133.
1406 <https://doi.org/10.1016/j.jsg.2015.06.008>
- 1407 Cottle, J.M., Searle, M.P., Horstwood, M.S.A. & Waters, D. (2009). Timing of midcrustal
1408 metamorphism, melting, and deformation in the Mount Everest region of south Tibet
1409 revealed by U(-Th)-Pb geochronology. *The Journal of Geology*, 117, 643–664.
- 1410 Craddock Affinati, A., Hoisch, T.D., Wells, M.L., & Vervoort, J.D. (2020). Pressure-
1411 temperature-time paths from the Funeral Mountains, California, reveal Jurassic retroarc
1412 underthrusting during early Sevier orogenesis. *Geological Society of America Bulletin*,
1413 132 (5-6), 1047–1065. <https://doi.org/10.1130/B35095.1>
- 1414 Crouzet, C., Dunkl, I., Paudel, L., Árkai, P., Rainer, T.M., Balogh, K., & Appel, E. (2007).
1415 Temperature and age constraints on the metamorphism of the Tethyan Himalaya in
1416 Central Nepal: A multidisciplinary approach. *Journal of Asian Earth Sciences*, 30(1),
1417 113-130. <https://doi.org/10.1016/j.jseaes.2006.07.014>
- 1418 Dai, J.-G., Wang, C.-S., Hébert, R., Santosh, M., Li, Y.-L. & Xu, J.-Y. (2011). Petrology and
1419 geochemistry of peridotites in the Zhongba ophiolite, Yarlung Zangbo Suture Zone:
1420 Implications for the Early Cretaceous intra-oceanic subduction zone within the Neo-
1421 Tethys. *Chemical Geology*, 288, 133–148.
- 1422 Daniel, C.G., Hollister, L.S., Parrish, R.R., & Grujic, D. (2003). Exhumation of the Main Central
1423 Thrust from lower crustal depths, eastern Bhutan Himalaya. *Journal of Metamorphic*
1424 *Geology*, 21(4), 317–334. <https://doi.org/10.1046/j.1525-1314.2003.00445.x>

- 1425 Dasgupta, S., Ganguly, J., & Neogi, S. (2004). Inverted metamorphic sequence in the Sikkim
1426 Himalayas: crystallization history, P–T gradient and implications. *Journal of*
1427 *Metamorphic Geology*, 22, 395–412. <https://doi.org/10.1111/j.1525-1314.2004.00522.x>
- 1428 de Capitani, C., & Brown, T.H. (1987). The computation of chemical equilibrium in complex
1429 systems containing non-ideal solutions. *Geochimica et Cosmochimica Acta*, 51, 2639–
1430 2652.
- 1431 de Capitani, C., & Petrakakis, K. (2010). The computation of equilibrium assemblage diagrams
1432 with Theriak/Domino software. *American Mineralogist*, 95, 1006–1016.
1433 <https://doi.org/10.2138/am.2010.3354>
- 1434 DeCelles, P.G. (2015). Structural-kinematic setting of the 2015 Gorkha, Nepal earthquakes:
1435 Lessons from a critically tapered orogenic wedge. 2015 GSA Annual Meeting in
1436 Baltimore, Maryland, USA (1–4 November 2015), Paper No. 105–9.
1437 <https://gsa.confex.com/gsa/2015AM/webprogram/Paper266639.html>
- 1438 DeCelles, P.G., Carrapa, B., Ojha, T.P., Gehrels, G.E., & Collins, D. (2020). Structural and
1439 Thermal Evolution of the Himalayan Thrust Belt in Midwestern Nepal. *Geological*
1440 *Society of America Special Paper*, 547, 1–77. [https://doi.org/10.1130/2020.2547\(01\)](https://doi.org/10.1130/2020.2547(01))
- 1441 DeCelles, P.G., Gehrels, G.E., Najman, Y., Martin, A.J., Carter, A., & Garzanti, E. (2004).
1442 Detrital geochronology and geochemistry of Cretaceous–Early Miocene strata of Nepal:
1443 implications for timing and diachroneity of initial Himalayan orogenesis. *Earth and*
1444 *Planetary Science Letters*, 227, 313–330.
- 1445 DeCelles, P.G., Gehrels, G.E., Quade, J., LaReau, B., & Spurlin, M. (2000). Tectonic
1446 implications of U–PL zircon ages of the Himalayan orogenic belt in Nepal. *Science* 288,
1447 497–499. DeCelles, P.G., Robinson, D.M., Quade, J., Ojha, T.P., Garziane, C.N.,
1448 Copeland, P., Upreti, B.N., 2001. Stratigraphy, structure, and tectonic evolution of the
1449 Himalayan fold-thrust belt in western Nepal. *Tectonics*, 20, 487–509.
- 1450 Denolle, M.A., Fan, W., & Shearer, M. (2015). Dynamics of the 2015 M7.8 Nepal earthquake.
1451 *Geophysical Research Letters*, 42, 7467–7475. <https://doi.org/10.1002/2015GL065336>
- 1452 Dewey, J.F., & Bird, J.M. (1970). Mountain belts and new global tectonics. *Journal of*
1453 *Geophysical Research*, 75, 2625–2685.
- 1454 Dey, S., Dasgupta, P., Das, K., & Matin, A. (2020). Neoproterozoic Blaini Formation of Lesser
1455 Himalaya, India: Fiction and Fact. *Geological Society of America Bulletin*, 132 (11–12),
1456 2267–2281. <https://doi.org/10.1130/B35483.1>
- 1457 Dhamodharan, S., Rawat, G., Kumar, S., & Bagri, D.S. (2020). Sedimentary thickness of the
1458 northern Indo-Gangetic plain inferred from magnetotelluric studies. *Journal of Earth*
1459 *System Sciences*, 129, 156–168. <https://doi.org/10.1007/s12040-020-01422-z>
- 1460 Ding, L., Kapp, P., & Wan, X.Q. (2005). Paleocene–Eocene record of ophiolite obduction and
1461 initial India–Asia collision, south central Tibet. *Tectonics* 24, TC3001.
1462 <https://doi.org/10.1029/2004TC001729>
- 1463 DiPietro, J.A., & Pogue, K.R. (2004). Tectonostratigraphic subdivisions of the Himalaya: a view
1464 from the west. *Tectonics* 23, TC5001. <https://doi.org/10.1029/2003TC001554>
- 1465 Dubey, A.K. (1997). Simultaneous development of noncylindrical folds, frontal ramps and
1466 transfer faults in a compressional regime—experimental investigation of Himalayan
1467 examples. *Tectonics*, 16, 336–346.
- 1468 Dunkl, I., Antolín, B., Wemmer, K., Rantitsch, G., Kienast, M., Montomoli, C., Ding, L., Carosi,
1469 R., Appel, E., El Bay, R., Xu, Q., & Von Eynatten, H. (2011). Metamorphic evolution of

- 1470 the Tethyan Himalayan flysch in SE Tibet. Geological Society, London, Special
 1471 Publications, 353, 45-69. <https://doi.org/10.1144/SP353.4>
- 1472 Duputel, Z., Vergne, J., Rivera, L., Wittlinger, G., Farra, V., & Hetényi, G. (2016). The 2015
 1473 Gorkha earthquake: A large event illuminating the Main Himalayan Thrust fault.
 1474 Geophysical Research Letters, 43, 2517-2525. <https://doi.org/10.1002/2016GL068083>
- 1475 Dyck, B., St-Onge, M., & Searle, M.P., Rayner, N., Waters, D., & Weller, O.M. (2018). Protolith
 1476 lithostratigraphy of the Greater Himalayan Series in Langtang, Nepal: implications for
 1477 the architecture of the northern Indian margin. Geological Society, London, Special
 1478 Publications, 483, 281-304. <https://doi.org/10.1144/SP483.9>
- 1479 Elliott, J., Jolivet, R., González, P.J., Avouac, J-P., Hollingsworth, J., Searle, M., & Stevens, L.
 1480 (2016). Himalayan megathrust geometry and relation to topography revealed by the
 1481 Gorkha earthquake. Nature Geoscience, 9, 174-180. <https://doi.org/10.1038/ngeo2623>
- 1482 England, P.C., & Molnar, P. (1993). The interpretation of inverted metamorphic isograds using
 1483 simple physical calculations. Tectonics, 12, 145-157.
- 1484 England, P.C., Le Fort P., Molnar P., & Pêcher, A. (1992). Heat sources for Tertiary
 1485 metamorphism and anatexis in the Annapurna-Manaslu region, central Nepal. Journal of
 1486 Geophysical Research, 97, 2107-2128.
- 1487 Ernst, W.G. (1973). Blueschist metamorphism and P-T regimes in active subduction zones.
 1488 Tectonophysics, 17, 255.
- 1489 Etzel, T. M., Catlos, E. J., Ataktürk, K., Lovera, O. M., Kelly, E. D., Çemen, I., & Diniz, E.
 1490 (2019). Implications for thrust-related shortening punctuated by extension from P-T paths
 1491 and geochronology of garnet-bearing schists, Southern (Çine) Menderes Massif, SW
 1492 Turkey. Tectonics, 38, 1974– 1998. <https://doi.org/10.1029/2018TC005335>
- 1493 Ferry, J.M., & Spear, F.S. (1978). Experimental calibration of partitioning of Fe and Mg between
 1494 biotite and garnet. Contributions to Mineralogy and Petrology, 66, 113-117.
- 1495 Fuchs, G. (1987). The Geology of southern Zaskar (Ladakh) - Evidence for the autochthony of
 1496 the Tethys Zone of the Himalaya. Jahrbuch der Geologischen Bundesanstalt-A, 130, 465-
 1497 491.
- 1498 Fuchs, G., & Linner, M. (1995). Geological traverse across the western Himalaya- a contribution
 1499 to the geology of eastern Ladakh, Lahul, and Chamba. Jahrbuch der Geologischen
 1500 Bundesanstalt-A., 138, 655-685.
- 1501 Fuchs, G., Widder, R.W., & Tuladhar, R. (1988). Contributions to the Geology of the Annapurna
 1502 Range [Manang Area, Nepal]. Jahrbuch der Geologischen Bundesanstalt-A, 131, 593-
 1503 607.
- 1504 Gaidies, F., de Capitani, C. & Abart, R. (2008). THERIA_G: a software program to numerically
 1505 model prograde garnet growth. Contributions to Mineralogy and Petrology, 155, 657–
 1506 671. <https://doi.org/10.1007/s00410-007-0263-z>
- 1507 Gaidies, F., Petley-Ragan, A., Chakraborty, S., Dasgupta, S., & Jones, P. (2015). Constraining
 1508 the conditions of barrovian metamorphism in Sikkim, India: P-T-t paths of garnet
 1509 crystallization in the Lesser Himalayan Belt. Journal of Metamorphic Geology, 33(1),
 1510 23–44. <https://doi.org/10.1111/jmg.12108>
- 1511 Gansser, A. (1964). The Geology of the Himalayas. Wiley Interscience, New York, 289 pp.
- 1512 Gansser, A. (1981). The geodynamic history of the Himalaya. In Gupta, H.K., and Delany, F.M.,
 1513 (Eds.), Zagros, Hindu Kush, Himalayan Geodynamic Evolution. American Geophysical
 1514 Union, 3, pp. 111-121.

- 1515 Gao, L-E., Zeng, L., Gao, J., Shang, Z., Hou, K., & Wang, Q. (2016). Oligocene crustal anatexis
 1516 in the Tethyan Himalaya, southern Tibet. *Lithos*, 264, 201-209.
 1517 <https://doi.org/10.1016/j.lithos.2016.08.038>
- 1518 Garzanti, E. (1999). Stratigraphy and sedimentary history of the Nepal Tethys Himalaya passive
 1519 margin. *Journal Asian Earth Science*, 17, 805–827.
- 1520 Garzanti, E., & Pagni Frette, M. (1991). Stratigraphic succession of the Thakkhola region
 1521 (central Nepal)- Comparison with the Northwestern Tethys Himalaya. *Rivista Italiana di*
 1522 *Paleontologia e Stratigrafia*, 97(1). <https://doi.org/10.13130/2039-4942/8980>
- 1523 Gehrels, G.E., DeCelles, P.G., Martin, A., Ojha, T.P., Pinhassi, G., & Upreti, B.N. (2003).
 1524 Initiation of the Himalayan Orogen as an early Paleozoic thin-skinned thrust belt.
 1525 *Geological Society of America Today*, 13, 4-9.
- 1526 Gehrels, G.E., P.G. DeCelles, T.P. Ojha, & B. N. Upreti (2006). Geologic and U-Th-Pb
 1527 geochronologic evidence for early Paleozoic tectonism in the Kathmandu thrust sheet,
 1528 central Nepal Himalaya. *Geological Society of America Bulletin*, 118, 185–198.
- 1529 Gervais, F., & Brown, R.L. (2011). Testing modes of exhumation in collisional orogens:
 1530 Synconvergent channel flow in the southeastern Canadian Cordillera. *Lithosphere*, 3, 55–
 1531 75. <https://doi.org/10.1130/L98.1>
- 1532 Ghosh, S., Sanyal, P., Sangode, S.J., & Nanda, A.C. (2018). Substrate control of C4 plant
 1533 abundance in the Himalayan foreland: A study based on inter-basinal records from Plio-
 1534 Pleistocene Siwalik Group sediments. *Palaeogeography, Palaeoclimatology,*
 1535 *Palaeoecology*, 511, 341–351.
- 1536 Gibson, R., Godin, L., Kellett, D.A., Cottle, J.M., & Archibald, D. (2016). Diachronous
 1537 deformation along the base of the Himalayan metamorphic core, west-central Nepal.
 1538 *GSA Bulletin*, 128 (5-6), 860–878. <https://doi-org/10.1130/B31328.1>
- 1539 Gnos, E., Immenhauser, A., Peters, Tj. (1997). Late Cretaceous/early Tertiary convergence
 1540 between the Indian and Arabian plates recorded in ophiolites and related sediments.
 1541 *Tectonophysics*, 271(1–2), 1-19. [https://doi.org/10.1016/S0040-1951\(96\)00249-1](https://doi.org/10.1016/S0040-1951(96)00249-1)
- 1542 Godin, L., Brown, R.L., & Hanmer, S. (1999b). High strain zone in the hanging wall of the
 1543 Annapurna detachment, central Nepal Himalaya. In Macfarlane, A., Sorkhabi, R.B., &
 1544 Quade, J., (Eds.), *Himalaya and Tibet: Mountain roots to mountain tops*. Geological
 1545 Society of America Special Paper, 328, pp. 199-210.
- 1546 Godin, L., Brown, R.L., Hanmer, S., & Parrish, R.R. (1999a). Back folds in the Himalayan
 1547 orogen: an alternative interpretation. *Geology*, 27, 151-154.
- 1548 Goscombe, B., & Hand, M. (2000). Contrasting P-T paths in the eastern Himalaya, Nepal:
 1549 Inverted isograds in a paired metamorphic mountain belt. *Journal of Petrology*, 41(12),
 1550 1673–1719. <https://doi.org/10.1093/petrology/41.12.1673>
- 1551 Goscombe, B., Gray, D., & Hand, M. (2006). Crustal architecture of the Himalayan metamorphic
 1552 front in eastern Nepal. *Gondwana Research*, 10(3–4), 232-255.
 1553 <https://doi.org/10.1016/j.gr.2006.05.003>.
- 1554 Goswami, P.K., & Deopa, T. (2017). Petrotectonic setting of the provenance of Lower Siwalik
 1555 sandstones of the Himalayan foreland basin, southeastern Kumaun Himalaya, India.
 1556 *Island Arc*, 27:e12242. <https://doi.org/10.1111/iar.12242>
- 1557 Goswami-Banerjee, S., Bhowmik, S. K., Dasgupta, S., & Pant, N. C. (2014). Burial of thermally
 1558 perturbed Lesser Himalayan mid-crust: Evidence from petrochemistry and P-T estimation
 1559 of the western Arunachal Himalaya, India. *Lithos*, 208-209, 298–311.
 1560 <https://doi.org/10.1016/j.lithos.2014.09.015>

- 1561 Graham, C.M., & England, P.C. (1976). Thermal regimes and regional metamorphism in the
1562 vicinity of overthrust faults: an example of shear heating and inverted metamorphic
1563 zonation from southern California. *Earth and Planetary Science Letters*, 31, 142-152.
- 1564 Graham, C.M., & Powell, R. (1984). A garnet-hornblende geothermometer; calibration, testing,
1565 and application to the Pelona Schist, Southern California. *Journal of Metamorphic
1566 Geology*, 2, 13-31.
- 1567 Grasemann B., & Vannay J-C. (1999). Flow controlled inverted metamorphism in shear zones.
1568 *Journal of Structural Geology*, 21, 743-750.
- 1569 Groppo, C., Rolfo, F., & Lombardo, B. (2009). P-T evolution across the Main Central Thrust
1570 Zone (eastern Nepal): Hidden discontinuities revealed by petrology. *Journal of Petrology*,
1571 50(6), 1149–1180. <https://doi.org/10.1093/petrology/egp036>
- 1572 Groppo, C., Rubatto, D., Rolfo, F., & Lombardo, B. (2010). Early Oligocene partial melting in
1573 the Main Central Thrust Zone (Arun valley, eastern Nepal Himalaya). *Lithos*, 118(3-4),
1574 287–301. <https://doi.org/10.1016/j.lithos.2010.05.003>
- 1575 Grujic, D., Casey, M., Davidson, C., Hollister, L.D., Kündig, R., Pavlis, T., & Schmid, S. (1996).
1576 Ductile extrusion of the Higher Himalayan Crystalline in Bhutan: evidence from quartz
1577 microfabrics. *Tectonophysics*, 260(1–3), 21-43. [https://doi.org/10.1016/0040-
1578 1951\(96\)00074-1](https://doi.org/10.1016/0040-1951(96)00074-1)
- 1579 Guillot, S. (1999). An overview of the metamorphic evolution in Central Nepal. *Journal of Asian
1580 Earth Sciences*, 17, 713-725.
- 1581 Guillot, S., Cosca, M., Allemand, P., & LeFort, P. (1999). Contrasting metamorphic and
1582 geochronologic evolution along the Himalayan belt. In: Macfarlane, A., Sorkhabi, R.B.,
1583 Quade, J. (Eds.), *Himalaya and Tibet: Mountain Roots to Mountain Tops*. Geological
1584 Society of America Special Papers, vol. 328, pp. 117– 128.
- 1585 Guillot, S., LeFort, P., Pêcher, A., Barman, M.R., & Aprahmaian, J. (1995). Contact-
1586 metamorphism and depth of emplacement of the Manaslu granite (Central Nepal)—
1587 implications for Himalayan orogenesis. *Tectonophysics*, 241, 99– 119.
- 1588 Guillot, S., Mahéo, G., de Sigoyer, J., Hattori, K.H., & Pêcher, A. (2008). Tethyan and Indian
1589 subduction viewed from the Himalayan high- to ultrahigh-pressure metamorphic rocks.
1590 *Tectonophysics*, 451, 225-241.
- 1591 Gupta, D.K., Bhowmick, D., & Roy, N.S. (2015). Himalayan hazard study on the basis of stress
1592 and strain state of 1991 Uttarkashi earthquake using Coulomb stress transfer model.
1593 *Geomatics, Natural Hazards and Risk*, 6, 131-148.
1594 <https://doi.org/10.1080/19475705.2013.820797>
- 1595 Guynn, J.H., Kapp, P., Pullen, A., Gehrels, G., Heizler, M. & Ding, L. (2006). Tibetan basement
1596 rocks near Amdo reveal “missing” Mesozoic tectonism along the Bangong suture, central
1597 Tibet. *Geology*, 34, 505-508.
- 1598 Harris, N., Inger, S., & Massey, J. (1993). The role of fluids in the formation of High Himalayan
1599 leucogranites. In Trearlor, P.J., & Searle, M.P., (Eds.), *Himalayan Tectonics*. Geological
1600 Society Special Publication, 74, pp. 391-400.
- 1601 Harris, N., & Massey, J. (1994). Decompression and anatexis of Himalayan metapelites.
1602 *Tectonics*, 13(6), 1537– 1546. <https://doi.org/10.1029/94TC01611>
- 1603 Harrison, T.M., Grove M., Lovera O.M., & Catlos E.J. (1998). A model for the origin on
1604 Himalayan anatexis and inverted metamorphism. *Journal of Geophysical Research*, 103,
1605 27017-27032.

- 1606 Harrison, T.M., Grove, M., Lovera, O.M., Catlos, E.J., & D'Andrea, J. (1999). The origin of
1607 Himalayan anatexis and inverted metamorphism: Models and constraints. *Journal of*
1608 *Asian Earth Sciences*, 17, 755-772.
- 1609 Harrison, T.M., McKeegan, K.D., & LeFort, P. (1995). Detection of inherited monazite in the
1610 Manaslu leucogranite by $^{208}\text{Pb}/^{232}\text{Th}$ ion microprobe dating: Crystallization age and
1611 tectonic implications. *Earth and Planetary Science Letters*, 133(3–4), 271-282.
1612 [https://doi.org/10.1016/0012-821X\(95\)00091-P](https://doi.org/10.1016/0012-821X(95)00091-P).
- 1613 Hazarika, D., Wadhawan M., Paul, A., Kumar, N., & Borah, K. (2017). Geometry of the Main
1614 Himalayan Thrust and Moho beneath Satluj valley, northwest Himalaya: Constraints
1615 from receiver function analysis. *Journal of Geophysical Research*, 122, 2929-2945.
1616 <https://doi.org/10.1002/2016JB013783>
- 1617 He, P., Lei, J., Yuan, X., Xu, X., Xu, Q., Liu, Z., Mi, Q., & Zhou, L. (2018). Lateral Moho
1618 variations and the geometry of the Main Himalayan Thrust beneath the Nepal Himalayan
1619 orogen revealed by teleseismic receiver functions. *Geophysical Journal International*,
1620 214, 1004-1017. <https://doi.org/10.1093/gji/ggy192>
- 1621 Hébert, R., Bezard, R., Guilmette, C., Dostal, J., Wang, C.S. & Liu, Z.F. (2012). The Indus–
1622 Yarlung Zangbo ophiolites from Nanga Parbat to Namche Barwa syntaxes, southern
1623 Tibet: First synthesis of petrology, geochemistry, and geochronology with incidences on
1624 geodynamic reconstructions of Neo-Tethys. *Gondwana Research*, 22, 337–397.
- 1625 Heim, A.A., & Gansser, A. (1939) *The Throne of the Gods; An Account of the First Swiss*
1626 *Expedition to the Himalayas*. New York: The Macmillan Company, 262 pp.
1627 ASIN:B000856X12
- 1628 Henry, P., Le Pichon, X., & Goffe, B. (1997). Kinematic, thermal and petrological model of the
1629 Himalayas: Constraints related to metamorphism within the underthrust Indian crust and
1630 topographic elevation. *Tectonophysics*, 273, 31-56.
- 1631 Herman, F., Copeland, P., Avouac, J. , Bollinger, L., Mahéo, G., Le Fort, P., et al. (2010).
1632 Exhumation, crustal deformation, and thermal structure of the Nepal Himalaya derived
1633 from the inversion of thermochronological and thermobarometric data and modeling of
1634 the topography. *Journal of Geophysical Research*, 115, B06407.
1635 <https://doi.org/10.1029/2008JB006126>
- 1636 Hirschmiller, J., Grujic, D., Bookhagen, B., Coutand, I., Huyghe, P., Mugnier, J-L., & Ojha, T.
1637 (2014). What controls the growth of the Himalayan foreland fold-and-thrust belt?
1638 *Geology*, 42 (3), 247–250. <https://doi.org/10.1130/G35057.1>
- 1639 Hodges, K.V. (2000). Tectonics of the Himalaya and southern Tibet from two perspectives.
1640 *Geological Society of America Bulletin*, 112, 324–350.
- 1641 Hodges, K.V., & Silverberg, D.S. (1988). Thermal evolution of the Greater Himalaya, Garhwal,
1642 India. *Tectonics*, 7, 583-600.
- 1643 Hodges, K.V., Burchfiel, B.C., Royden, L.H., Chen, Z., & Liu, Y. (1993). The metamorphic
1644 signature of contemporaneous extension and shortening in the central Himalayan orogen:
1645 data from the Nyalam transect, southern Tibet. *Journal of Metamorphic Geology*, 11,
1646 721-737.
- 1647 Hodges, K.V., Hames, W.E., Olszewski, W.J., Burchfiel, B.C., Royden, L.H., & Chen, Z.
1648 (1994). Thermobarometric and $^{40}\text{Ar}/^{39}\text{Ar}$ geochronologic constraints on Eohimalayan
1649 metamorphism in the Dinggy area, southern Tibet. *Contributions to Mineralogy*
1650 *Petrology*, 117, 151– 163.

- 1651 Hodges, K.V., Le Fort, P., & Pêcher, A. (1988). Possible thermal buffering by crustal anatexis in
1652 collisional orogens: thermobarometric evidence from the Nepalese Himalaya. *Geology*,
1653 16, 707-710.
- 1654 Hodges, K.V., Parrish, R.R., & Searle, M.P. (1996). Tectonic evolution of the central Annapurna
1655 Range, Nepalese Himalayas. *Tectonics*, 15, 1264-1291.
- 1656 Hoisch, T.D. (1990). Empirical calibration of six geobarometers for the mineral assemblage
1657 quartz + muscovite + biotite + plagioclase + garnet. *Contributions to Mineralogy and*
1658 *Petrology*, 104, 225-234.
- 1659 Holland, T. J. B., Baker, J. M., & Powell, R. (1998). Mixing properties and activity—
1660 Composition relationships of chlorites in the system MgO-FeO-Al₂O₃-SiO₂-H₂O.
1661 *European Journal of Mineralogy*, 10(3), 395–406. <https://doi.org/10.1127/ejm/10/3/0395>
- 1662 Hopkinson, T.N., Harris, N.B.W., Warren, C.J., Spencer, C.J., Roberts, N.M.W., Horstwood,
1663 M.S.A., Parrish, R.R., & EIMF (2017). The identification and significance of pure
1664 sediment-derived granites. *Earth and Planetary Science Letters*, 467, 57-63.
1665 <https://doi.org/10.1016/j.epsl.2017.03.018>
- 1666 Hu, X., Garzanti, E., Wang, J., Huang, W., An, Q. & Webb, A. 2016. The timing of India–Asia
1667 collision onset – Facts, theories, controversies. *Earth-Science Reviews*, 160, 264–299.
- 1668 Hu, X., Jansa, L., Chen, L., Griffin, W.L., O'Reilly, S.Y. & Wang, J. (2010). Provenance of
1669 Lower Cretaceous Wölong volcanoclastics in the Tibetan Tethyan Himalaya: Implications
1670 for the final breakup of Eastern Gondwana. *Sedimentary Geology*, 223, 193–205.
1671 <https://doi.org/10.1016/j.sedgeo.2009.11.008>
- 1672 Hubbard, M.S. (1989). Thermobarometric constraints on the thermal history of the Main Central
1673 Thrust Zone and Tibet Slab, eastern Nepal Himalaya. *Journal of Metamorphic Geology*,
1674 7, 19-30.
- 1675 Hubbard, M.S. (1996). Ductile shear as a cause of inverted metamorphism: example from the
1676 Nepal Himalaya. *Journal of Geology*, 104, 493-499.
- 1677 Hughes, (2016). Harrison, T.M., Grove M., & Lovera O.M. (1997). New insights into the origin
1678 of two contrasting Himalayan granite belts. *Geology*, 25, 899-902.
- 1679 Hughes, N.C., Myrow, P.M., Peng, S., Banerjee, D.M. (2018). The Parahio Formation of the
1680 Tethyan Himalaya: The type section, thickness, lithostratigraphy and biostratigraphy of
1681 the best characterised Cambrian succession in the Indian subcontinent. *Journal of the*
1682 *Palaeontological Society of India*, 63(1), 1-18.
- 1683 Hughes, N.C., Peng, S., Bhargava, O.N., Ahulwalia, A.D., Walia, S., Myrow, P.M., & Parcha,
1684 S.K. (2005). The Cambrian biostratigraphy of the Tal Group, Lesser Himalaya, India, and
1685 early Tsanglangpuan (late early Cambrian) trilobites from the Nigali Dhar Syncline.
1686 *Geological Magazine*, 142, 57–80.
- 1687 Iaccarino, S., Montomoli, C., Carosi, R., Massonne, H.-J., & Visonà, D. (2017). Geology and
1688 tectono-metamorphic evolution of the Himalayan metamorphic core: Insights from the
1689 Mugu Karnali transect, western Nepal (central Himalaya). *Journal of Metamorphic*
1690 *Geology*, 35(3), 301–325. <https://doi.org/10.1111/jmg.12233>
- 1691 Iaccarino, S., Montomoli, C., Montemagni, C., Massonne, H.-J., Langone, A., Jain, A.K., Visonà,
1692 D., & Carosi, R. (2020). The Main Central Thrust zone along the Alaknanda and Dhaulti
1693 Ganga valleys (Garhwal Himalaya, NW India): Insights into an inverted metamorphic
1694 sequence. *Lithos*, 372–373. <https://doi.org/10.1016/j.lithos.2020.105669>
- 1695 Imayama, T., Takeshita, T., & Arita, K. (2010). Metamorphic P-T profile and P-T path
1696 discontinuity across the far-eastern Nepal Himalaya: Investigation of channel flow

- 1697 models. *Journal of Metamorphic Geology*, 28, 527-549. <https://doi.org/10.1111/j.1525-1314.2010.00879.x>
- 1698
- 1699 Inger, S. & Harris, N.B.W. (1992). Tectonothermal evolution of the High Himalaya Crystalline
1700 sequence, Langtang Valley, northern Nepal. *Journal of Metamorphic Geology*, 10, 439-
1701 452
- 1702 Jadoul, F., Berra, F., & Garzanti, E. (1998). The Tethys Himalayan passive margin from Late
1703 Triassic to Early Cretaceous (South Tibet): *Journal of Asian Earth Sciences*, 16, 173–194.
1704 [https://doi.org/10.1016/S0743-9547\(98\)00013-0](https://doi.org/10.1016/S0743-9547(98)00013-0)
- 1705 Jain, A.K., & Chander, R. (1995). Geodynamic models for Uttarkashi earthquake of October 20,
1706 1991. *Memoirs of the Geological Society of India*, Bangalore, 225-233.
- 1707 Jamieson, R.A., & Beaumont, C. (2013). On the origin of orogens. *Geological Society of
1708 America Bulletin*, 11-12, 1671-1702.
- 1709 Jamieson, R.A., Beaumont, C., Hamilton, J., & Fullsack, P. (1996). Tectonic assembly of
1710 inverted metamorphic sequences. *Geology*, 24, 839–842.
- 1711 Jamieson, R.A., Beaumont, C., Medvedev, S., Nguyen, M.H. (2004). Crustal channel flows: 2.
1712 Numerical models with implications for metamorphism in the Himalayan–Tibetan
1713 orogen. *Journal of Geophysical Research*, 109. <https://doi.org/10.1029/2003JB002811>
- 1714 Jamieson, R.A., Beaumont, C., Nguyen, M.H., & Grujic, D. (2006). Provenance of the Greater
1715 Himalayan Sequence and associated rocks: predictions of channel flow models.
1716 *Geological Society, London, Special Publications*, 268, 165-182, 1 January 2006.
1717 <https://doi.org/10.1144/GSL.SP.2006.268.01.07>
- 1718 Jharendra, K.C., & Paudyal, K.R. (2019). Characteristics and field relation of Ulleri Augen
1719 Gneiss to country rocks in the Lesser Himalaya: A case study from Syaprubesi-
1720 Chhyamthali area, central Nepal. *Journal of Nepal Geological Society*, 58, 89-96.
1721 <https://doi.org/10.3126/jngs.v58i0.24577>
- 1722 Kaneko, Y. (1995). Thermal structure in the Annapurna region, central Nepal Himalaya:
1723 implication for the inverted metamorphism. *J. Mineral. Petrol. Econ. Geol.*, 90, 143-154.
- 1724 Kaneoka, I. & Kono, M. (1981). $^{40}\text{Ar}/^{39}\text{Ar}$ dating of Himalayan rocks from the Mount Everest
1725 Region. *Journal of Geophysics*, 49, 207-211.
- 1726 Kapp, P., DeCelles, P.G., Gehrels, G.E., Heizler, M. & Ding, L. 2007. Geological records of the
1727 Lhasa–Qiangtang and Indo-Asian collisions in the Nima area of central Tibet. *Geological
1728 Society of America Bulletin*, 119, 917–932.
- 1729 Kapp, P., Murphy, M.A., Yin, A., Harrison, T.M., Ding, L. & Guo, J.R. 2003. Mesozoic and
1730 Cenozoic tectonic evolution of the Shiquanhe area of western Tibet. *Tectonics*, 22.
1731 <https://doi.org/10.1029/2001TC001332>
- 1732 Kawakami, T., Sakai, H., & Sato, K. (2019). Syn-metamorphic B-bearing fluid infiltrations
1733 deduced from tourmaline in the Main Central Thrust zone, Eastern Nepal Himalayas.
1734 *Lithos*, 348–349, 105175. <https://doi.org/10.1016/j.lithos.2019.105175>
- 1735 Kayal, J.R. (1996). Precursor seismicity, foreshocks and aftershocks of the Uttarkashi earthquake
1736 of October 20, 1991 at Garhwal Himalaya. *Tectonophysics*, 263, 339-345.
- 1737 Kellett, S.A., Cottle, J.M., & Larson, K.P. (2018). The South Tibetan Detachment System:
1738 history, advances, definition and future directions. *Geological Society, London, Special
1739 Publications*, 483, 377-400. <https://doi.org/10.1144/SP483.2>
- 1740 Kelly, E. D., Hoisch, T. D., Wells, M. L., Vervoort, J. D. & Beyene, M. A. (2015). An Early
1741 Cretaceous garnet pressure–temperature path recording synconvergent burial and

- 1742 exhumation from the hinterland of the Sevier orogenic belt, Albion Mountains, Idaho.
1743 *Contributions to Mineralogy and Petrology* 170, 1–22.
- 1744 Khan, M.A., Bera, M., Spicer, R.A., Spicer, T.E.V., & Bera, S. (2019). Palaeoclimatic estimates
1745 for a latest Miocene-Pliocene flora from the Siwalik Group of Bhutan: Evidence for the
1746 development of the South Asian Monsoon in the eastern Himalaya, *Palaeogeography,*
1747 *Palaeoclimatology, Palaeoecology*, 514, 326–335.
1748 <https://doi.org/10.1016/j.palaeo.2018.10.019>
- 1749 Khanal, S., Robinson, D.M., Mandal, S., & Simkhada, P. (2014). Structural, geochronological
1750 and geochemical evidence for two distinct thrust sheets in the ‘Main Central thrust zone’,
1751 the Main Central thrust and Ramgarh–Munsiari thrust: implications for upper crustal
1752 shortening in central Nepal Geological Society, London, Special Publications, 412, 221–
1753 245. <https://doi.org/10.1144/SP412.2>
- 1754 Khattri, K.N. and Tyagi, A.K. (1983). Seismicity patterns in the Himalayan plate boundary and
1755 identification of areas of high seismic potential. *Tectonophysics*, 96, 281–297.
- 1756 Kidder, S.B., Herman, F., Saleeby, J., Avouac, J-P., Ducea, M.N., & Chapman, A. (2013). Shear
1757 heating not a cause of inverted metamorphism. *Geology*, 41, 899–902.
1758 <https://doi.org/10.1130/G34289.1>
- 1759 Klootwijk, C.T., Gee, J.S., Peirce, J.W., Smith, G.M., & McFadden, P.L. (1992). An early India-
1760 Asia contact: Paleomagnetic constraints from Ninetyeast Ridge, ODP Leg 121. *Geology*,
1761 20(5), 395–398. [https://doi.org/10.1130/0091-7613\(1992\)020<0395:AEIACP>2.3.CO;2](https://doi.org/10.1130/0091-7613(1992)020<0395:AEIACP>2.3.CO;2)
- 1762 Kohn, M. J., M. Wieland, C. D. Parkinson, & B. N. Upreti (2004). Miocene faulting at plate
1763 tectonic velocity in the Himalaya of central Nepal, *Earth and Planetary Science Letters*,
1764 228, 299–310.
- 1765 Kohn, M. J., S. K. Paul, & S. L. Corrie (2010). The lower Lesser Himalayan sequence: A
1766 Paleoproterozoic arc on the northern margin of the Indian plate, *Geological Society of*
1767 *America Bulletin*, 122, 323–335.
- 1768 Kohn, M.J. (1993). Uncertainties in differential thermodynamic (Gibbs' method) P-T paths.
1769 *Contributions to Mineralogy and Petrology*, 113, 24–39.
1770 <https://doi.org/10.1007/BF00320829>
- 1771 Kohn, M.J. (2008). P-T-t data from central Nepal support critical taper and repudiate large-scale
1772 channel flow of the Greater Himalayan Sequence. *Geological Society of America*
1773 *Bulletin*, 120, 259–273. <https://doi.org/10.1130/B26252.1>
- 1774 Kohn, M.J. (2014). Himalayan metamorphism and its tectonic implications. *Annual Review of*
1775 *Earth and Planetary Sciences*, 42(1), 381–419.
- 1776 Kohn, M.J. (2016). Metamorphic chronology—a tool for all ages: Past achievements and future
1777 prospects. *American Mineralogist*, 101, 25–42. <https://doi.org/10.2138/am-2016-5146>
- 1778 Kohn, M.J., & Spear, F. (2000). Retrograde net transfer reaction insurance for pressure-
1779 temperature estimates. *Geology*, 28, 1127–1130. [https://doi.org/10.1130/0091-7613\(2000\)28<1127:RNTRIF>2.0.CO;2](https://doi.org/10.1130/0091-7613(2000)28<1127:RNTRIF>2.0.CO;2)
- 1781 Kohn, M.J., & Spear, F.S. (1990). Two new barometers for garnet amphibolites with applications
1782 to southeastern Vermont: *American Mineralogist*, 75, p. 89–96.
- 1783 Kohn, M.J., & Spear, F.S. (1991). Error propagation for barometers: 2. Application to rocks.
1784 *American Mineralogist*, 76 (1-2), 138–147.
- 1785 Kohn, M.J., Catlos, E.J., Ryerson, F.J., & Harrison, T.M. (2001). Pressure-temperature-time path
1786 discontinuity in the Main Central thrust zone, central Nepal. *Geology*, 29 (7), 571–574.
1787 [https://doi.org/10.1130/0091-7613\(2001\)029<0571:PTTPDI>2.0.CO;2](https://doi.org/10.1130/0091-7613(2001)029<0571:PTTPDI>2.0.CO;2)

- 1788 Kohn, M.J., Catlos, E.J., Ryerson, F.J., & Harrison, T.M. (2001). Pressure–temperature–time
1789 path discontinuity in the Main Central thrust zone, central Nepal. *Geology*, 29, 571–574.
- 1790 Lanari, P. & Duesterhoeft, E. (2019). Modeling metamorphic rocks using equilibrium
1791 thermodynamics and internally consistent databases: Past achievements, problems and
1792 perspectives. *Journal of Petrology*, 60, 19–56. <https://doi.org/10.1093/petrology/egy105>
- 1793 Lanari, P., & Engi, M. (2017). Local bulk composition effects on metamorphic mineral
1794 assemblages. *Reviews in Mineralogy and Geochemistry*, 83, 55– 102.
1795 <https://doi.org/10.2138/rmg.2017.83.3>
- 1796 Larson, K.P., Godin, L., & Price, R.A. (2010). Relationships between displacement and
1797 distortion in orogens: Linking the Himalayan foreland and hinterland in central Nepal.
1798 *Geological Society of America Bulletin*, 122 (7-8), 1116–1134.
1799 <https://doi.org/10.1130/B30073.1>
- 1800 Larson K.P., Kellet, D.A., Cottle, J.M., Camacho, A., & Brubacher, A.D. (2019). Mid-Miocene
1801 initiation of E-W extension and recoupling of the Himalayan Orogen. *Terra Nova* 12443,
1802 1–8.
- 1803 Larson, K., Gervais, F., & Kellett, D. A. (2013). A P-T-t-D discontinuity in east-central Nepal:
1804 Implications for the evolution of the Himalayan mid-crust. *Lithos*, 179, 275-292.
1805 <https://doi.org/10.1016/j.lithos.2013.08.012>
- 1806 Larson, K.P., Ambrose, T.K., Webb, A.A.G., Cottle, J.M., & Shrestha, S. (2015). Reconciling
1807 Himalayan midcrustal discontinuities: The Main Central thrust system. *Earth and
1808 Planetary Science Letters*, 429, 139-146. <https://doi.org/10.1016/j.epsl.2015.07.070>
- 1809 Laskowski, A.K., Kapp, P., Vervoort, J.D., & Ding, L. (2016). High-pressure Tethyan Himalaya
1810 rocks along the India-Asia suture zone in southern Tibet. *Lithosphere*, 8 (5), 574–582.
1811 <https://doi.org/10.1130/L544.1>
- 1812 Lawver, L.A., Norton, I.O., Dalziel, I.W.D., Davis, J.K. & Gahagan, L.M. (2018). The PLATES
1813 2017 Atlas of Plate Reconstructions (550 Ma to Present Day). PLATES Progress Report,
1814 390-0318.
- 1815 Le Fort, P. (1975). Himalaya, the collided range, Present knowledge of the continental arc.
1816 *American Journal of Science*, 275A, 1-44.
- 1817 Le Fort, P. (1996). Evolution of the Himalaya. In Yin, A., and Harrison, T.M., (Eds.), *The
1818 Tectonic Evolution of Asia*. Cambridge University Press, pp. 95-109.
- 1819 Lee, J., Hacker, B., & Wang, Y. (2004). Evolution of North Himalayan gneiss domes: structural
1820 and metamorphic studies in Mabja Dome, southern Tibet. *Journal of Structural Geology*,
1821 26, 2297–316.
- 1822 LeFort, P., & Rai, S.M. (1999). Pre-Tertiary felsic magmatism of the Nepal Himalaya: recycling
1823 of continental crust. *Journal of Asian Earth Sciences*, 17, 607– 628.
- 1824 Lihter, I., Larson, K.P., Shrestha, S., Cottle, J.M., & Brubacher, A.D. (2020). Contact
1825 metamorphism of the Tethyan Sedimentary Sequence, Upper Mustang region, west-
1826 central Nepal. *Geological Magazine*, 157(11), 1917–1932.
1827 <https://doi.org/10.1017/S0016756820000229>
- 1828 Liu, G., & Einsele, G. (1994). Sedimentary history of the Tethyan basin in the Tibetan
1829 Himalayas. *Geologische Rundschau*, 82, 32– 61.
- 1830 Liu, J-H., Xie, C-M., Li, C., Wang, M., Wu, H., Li, X-K., Liu, Y-M., Zhang, T-Y. (2018). Early
1831 Carboniferous adakite-like and I-type granites in central Qiangtang, northern Tibet:
1832 Implications for intra-oceanic subduction and back-arc basin formation within the Paleo-
1833 Tethys Ocean. *Lithos*, 296–299, 265-280. <https://doi.org/10.1016/j.lithos.2017.11.005>

- 1834 Liu, Z.C., Wu, F.Y., Ding, L., Liu, X.C., Wang, J.G., & Ji, W.Q. (2016). Highly fractionated
 1835 Late Eocene (~ 35 Ma). leucogranites in the Xiaru Dome, Tethyan Himalaya, South
 1836 Tibet. *Lithos*, 240-243, 337-354.
- 1837 Lombardo B., Pertusati, P., & Borghi, S. (1993). Geology and tectonomagmatic evolution of the
 1838 eastern Himalaya along the Chomolungma-Makalu transect. In Treloar, P.J., & Searle,
 1839 M.P., (Eds.), *Himalayan Tectonics*. Geological Society Special Publication, 74, pp. 341-
 1840 355.
- 1841 Lombardo, B., Rolfo, F., 2000. Two contrasting eclogite types in the Himalayas: implications for
 1842 the Himalayan orogeny. *Journal of Geodynamics*, 30, 37-60.
- 1843 Long, S., & McQuarrie, N. (2010). Placing limits on channel flow: Insights from the Bhutan
 1844 Himalaya. *Earth and Planetary Science Letters*, 290, 475-390.
- 1845 Long, S., McQuarrie, N., Tobgay, T., & Grujic, D. (2011). Geometry and crustal shortening of
 1846 the Himalayan fold-thrust belt, eastern and central Bhutan. *Geological Society of
 1847 America Bulletin*, 123 (7-8), 1427–1447. <https://doi.org/10.1130/B30203.1>
- 1848 Long, S.P., Gordon, S.M., & Soignard, E., 2017, Distributed north-vergent shear and flattening
 1849 through Greater and Tethyan Himalayan rocks: Insights from metamorphic and strain
 1850 data from the Dang Chu region, central Bhutan. *Lithosphere*, 9, 774–795.
 1851 <https://doi.org/10.1130/L655.1>
- 1852 Long, S.P., Mullady, C.L., Starnes, J.K., Gordon, S.M., Larson, K.P., Pianowski, L.S., Miller,
 1853 R.B., & Soignard, E. (2019). A structural model for the South Tibetan detachment system
 1854 in northwestern Bhutan from integration of temperature, fabric, strain, and kinematic
 1855 data. *Lithosphere*, 11 (4), 465–487. <https://doi.org/10.1130/L1049.1>
- 1856 Macfarlane, A.M. (1995). An evaluation of the inverted metamorphic gradient at Langtang
 1857 National Park, central Nepal Himalaya. *Journal of Metamorphic Geology*, 13, 595-612.
- 1858 Mahajan, A.K., Thakur, C., Sharma, M.L., & Chauhan, M. (2010). Probabilistic seismic hazard
 1859 map of NW Himalaya and its adjoining area, India. *Natural Hazards*, 53, 443-457.
 1860 <https://doi.org/10.1007/s11069-009-9439-3>
- 1861 Maiti, G., & Mandal, N. (2021) Early Miocene exhumation of high-pressure rocks in the
 1862 Himalaya: A response to reduced India-Asia convergence velocity. *Frontiers in Earth
 1863 Science*, <https://doi.org/10.3389/feart.2021.632806>.
- 1864 Maiti, G., Mandal, N., & Misra, S. (2020). Insights into the dynamics of an orogenic wedge from
 1865 lubrication theory: Implications for the Himalayan tectonics. *Tectonophysics*, 776,
 1866 228335. <https://doi.org/10.1016/j.tecto.2020.228335>
- 1867 Makovsky, Y., Klempner, S. L., Huang, L., Lu, D., & Project INDEPTH Team (1996).
 1868 Structural elements of the southern Tethyan Himalaya crust from wide-angle seismic
 1869 data, *Tectonics*, 15(5), 997– 1005. <https://doi.org/10.1029/96TC00310>
- 1870 Makovsky, Y., Klempner, S.L., Ratschbacher, L., & Alsdorf, D. (1999). Midcrustal reflector on
 1871 INDEPTH wide-angle profiles: an ophiolitic slab beneath the India–Asia suture in
 1872 southern Tibet? *Tectonics*, 18, 793–808.
- 1873 Mandal, S., Robinson, D.M., Khanal, S., & Das, O. (2015). Redefining the tectonostratigraphic
 1874 and structural architecture of the Almora klippe and the Ramgarh–Munsiari thrust sheet
 1875 in NW India. In: Mukherjee, S., Carosi, R., van der Beek, P.A., Mukherjee, B.K., &
 1876 Robinson, D.M. (Eds.) *Tectonics of the Himalaya*, Geological Society of America
 1877 Special Publications, 412, 247–269.
- 1878 Mandal, S., Robinson, D.M., Kohn, M.J., Khanal, S., Das, O., & Bose S. (2016). Zircon U-Pb
 1879 ages and Hf isotopes of the Askot klippe, Kumaun, northwest India: Implications for

- 1880 Paleoproterozoic tectonics, basin evolution and associated metallogeny of the northern
 1881 Indian cratonic margin, *Tectonics*, 35. <https://doi.org/10.1002/2015TC004064>
- 1882 Manickavasagam, R.M., Jain, A.K., Singh, S., & Asokan, A. (1999). Metamorphic evolution of
 1883 the northwest Himalaya, India: Pressure-temperature data, inverted metamorphism, and
 1884 exhumation in the Kashmir, Himachal, and Garhwal Himalayas. In Macfarlane, A.,
 1885 Sorkhabai, R.B., and Quade, J. (Eds.), *Himalaya and Tibet: Mountain roots to mountain*
 1886 *tops*. Geological Society of America Special Paper, 328, 179-198.
- 1887 Martin, A. J., Ganguly, J., & DeCelles, P.G. (2010). Metamorphism of Greater and Lesser
 1888 Himalayan rocks exposed in the Modi Khola valley, central Nepal. *Contributions to*
 1889 *Mineralogy and Petrology*, 159, 203–223.
- 1890 Martin, A.J. (2017a). A review of Himalayan stratigraphy, magmatism, and structure. *Gondwana*
 1891 *Research*, 49, 42-80. <https://doi.org/10.1016/j.gr.2017.04.031>
- 1892 Martin, A.J. (2017b). A review of definitions of the Himalayan Main Central Thrust.
 1893 *International Journal of Earth Sciences*, 106, 2131-45. [https://doi.org/10.1007/s00531-](https://doi.org/10.1007/s00531-016-1419-8)
 1894 [016-1419-8](https://doi.org/10.1007/s00531-016-1419-8)
- 1895 Martin, A.J. Burgoyne, K.D., Kaufman, A.J., & Gehrels, G.E. (2011). Stratigraphic and tectonic
 1896 implications of field and isotopic constraints on depositional ages of Proterozoic Lesser
 1897 Himalayan rocks in central Nepal. *Precambrian Research*, 185, 1-17.
- 1898 Martin, A.J., DeCelles, P.G., Gehrels, G.E., Patchett, P.J., & Isachsen, C. (2005). Isotopic and
 1899 structural constraints on the location of the Main Central Thrust in the Annapurna Range,
 1900 central Nepal Himalaya. *Geological Society of America Bulletin*, 117(7-8), 926–944.
- 1901 Matin, A., & Mukul, M. (2010). Phases of deformation from cross-cutting structural
 1902 relationships in external thrust sheets: Insights from small-scale structures in the
 1903 Ramgarh thrust sheet, Darjiling Himalaya, West Bengal. *Current Science*, 99(10), 1369-
 1904 1377.
- 1905 Matsuoka, A., Yang, Q., Kobayashi, K., Takei, M., Nagahashi, T., Zeng, Q., & Wang, Y. (2002).
 1906 Jurassic–Cretaceous radiolarian biostratigraphy and sedimentary environments of the
 1907 Ceno-Tethys: records from the Xialu Chert in the Yarlung-Zangbo Suture Zone, southern
 1908 Tibet. *Journal of Asian Earth Sciences*, 20(3), 277-287. [https://doi.org/10.1016/S1367-](https://doi.org/10.1016/S1367-9120(01)00044-X)
 1909 [9120\(01\)00044-X](https://doi.org/10.1016/S1367-9120(01)00044-X)
- 1910 McKenzie, N.R., Hughes, N.C., Myrow, P.M., Xiao, S., & Sharma, M. (2011). Correlation of
 1911 Precambrian–Cambrian sedimentary successions across northern India and the utility of
 1912 isotopic signatures of Himalayan lithotectonic zones. *Earth and Planetary Science Letters*,
 1913 312(3–4), 471-483. <https://doi.org/10.1016/j.epsl.2011.10.027>
- 1914 Medicott, H.B. (1864). On the geologic structure and relations of the southern portion of the
 1915 Himalayan range between the rivers Ganges and Ravee. *Memoirs of the Geological*
 1916 *Survey of India*, 3, 1-206.
- 1917 Meigs, A.J., Burbank, D.W., & Beck, R.A. (1995). Middle-late Miocene [>10 Ma] formation of
 1918 the Main Boundary Thrust in the Western Himalaya. *Geology*, 23, 423-426.
- 1919 Metcalfe, I. (1999). The Tethys; How many? How old? How deep? How wide? In: Ratanasthien,
 1920 B. & Rieb, S. L. (eds) *Proceedings of the International Symposium on Shallow Tethys*, 5,
 1921 1-15.
- 1922 Metcalfe, I. (2009). Late Palaeozoic and Mesozoic tectonic and palaeogeographic evolution of
 1923 SE Asia. *Geological Society of London, Special Publication*, 315, 7-23.
- 1924 Metcalfe, I. 2013. Gondwana dispersion and Asian accretion: Tectonic and palaeogeographic
 1925 evolution of eastern Tethys. *Journal of Asian Earth Sciences*, 66, 1-33.

- 1926 Metcalfe, R.P. (1993). Pressure, temperature and time constraints on metamorphism across the
 1927 Main Central Thrust zone and High Himalaya Slab in the Garhwal Himalaya. In Treloar,
 1928 P.J., and Searle, M.P., (Eds.), *Himalayan Tectonics*. Geological Society Special
 1929 Publication, 74, 485-509.
- 1930 Middlemiss, C.S. (1887). Physical geology of West British Garhwal; with notes on a route
 1931 traverse through Jaunsar Bawar and Tiri-Garhwal. *Records of the Geological Survey of*
 1932 *India*, 20, 26-40.
- 1933 Miller, C., Klotzli, U., Frank, W., Thoni, M., & Grasemann, B. (2000). Proterozoic crustal
 1934 evolution in the NW Himalaya (India) as recorded by circa 1.80 Ga mafic and 1.84 Ga
 1935 granitic magmatism. *Precambrian Research*, 103 (3–4), 191– 206.
- 1936 Molnar, P., & England, P. Late Cenozoic uplift of mountain ranges and global climate change:
 1937 chicken or egg?. *Nature*, 346, 29–34. <https://doi.org/10.1038/346029a0>
- 1938 Molnar, P. & Stock, J.M. (2009). Slowing of India's convergence with Eurasia since 20 Ma and
 1939 its implications for Tibetan mantle dynamics. *Tectonics*, 28.
 1940 <https://doi.org/10.1029/2008TC002271>
- 1941 Montemagni, C, Carosi, R, Fusi, N, Iaccarino, S., Montomoli, C., Villa, I.M., & Zancetta, S.
 1942 (2020) Three-dimensional vorticity and time-constrained evolution of the Main Central
 1943 Thrust zone, Garhwal Himalaya (NW India). *Terra Nova*. 2020; 32: 215– 224.
 1944 <https://doi.org/10.1111/ter.12450>
- 1945 Montemagni, C., Montomoli, C., Iaccarino, S., Carosi, R., Jain, A.K., Massonne, H-K., & Villa,
 1946 I.M. (2018) Dating protracted fault activities: microstructures, microchemistry and
 1947 geochronology of the Vaikrita Thrust, Main Central Thrust zone, Garhwal Himalaya, NW
 1948 India. *Geological Society, London, Special Publications*, 481, 127-146,
 1949 <https://doi.org/10.1144/SP481.3>
- 1950 Montomoli, C., Carosi, R., & Iaccarino, S. (2015). Tectonometamorphic discontinuities in the
 1951 Greater Himalayan Sequence: a local or a regional feature? *Geological Society Special*
 1952 *Publication*, 412, 25-41.
- 1953 Montomoli, C., Carosi, R., Rubatto, D., Visonà, D., & S. Iaccarino (2017). Tectonic activity
 1954 along the inner margin of the South Tibetan Detachment constrained by syntectonic
 1955 leucogranite emplacement in Western Bhutan. *Italian Journal of Geosciences*, 136(1), 5–
 1956 14. <https://doi.org/10.3301/IJG.2015.26>
- 1957 Montomoli, C., Iaccarino, S., Carosi, R., Langone, A., & Visonà, D. (2013).
 1958 Tectonometamorphic discontinuities within the Greater Himalayan Sequence in Western
 1959 Nepal (Central Himalaya): insights on the exhumation of crystalline rocks.
 1960 *Tectonophysics*, 608, 1349-1370.
- 1961 Mosca, P., Groppo, C., & Rolfo, F. (2012). Structural and metamorphic features of the Main
 1962 Central Thrust Zone and its contiguous domains in the eastern Nepalese Himalaya, in
 1963 Zucali, M., Spalla, M.I., & Gosso, G., eds., *Multiscale structures and tectonic trajectories*
 1964 *in active margins*. *Journal of the Virtual Explorer*, 41, 1-34, Clayton, Victoria, Australia:
 1965 Australian Crustal Research Centre, Monash University.
 1966 <https://doi.org/10.3809/jvirtex.2011.00294>
- 1967 Mottram, C.M., Warren, C.J., Regis, D., Roberts, N.M.W., Harris, N.B.W. Argles, T.W., &
 1968 Parrish, R.R. (2014). Developing an inverted Barrovian sequence; insights from monazite
 1969 petrochronology. *Earth and Planetary Science Letters*, 403, 418-431.
 1970 <https://doi.org/10.1016/j.epsl.2014.07.006>

- 1971 Moynihan, D., & Pattison, D.R.M. (2013). An automated method for the calculation of P-T paths
 1972 from garnet zoning, with application to metapelitic schist from the Kootenay Arc, British
 1973 Columbia, Canada. *Journal of Metamorphic Geology*, 31, 525-548.
 1974 <https://doi.org/10.1111/jmg.12032>
- 1975 Mugnier, J.L., Huyghe, P., Chalaron, E., & Mascle, G. (1994). Recent movements along the
 1976 Main Boundary Thrust of the Himalayas: Normal faulting in an over-critical thrust
 1977 wedge? *Tectonophysics*, 238(1-4), 199-215. [https://doi.org/10.1016/0040-](https://doi.org/10.1016/0040-1951(94)90056-6)
 1978 [1951\(94\)90056-6](https://doi.org/10.1016/0040-1951(94)90056-6)
- 1979 Mugnier, J.L., Leturmy, P., Mascle, G., Huyghe, P., Chalaron, E., Vidal, G., Husson, L., &
 1980 Delcaillau, B. (1999). The Siwaliks of western Nepal: I. Geometry and kinematics.
 1981 *Journal of Asian Earth Sciences*, 17(5-6), 629-642. [https://doi.org/10.1016/S1367-](https://doi.org/10.1016/S1367-9120(99)00038-3)
 1982 [9120\(99\)00038-3](https://doi.org/10.1016/S1367-9120(99)00038-3)
- 1983 Mukherjee, S. (2013). Higher Himalaya in the Bhagirathi section (NW Himalaya, India): its
 1984 structures, backthrusts and extrusion mechanism by both channel flow and critical taper
 1985 mechanisms. *International Journal of Earth Sciences (Geol Rundsch)* 102, 1851–1870.
 1986 <https://doi.org/10.1007/s00531-012-0861-5>
- 1987 Mukherjee, S., Koyi, H.A. & Talbot, C.J. (2012). Implications of channel flow analogue models
 1988 for extrusion of the Higher Himalayan Shear Zone with special reference to the out-of-
 1989 sequence thrusting. *International Journal of Earth Sciences (Geol Rundsch)* 101, 253–
 1990 272. <https://doi.org/10.1007/s00531-011-0650-6>
- 1991 Mukhopadhyay, D. K., Chakraborty, S., Trepmann, C., Rubatto, D., Anczkiewicz, R., Gaidies,
 1992 F., et al. (2017). The nature and evolution of the Main Central Thrust: Structural and
 1993 geochronological constraints from the Sikkim Himalaya, NE India. *Lithos*, 282–283,
 1994 447–463. <https://doi.org/10.1016/j.lithos.2017.01.015>
- 1995 Mukul, M. (2000). The geometry and kinematics of the Main Boundary Thrust and related
 1996 neotectonics in the Darjiling Himalayan Fold-and-Thrust belt, West Bengal, India.
 1997 *Journal of Structural Geology*, 22, 1261–1283.
- 1998 Mukul, M., Jaiswal, M., & Singhvi, A.K. (2007). Timing of recent out-of-sequence active
 1999 deformation in the frontal Himalayan wedge: Insights from the Darjiling sub-Himalaya,
 2000 India. *Geology*, 35 (11), 999–1002. [https://doi.org/ https://doi.org/10.1130/G23869A.1](https://doi.org/10.1130/G23869A.1)
- 2001 Myrow, P.M., Hughes, N.C., Derry, L.A., McKenzie, N.R., Jiang, G., Webb, A.A.G., Banerjee,
 2002 D.M., Paulsen, T.S., & Singh, B.P. (2015). Neogene marine isotopic evolution and the
 2003 erosion of Lesser Himalayan strata: implications for Cenozoic tectonic history. *Earth*
 2004 *Planetary Science Letters*, 417, 142–150.
- 2005 Myrow, P.M., Hughes, N.C., Paulsen, T.S., Williams, I.S., Parcha, S.K., Thompson, K.R.,
 2006 Bowring, S.A., Peng, S.C., & Ahluwalia, A.D. (2003). Integrated tectonostratigraphic
 2007 analysis of the Himalaya and implications for its tectonic reconstruction. *Earth and*
 2008 *Planetary Science Letters*, 212, 433-441.
- 2009 Myrow, P.M., Hughes, N.C., Searle, M.P., Fanning, C.M., Peng, S., & Parcha, S.K. (2009).
 2010 Stratigraphic correlation of Cambrian-Ordovician deposits along the Himalaya:
 2011 implications for the age and nature of rocks in the Mt. Everest region. *Geological Society*
 2012 *of America Bulletin*, 120, 323–332.
- 2013 Myrow, P.M., Snell, K., Hughes, N.C., Paulsen, T.S., Heim, N.A., & Parcha, S.K. (2006).
 2014 Cambrian depositional history of the Zaskar Valley region of Indian Himalaya: Tectonic
 2015 implications: *Journal of Sedimentary Research*, 76, 364-381.

- 2016 Nábělek, J., Hetenyi, G., Vergne, J., Sapkota, S., Kafle, B., Jiang, M., Su, H., Chen, J., Huang,
 2017 B.S., & Hi, C.T. (2009). Underplating in the Himalaya-Tibet collision zone revealed by
 2018 the Hi-CLIMB experiment. *Science*, 325, 1371-1374.
 2019 <https://doi.org/10.1126/science.1167719>
- 2020 Najman, Y., Garzanti, E., Pringle, M., Bickle, M., Stix, J., & Khan, I. (2003). Early–middle
 2021 Miocene paleodrainage and tectonics in the Pakistan Himalaya. *Geological Society of
 2022 America Bulletin*, 115, 1265–1277.
- 2023 Najman, Y., Jenks, D. et al. (2017). The Tethyan Himalayan detrital record shows that India–
 2024 Asia terminal collision occurred by 54 Ma in the Western Himalaya. *Earth and Planetary
 2025 Science Letters*, 459, 301–310.
- 2026 Najman, Y., Pringle, M., Godin, L., & Oliver, G. (2001). Dating of the oldest continental
 2027 sediments from the Himalayan foreland basin. *Nature*, 410, 194– 197.
- 2028 Najman, Y., Pringle, M., Godin, L., & Oliver, G. (2002). A reinterpretation of the Balakot
 2029 formation: implications for the tectonics of the NW Himalaya, Pakistan. *Tectonics*, 21
 2030 (Art. No. 1045).
- 2031 Nelson, K.D., Zhao, W., Brown, L.D., & others (1996). Partially molten crust beneath Southern
 2032 Tibet: synthesis of project INDEPTH results. *Science*, 274, 1684-1688.
- 2033 Ni, J. & Barazangi, M. (1984). Seismotectonics of the Himalayan collision zone; geometry of the
 2034 underthrusting Indian Plate beneath the Himalaya. *Journal of Geophysical Research*, 89,
 2035 1147-1163.
- 2036 Oldham, R.D. (1883). The geology of Jaunsar and the Lower Himalayas. *Records of the
 2037 Geological Survey of India*, 16, 193-198.
- 2038 Pandey, M.R., Lavé, J., & Massot, J.P. (1995). Interseismic strain accumulation on the
 2039 Himalayan Crustal Ramp (Nepal). *Geophysical Research Letters*, 22, 751-754.
- 2040 Parrish, R.R., & Hodges, K.V. (1996). Isotopic constraints on the age and provenance of the
 2041 Lesser and Greater Himalaya sequences, Nepalese Himalaya. *Geological Society of
 2042 America Bulletin*, 108, 904-911.
- 2043 Parsons, A. J., Law, R. D., Lloyd, G. E., Phillips, R. J., & Searle, M. P. (2016). Thermo-
 2044 kinematic evolution of the Annapurna-Dhaulagiri Himalaya, central Nepal: The
 2045 Composite Orogenic System. *Geochemistry, Geophysics, Geosystems*, 17, 1511–1539.
 2046 <https://doi.org/10.1002/2015GC006184>
- 2047 Patel, R.C., Singh, S., Asokan, A., Manickavasagam, R.M., & Jain, A.K. (1993). Extensional
 2048 tectonics in the Himalayan orogen, Zaskar, NW India. In Treloar, P.J., & Searle, M.P.,
 2049 (Eds.), *Himalayan Tectonics*. Geological Society Special Publication, 74, 445-459.
- 2050 Patra, A., & Saha, D. (2019). Stress regime changes in the Main Boundary Thrust zone, Eastern
 2051 Himalaya, decoded from fault-slip analysis. *Journal of Structural Geology*, 120, 29-47.
 2052 <https://doi.org/10.1016/j.jsg.2018.12.010>
- 2053 Patriat, P., & Achache, J. (1984). India–Eurasia collision chronology has implications for crustal
 2054 shortening and driving mechanism of plates. *Nature*, 311, 615– 621.
- 2055 Pearson, O. N., & DeCelles, P.G. (2005). Structural geology and regional tectonic significance of
 2056 the Ramgarh thrust, Himalayan fold-thrust belt of Nepal, *Tectonics*, 24, TC4008.
 2057 <https://doi.org/10.1029/2003TC001617>
- 2058 Pêcher, A. (1989). The metamorphism in the central Himalaya. *Journal of Metamorphic
 2059 Geology*, 7, 31-41.
- 2060 Pêcher, A. (1991). The contact between the Higher Himalayan crystallines and the Tibetan
 2061 sedimentary series: Miocene large-scale dextral shearing. *Tectonics*, 10, 587-598.

- 2062 Pêcher, A., & Le Fort, P. (1986). The metamorphism in central Himalaya, its relations with the
2063 thrust tectonic. In P. Le Fort, M. Colchen, & C. Montenat, (Eds.), *Évolution des domaines*
2064 *orogéniques d'Asie méridionale (de la Turquie à l'Indonésie)*. Science de la Terre, 47,
2065 pp. 285-309.
- 2066 Phukon, P., Sen, K., Singh, P.C., Sen, A., Srivastava, H.B., & Singhal, S. (2019). Characterizing
2067 anatexis in the Greater Himalayan Sequence (Kumaun, NW India) in terms of pressure,
2068 temperature, time and deformation, *Lithos*, 344–345, 22-50.
2069 <https://doi.org/10.1016/j.lithos.2019.04.018>
- 2070 Pilgrim, G.E. & West, W.D. (1928). The structure and correlation of the Simla Rocks. *Memoirs*
2071 *of the Geological Survey of India*, 53, 1-138.
- 2072 Pognante, U., & Benna, P. (1993). Metamorphic zonation, migmatization and leucogranites along
2073 the Everest transect of Eastern Nepal and Tibet: Record of an exhumation history. In
2074 Treloar, P.J., and Searle, M.P., (Eds.), *Himalayan Tectonics*. Geological Society Special
2075 Publication, 74, pp. 323-340.
- 2076 Powers, P.M., Lillie, R.J., & Yeats, R.S. (1998). Structure and shortening of the Kangra and
2077 Dehra Dun reentrants, Sub-Himalaya, India. *Geological Society of America Bulletin*,
2078 110, 1010-1027.
- 2079 Quade, J., Cater, J.M.L., Ohja, T.P., Adam, J., & Harrison, T.M. (1995). Late Miocene
2080 environmental change in Nepal and the northern Indian subcontinent: stable isotopic
2081 evidence from paleosols. *Geological Society of America Bulletin*, 107, 1381-1397
- 2082 Quade, J., Cerling, T. & Bowman, J. (1989). Development of Asian monsoon revealed by
2083 marked ecological shift during the latest Miocene in northern Pakistan. *Nature* 342, 163–
2084 166. <https://doi.org/10.1038/342163a0>
- 2085 Quidelleur, X., Grove, M., Lovera, O.M., Harrison, T. M., Yin, A., & Ryerson F.J. (1997). The
2086 thermal evolution and slip history of the Renbu Zedong Thrust, southeastern Tibet.
2087 *Journal of Geophysical Research*, 102, 2659-2679.
- 2088 Raiverman, V., Kunte, S. V., & Mukherjee, A. (1983). Basin geometry, Cenozoic sedimentation,
2089 and hydrocarbon prospects in northwestern Himalaya and Indo-Gangetic plains.
2090 *Petroleum Asia Journal*, 6, 67–92.
- 2091 Rajendran, K., Parameswaran, R.M., & Rajendran, C. (2017). Seismotectonic perspectives on the
2092 Himalayan arc and contiguous areas: Inferences from past and recent earthquakes. *Earth-*
2093 *Science Reviews*, 173, 1-30. <https://doi.org/10.1016/j.earscire.2017.08.003>
- 2094 Rapa, G., Mosca, P., Groppo, C., & Rolfo, F. (2018). Detection of tectonometamorphic
2095 discontinuities within the Himalayan orogen: Structural and petrological constraints from
2096 the Rasuwa district, central Nepal Himalaya. *Journal of Asian Earth Sciences*, 158, 266-
2097 286. <https://doi.org/10.1016/j.jseaes.2018.02.021>
- 2098 Ray, S. (1947). Zonal metamorphism in the eastern Himalayas and some aspects of local
2099 geology. *The Quarterly journal of the Geological, Mining, and Metallurgical Society of*
2100 *India*, 19, 117-140.
- 2101 Reuber, I. (1986). Two peridotite units superposed by intra-oceanic thrusting in the Spongtag
2102 Klippe (Ladakh-Himalaya). *Sciences Geologiques [Bulletin]*, 39, 391-402.
- 2103 Roberts, A. G., Weinberg, R. F., Hunter, N. J. R., & Ganade, C. E. (2020). Large-scale rotational
2104 motion within the Main Central Thrust Zone in the Darjeeling-Sikkim Himalaya, India.
2105 *Tectonics*, 39, e2019TC005949. <https://doi.org/10.1029/2019TC005949>

- 2106 Robinson, D.M., DeCelles, P.G., & Copeland, P. (2006). Tectonic evolution of the Himalayan
2107 thrust belt in western Nepal: Implications for channel flow models, *Geological Society of*
2108 *America Bulletin*, 118, 865–885. <https://doi.org/10.1130/B25911.1>
- 2109 Robinson, D.M., DeCelles, P.G., Garzione, C.N., Pearson, O.N., Harrison, T.M., Catlos, E.J.
2110 (2003). Kinematic model for the Main Central Thrust in Nepal. *Geology* 31, 359– 362.
- 2111 Robinson, D.M., DeCelles, P.G., Patchett, P.J., & Garzione, C.N. (2001). The kinematic
2112 evolution of the Nepalese Himalaya interpreted from Nd isotopes. *Earth and Planetary*
2113 *Science Letters* 192, 507– 521.
- 2114 Robyr, M., & Lanari, P. (2020). Kinematic, metamorphic, and age constraints on the Miyar
2115 Thrust Zone: Implications for the Eohimalayan history of the High Himalayan Crystalline
2116 of NW India. *Tectonics*, 39, e2020TC006379. <https://doi.org/10.1029/2020TC006379>
- 2117 Rolfo, F., Groppo, C. & Mosca, P. (2014). Petrological constraints of the ‘Channel Flow’ model
2118 in eastern Nepal. In: Mukherjee, S., Carosi, R., van der Beek, P. A., Mukherjee, B. K. &
2119 Robinson, D. M. (eds) *Tectonics of the Himalaya*. Geological Society, London, Special
2120 Publications, 412. <https://doi.org/10.1144/SP412.4>
- 2121 Rolland, Y., Picard, C., Pecher, A., Lapierre, H., Bosch, D., & Keller, F. (2002). The cretaceous
2122 Ladakh arc of NW himalaya—slab melting and melt–mantle interaction during fast
2123 northward drift of Indian Plate. *Chemical Geology*, 182(2–4), 139-178.
2124 [https://doi.org/10.1016/S0009-2541\(01\)00286-8](https://doi.org/10.1016/S0009-2541(01)00286-8)
- 2125 Rowley, D.B. (1996). Age of collision between India and Asia: A review of the stratigraphic
2126 data. *Earth and Planetary Science Letters*, 145, 1-13.
- 2127 Sachan, H.K., Kohn, M.J., Saxena, A., & Corrie, S.L. (2010). The Malari leucogranite, Garhwal
2128 Himalaya, northern India: Chemistry, age, and tectonic implications. *Geological Society*
2129 *of America Bulletin*, 122, 1865-1876. <https://doi.org/10.1130/B30153.1>
- 2130 Sakai, H., Iwano, H., Danhara, T., Takigami, Y., Rai, S.M., Upreti, B.N. & Hirata, T. (2013).
2131 Rift-related origin of Kuncha Formation. *Island Arc*, 22, 338-360.
2132 <https://doi.org/10.1111/iar.12021>
- 2133 Sanyal, P., & Sinha, R. (2010). Evolution of the Indian summer monsoon: synthesis of
2134 continental records. Geological Society, London, Special Publications, 342, 153-183.
2135 <https://doi.org/10.1144/SP342.11>
- 2136 Saxena, M.N. (1971). The crystalline axis of the Himalaya: The Indian shield and continental
2137 drift. *Tectonophysics*, 12(6), 433-447. [https://doi.org/10.1016/0040-1951\(71\)90044-8](https://doi.org/10.1016/0040-1951(71)90044-8)
- 2138 Schelling, D. & Arita, K. (1991). Thrust tectonics, crustal shortening, and the structure of the far-
2139 eastern Nepal Himalayas. *Tectonics*, 10, 851-862.
- 2140 Schelling, D. (1992). The tectonostratigraphy and structure of the Eastern Nepal Himalaya.
2141 *Tectonics*, 11, 925-943.
- 2142 Schmalholz, S. M., & Podladchikov, Y. Y. (2013). Tectonic overpressure in weak crustal-scale
2143 shear zones and implications for the exhumation of high-pressure rocks. *Geophysical*
2144 *Research Letters*, 40, 1984–1988. <https://doi.org/10.1002/grl.50417>
- 2145 Schneider, C., & Masch, L. (1993). The metamorphism of the Tibet Series from the Manang
2146 area, Marsyandi Valley, central Nepal. In Trearlor, P.J., Searle, M.P., (Eds.), *Himalayan*
2147 *Tectonics*. Geological Society Special Publication, 74, pp. 357-374.
- 2148 Scotese, C.R., Gahagan, L.M. & Larson, R.L. (1988). Plate tectonic reconstructions of the
2149 Cretaceous and Cenozoic ocean basins. *Tectonophysics*, 155, 27-48.
- 2150 Searle, M.P. (1999). Extensional and compressional faults in the Everest-Lhotse massif, Khumbu
2151 Himalaya, Nepal. *Journal of the Geological Society London*, 156, 227-240.

- 2152 Searle, M., Avouac, J.-, Elliott, J., & Dyck, B. (2017). Ductile shearing to brittle thrusting along
 2153 the Nepal Himalaya: Linking Miocene channel flow and critical wedge tectonics to April
 2154 25 2015 Gorkha earthquake. *Tectonophysics*, 714-715, 117-124.
 2155 <https://doi.org/10.1016/j.tecto.2016.08.003>
- 2156 Searle, M. P., Law, R.D., Godin, L., Larson, L.P., Streule, M.J., Cottle, J.M., & Jessup, M.J.
 2157 (2008). Defining the Himalayan Main Central Thrust in Nepal. *Journal of the Geological*
 2158 *Society*, 165(2), 523–534.
- 2159 Searle, M.P., Law, R.D., & Jessup, M.J. (2006). Crustal structure, restoration and evolution of
 2160 the Greater Himalaya in Nepal-South Tibet: implications for channel flow and ductile
 2161 extrusion of the middle crust. *Geological Society, London, Special Publications*, 268,
 2162 355-378. <https://doi.org/10.1144/GSL.SP.2006.268.01.17>
- 2163 Searle, M.P., Metcalfe, R.P., Rex, A.J., & Norry, M.J. (1993). Field relations, petrogenesis and
 2164 emplacement of the Bhagirathi leucogranite, Garhwal Himalayas. In Trearlor, P.J., &
 2165 Searle, M.P., (Eds.), *Himalayan Tectonics*. *Geological Society Special Publication*, 74,
 2166 pp. 429-444.
- 2167 Searle, M.P. & Rex, A.J. (1989). Thermal model for the Zaskar Himalaya. *Journal of*
 2168 *Metamorphic Geology*, 7, 127-134.
- 2169 Şengör, A.M.C. & Atayman, S. (2009). The Permian extinction and the Tethys; an exercise in
 2170 global geology. *Special Paper - Geological Society of America*, 448.
 2171 <https://doi.org/10.1130/2009.2448>
- 2172 Siddiqui, R.H., Jan, M.Q. & Khan, M.A. (2012). Petrogenesis of Late Cretaceous lava flows
 2173 from a Ceno-Tethyan Island Arc: the Raskoh Arc, Balochistan, Pakistan. *Journal of*
 2174 *Asian Earth Sciences*, 59, 24-28.
- 2175 Siddiqui, R.H., Jan, M.Q., Khan, M.A., Kakar, M.I. & Foden, J.D. (2017). Petrogenesis of the
 2176 Late Cretaceous Tholeiitic volcanism and ocean island arc affinity of the Chagai arc,
 2177 western Pakistan. *Acta Geologica Sinica*, 91, 1248-1263.
- 2178 Simpson, R.L., Parrish, R.R., Searle, M.P., & Waters, D.J. (2000). Two episodes of monazite
 2179 crystallization during metamorphism and crustal melting in the Everest region of the
 2180 Nepalese Himalaya. *Geology*, 28, 403-406.
- 2181 Sinha-Roy, S. (1982). Interactions of Tethyan blocks and the evolution of Asian fold belts.
 2182 *Tectonophysics*, 82, 271-297.
- 2183 Spear, F. S. (1993). *Metamorphic Phase Equilibria and Pressure–Temperature–Time Paths*.
 2184 Washington, DC: Mineralogical Society of America.
- 2185 Spear, F. S., & Daniel, C. G. (1998). Three-dimensional imaging of garnet porphyroblast sizes
 2186 and chemical zoning: Nucleation and growth history in the garnet zone. *Geological*
 2187 *Materials Research*, 1, 44.
- 2188 Spear, F. S., & Peacock, S. M. (1989). Metamorphic pressure-temperature-time paths. *American*
 2189 *Geophysical Union Short Course in Geology*, 7, 102.
- 2190 Spear, F.S. & Rumble, D., III (1986). Pressure, temperature and structural evolution of the
 2191 Orfordville Belt, west-central New Hampshire. *Journal of Petrology*, 27, 1071-1093.
- 2192 Spear, F.S. (1986). P-T PATH:A FORTRAN program to calculate pressure-temperature paths
 2193 from zoned metamorphic garnets. *Computers in Geoscience*, 12, 247-266.
- 2194 Spear, F.S., & Selverstone, J. (1983). Quantitative P-T paths from zoned minerals: Theory and
 2195 tectonic applications. *Contributions to Mineralogy and Petrology*, 83, 348–357.

- 2196 Spear, F.S., Kohn, M.J., & Paetzold, S. (1995). Petrology of the regional sillimanite zone, west-
2197 central New Hampshire, USA, with implications for the development of inverted
2198 isograds. *American Mineralogist*, 80, 361-376.
- 2199 Spear, F.S., Selverstone, J., Hickmott, D., Crowley, P. and Hodges, K.V. (1984). P-T paths from
2200 garnet zoning: A new technique for deciphering tectonic processes in crystalline terranes.
2201 *Geology*, 12, 87-90.
- 2202 Srivastava, V., Mukul, M., Barnes, J.B., & Mukul, M. (2018). Geometry and kinematics of Main
2203 Frontal thrust-related fault propagation folding in the Mohand Range, northwest
2204 Himalaya. *Journal of Structural Geology*, 115, 1-18.
2205 <https://doi.org/10.1016/j.jsg.2018.06.022>
- 2206 Stäubli, A. (1989). Polyphase metamorphism and the development of the Main Central thrust:
2207 *Journal of Metamorphic Geology*, 7, 73–93.
- 2208 Stephenson, B. J., Waters, D. J., & Searle, M. P. (2000). Inverted metamorphism and the Main
2209 Central Thrust: Field relations and thermobarometric constraints from the Kishtwar
2210 Window, NW Indian Himalaya. *Journal of Metamorphic Geology*, 18(5), 571–590.
2211 <https://doi.org/10.1046/j.1525-1314.2000.00277.x>
- 2212 Stickroth, S. F., Carrapa, B., DeCelles, P. G., Gehrels, G. E., & Thomson, S. N. (2019). Tracking
2213 the growth of the Himalayan fold-and-thrust belt from lower Miocene foreland basin
2214 strata: Dumri Formation, western Nepal. *Tectonics*, 38, 3765– 3793.
2215 <https://doi.org/10.1029/2018TC005390>
- 2216 Stöcklin, J. (1980). Geology of Nepal and its regional frame. *Journal of the Geological Society*,
2217 137, 1-34.
- 2218 Subedi, S., Hetényi, G., Vergne, J., Bollinger, L., Lyon-Caen, H., Farra, V., Adhikari, L.B., &
2219 Gupta, R.M. (2018). Imaging the Moho and the Main Himalayan Thrust in Western
2220 Nepal with receiver functions. *Geophysical Research Letters*, 45, 13,222– 13,230.
2221 <https://doi.org/10.1029/2018GL080911>
- 2222 Thakur, C., & Kumar, S. (1994). Seismotectonics of the October 20 1991 Uttarkashi earthquake
2223 in Garhwal, Himalaya, North India. *Terra Nova*, 6, 90-94. <https://doi.org/10.1111/j.1365-3121.1994.tb00637.x>
- 2224
- 2225 Thakur, S.S., Patel, S.C., & Singh, A.K., (2015). A P–T pseudosection modelling approach to
2226 understand metamorphic evolution of the Main Central Thrust Zone in the Alaknanda
2227 valley, NW Himalaya. *Contributions to Mineralogy and Petrology*, 170:2.
2228 <https://doi.org/10.1007/s00410-015-1159-y>
- 2229 Thakur, V.C., Jayangondaperumal, R., & Malik, M.A. (2010). Redefining Medlicott–Wadia's
2230 main boundary fault from Jhelum to Yamuna: An active fault strand of the main
2231 boundary thrust in northwest Himalaya, *Tectonophysics*, 489(1–4), 29-42.
2232 <https://doi.org/10.1016/j.tecto.2010.03.014>
- 2233 Tobgay, T., McQuarrie, N., Long, S., Kohn, M.J., & Corrie, S.L. (2012). The age and rate of
2234 displacement along the Main Central Thrust in the western Bhutan Himalaya. *Earth and*
2235 *Planetary Science Letters*, 319–320, 146-158. <https://doi.org/10.1016/j.epsl.2011.12.005>
- 2236 Tripathi, C., & Singh, G. (1987). Gondwana and associated rocks of the Himalaya and their
2237 significance. In: McKenzie, G.D., (Ed.), *Gondwana Six; Stratigraphy, sedimentology, &*
2238 *paleontology*. AGU Geophysical Monograph, 41, pp. 195-205.
- 2239 Trivedi, J.R., Gopalan, K., & Valdiya, K.S. (1984). Rb-Sr ages of granitic rocks within the
2240 Lesser Himalaya nappes, Kumaun, India. *Journal of the Geological Society India*, 25,
2241 641-654.

- 2242 Upreti, B.N. (1999). An overview of the stratigraphy and tectonics of the Nepal Himalaya.
 2243 *Journal of Asian Earth Sciences*, 17, 741-753.
- 2244 Upreti, B.N., & Le Fort, P. (1999). Lesser Himalayan crystalline nappes of Nepal: Problems of
 2245 their origin. In Macfarlane, A., Sorkhabai, R.B., & Quade, J. (Eds.), *Himalaya and Tibet:*
 2246 *Mountain roots to mountain tops*. Geological Society of America Special Paper, 328, pp.
 2247 225-238.
- 2248 Upreti, B.N., & Yoshida, M. (2005). Basement history and provenance of the Tethys sediments
 2249 of the Himalaya: an appraisal based on recent geochronologic and tectonic data. Abstract.
 2250 The 1st International Conference on the “Geology of Tethys, 2005”, 12–14 November
 2251 2005, Cairo.
- 2252 Valdiya, K.S. (1980). *Geology of the Kumaon Lesser Himalaya*. Wadia Institute of Himalaya,
 2253 Dehra Dun, India, 291 pp.
- 2254 Valdiya, K.S. (1988). Tectonics and the evolution of the central sector of the Himalaya.
 2255 *Philosophical Transactions of the Royal Society of London, A.*, 326, 151-175.
- 2256 Valdiya, K.S. (1992). The Main Boundary Thrust Zone of the Himalaya, India. *Annales*
 2257 *Tectonicae* 6, suppl., 54-84.
- 2258 van Hinsbergen, D.J.J., Lippert, P. C.; Dupont-Nivet, G., McQuarrie, N., Doubrovine, P.V.,
 2259 Spakman, W. & Torsvik, T.H. (2012). Greater India Basin hypothesis and two-stage
 2260 Cenozoic collision between India and Asia. *Proceedings of the National Academy of*
 2261 *Sciences of the United States of America*, 109, 7659-7664.
- 2262 Vannay, J.-C., & Grasemann, B. (1998). Inverted metamorphism in the High Himalaya of
 2263 Himachal Pradesh (NW India): phase equilibria versus thermobarometry. *Schweizerische*
 2264 *Mineralogische und Petrographische Mitteilungen*, 78, 107-132.
- 2265 Vannay, J.-C., & Steck, A. (1995). Tectonic evolution of the High Himalaya in upper Lahul (NW
 2266 Himalaya, India). *Tectonics*, 14, 253-263.
- 2267 Vannay, J.-C., Grasemann, B., Rahn, M., Frank, W., Carter, A., Baudraz, V., Cosca, M. (2004).
 2268 Miocene to Holocene exhumation of metamorphic crustal wedges in the NW Himalaya:
 2269 Evidence for tectonic extrusion coupled to fluvial erosion. *Tectonics* 23, TC1014.
- 2270 Vannay, J.-C., & Hodges, K.V. (1996). Tectonometamorphic evolution of the Himalayan
 2271 metamorphic core between Annapurna and Dhaulagiri, central Nepal. *Journal of*
 2272 *Metamorphic Geology*, 14, 635-656.
- 2273 Von Loczy, L. (1907). Beobachtungen im östlichen Himalaya (vom 8. his 28. Febr.. 1878).
 2274 *Foldt. Kozl.* 35(9): 1-24
- 2275 Wakita, K. & Metcalfe, I. (2005). Ocean plate stratigraphy in East and Southeast Asia. *Journal of*
 2276 *Asian Earth Sciences*, 24, 679-702.
- 2277 Wang, J.M., Zhang, J.J., & Wang, X.X. (2013). Structural kinematics, metamorphic P–T profiles
 2278 and zircon geochronology across the Greater Himalayan Crystalline Complex in south-
 2279 central Tibet: implication for a revised channel flow. *J. Meta. Geol.*, 31, 607-628.
 2280 <https://doi.org/10.1111/jmg.12036>
- 2281 Wang, J.-M., Zhang, J.-J., Liu, K., Zhang, B., Wang, X.-X., Rai, S., & Scheltens, M. (2016).
 2282 Spatial and temporal evolution of tectonometamorphic discontinuities in the central
 2283 Himalaya: Constraints from P-T paths and geochronology. *Tectonophysics*, 679, 41–60.
 2284 <https://doi.org/10.1016/j.tecto.2016.04.035>
- 2285 Wang, X., Wei, S., & Wu, W. (2017). Double-ramp on the Main Himalayan Thrust revealed by
 2286 broadband waveform modeling of the 2015 Gorkha earthquake sequence. *Earth and*
 2287 *Planetary Science Letters*, 473, 83-93. <https://doi.org/10.1016/j.epsl.2017.05.032>

- 2288 Waters D.J. (2019). Metamorphic constraints on the tectonic evolution of the High Himalaya in
2289 Nepal: the art of the possible, in Treloar J. and Searle M., eds., *Himalayan Tectonics: A*
2290 *Modern Synthesis*. Geological Society, London, Special Publications, 483.
2291 <https://doi.org/10.1144/SP483-2018-187>
- 2292 Webb, A.G., Yin, A., Harrison, T.M., C  lerier, J., & Burgess, W.P. (2007). The leading edge of
2293 the Greater Himalayan Crystalline complex revealed in the NW Indian Himalaya:
2294 Implications for the evolution of the Himalayan orogen. *Geology*, 35 (10), 955–
2295 958. <https://doi.org/10.1130/G23931A.1>
- 2296 Webb, A.G., Schmitt, A.K., He, D., & Weigand, E.L. (2011). Structural and geochronological
2297 evidence for the leading edge of the Greater Himalayan Crystalline Complex in the
2298 central Nepal Himalaya. *Earth and Planetary Science Letters*, 304, 483-495.
2299 <https://doi.org/10.1016/j.epsl.2011.02.024>
- 2300 Whipple, K.X., Shirzaei, M., Hodges, K., & Arrowsmith, J.R. (2016). Active shortening within
2301 the Himalayan orogenic wedge implied by the 2015 Gorkha earthquake. *Nature*
2302 *Geoscience*, 9, 711-716.
- 2303 White, R.W., Powell, R., Holland, T.J.B., Johnson, T.E., & Green, E.C.R. (2014). New mineral
2304 activity-composition relations for thermodynamic calculations in metapelitic systems.
2305 *Journal of Metamorphic Geology*, 32, 261– 286.
- 2306 Wiesmayr, G., & Grasemann, B. (2002). Eohimalayan fold and thrust belt: implications for the
2307 geodynamic evolution of the NW Himalaya (India). *Tectonics* 2, 1058.
- 2308 Willems, H., Zhou, Z., Zhang, B., & Gr  fe, K-U. (1996). Stratigraphy of the upper cretaceous
2309 and lower tertiary strata in the Tethyan Himalayas of Tibet (Tingri area, China). *Geol*
2310 *Rundsch* 85, 723. <https://doi.org/10.1007/BF02440107>
- 2311 Wu, C., Nelson, K.D., Wortman, G., Samson, S., Yue, Y., Li, J., Kidd, W.S.F., & Edward, M.A.
2312 (1998). Yadong cross structure and South Tibetan Detachment in the east central
2313 Himalaya (89–90E). *Tectonics* 17, 28–45.
- 2314 Wu, F-Y., Liu, X-C., Liu, Z-C., Wang, R-C., Xie, L., Wang, J-M., Ji, W-Q., Yang, L., Liu, C.,
2315 Khanal, G.P., He, S-X. (2020). Highly fractionated Himalayan leucogranites and
2316 associated rare-metal mineralization, *Lithos*, 352–353, 105319.
2317 <https://doi.org/10.1016/j.lithos.2019.105319>
- 2318 Yang, T., Ma, Y., Bian, W., Jin, J., Zhang, S., Wu, H., Li, H., Yang, Z., & Ding, J. (2015).
2319 Paleomagnetic results from the Early Cretaceous Lakang Formation lavas: Constraints on
2320 the paleolatitude of the Tethyan Himalaya and the India–Asia collision. *Earth and*
2321 *Planetary Science Letters*, 428, 120-133. <https://doi.org/10.1016/j.epsl.2015.07.040>
- 2322 Ye, H., Zhang W., Yu Z., & Xia G. (1981). The seismicity and regional crustal movement in the
2323 Himalaya region. In *Geological and ecological studies of the Qinghai-Xizang Plateau*, 1,
2324 New York, 65-80.
- 2325 Yeats, R.S., Nakata, T., Farah, A., Fort, M., Mirza, M.A., Pandey, M.R., & Stein, R.S. (1992).
2326 The Himalayan Frontal Fault System. *Annales Tectonicae*, 6 suppl., 85-98.
- 2327 Yin, A. & Harrison, T.M. (2000). Geologic evolution of the Himalayan-Tibet orogen. *Annual*
2328 *Reviews in Earth and Planetary Science*, 28, 211-280.
- 2329 Yin, A. (2006). Cenozoic tectonic evolution of the Himalayan orogen as constrained by along-
2330 strike variation of structural geometry, exhumation history, and foreland sedimentation.
2331 *Earth-Science Reviews* 76, 1 –131.

- 2332 Yin, A., Harrison, T.M., Murphy, M.A., Grove, M., Nie, S., Ryerson, F.J., Feng, W.X., & Le,
 2333 C.Z. (1999). Tertiary deformation history of southeastern and southwestern Tibet during
 2334 the Indo-Asian collision. *Geological Society of America Bulletin*, 111, 1644–1664.
- 2335 Yin, A., Harrison, T.M., Ryerson, F.J., Wenji, C., Kidd, W.S.F., & Copeland, P. (1994). Tertiary
 2336 structural evolution of the Gangdese thrust system, southeastern Tibet. *Journal of*
 2337 *Geophysical Research*, 99, 18175-18201.
- 2338 Yoshida, M., & Upreti, B.N (2006). Neoproterozoic India within East Gondwana: Constraints
 2339 from recent geochronologic data from Himalaya. *Gondwana Research*, 10(3-4), 349-356.
 2340 <https://doi.org/10.1016/j.gr.2006.04.011>
- 2341 Yuan, J., Yang, Z., Deng, C., Krijgsman, W., Hu, X., Li, S., Shen, Z., Qin, H., An, W., He, H.,
 2342 Ding, L., Guo, Z., & Zhu, R. (2020). Rapid drift of the Tethyan Himalaya terrane before
 2343 two-stage India-Asia collision. *National Science Review*, 0, 1–13.
 2344 <https://doi.org/10.1093/nsr/nwaa173>
- 2345 Zhang, H., Harris, N., Parrish, R., Zhang, L., & Zhao, Z. (2004). U-Pb ages of Kude and Sajia
 2346 leucogranites in Sajia dome from North Himalaya and their geological implications.
 2347 *Chinese Science Bulletin*, 49, 2087. <https://doi.org/10.1360/04wd0198>
- 2348 Zhao, W., Nelson K.D., & Project INDEPTH (1993). Deep seismic reflection evidence for
 2349 continental underthrusting beneath southern Tibet. *Nature*, 366, 557-559.
- 2350 Zhou, Z., Kusky, T.M., & Tang, C-C. (2019). Coulomb stress change pattern and aftershock
 2351 distributions associated with a blind low-angle megathrust fault, Nepalese Himalaya.
 2352 *Tectonophysics*, 767, 228161. <https://doi.org/10.1016/j.tecto.2019.228161>
- 2353 Zhu, B., Kidd, W.S.F., Rowley, D.B., Currie, B.S., & Shafique, N. (2005). Age of initiation of
 2354 the India–Asia collision in the east-central Himalaya. *Journal of Geology* 113, 265–285.
- 2355 Zhu, D.C., Zhao, Z.D., Niu, Y.L., Dilek, Y., Hou, Z.Q. & Mo, X.X. (2013). The origin and pre-
 2356 Cenozoic evolution of the Tibetan Plateau. *Gondwana Research*, 23, 1429-1454.
- 2357 Ziyabrev, S.V., Kojima, S., & Ahmad, T. (2008). Radiolarian biostratigraphic constraints on the
 2358 generation of the Nidar ophiolite and the onset of Dras arc volcanism: Tracing the
 2359 evolution of the closing Tethys along the Indus – Yarlung-Tsangpo suture. *Stratigraphy*,
 2360 5(1), 99-112.
- 2361
- 2362
- 2363
- 2364
- 2365
- 2366
- 2367
- 2368
- 2369
- 2370
- 2371
- 2372
- 2373
- 2374
- 2375
- 2376
- 2377

2378

Table 1. Conventional P-T data from samples collected along the Darondi Khola.

Sample ^a	Gibbs Core P (±1kbar)	Gibbs Core T (±25°C)	Gibbs Rim P (± 1kbar)	Gibbs Rim T (±25°C)	Conv. Rim P (kbar, ±1σ)	Conv. Rim T (°C, ±1σ)
Lower LHF						
DH16	- ^b	-	-	-	5.0±1.0	520±25
DH17	6.0	510	7.0	525	6.8±1.0	525±15
DH19	5.5	475	6.0	525	6.2±0.5	527±12
Middle LHF						
DH22	6.0	498	5.0	525	5.2±1.0	520±25
DH23	7.0	525	7.3	575	7.2±2.0	540±35
DH26	6.5	500	5.5	520	5.5±1.0	524±25
DH30	-	-	-	-	8.5±2.0	570±20
DH75A	8.5	530	9.0	560	8.5±2.0	570±20
DH75B	8.0	500	8.0	560	8.5±2.0	570±20
Upper LHF						
DH38	-	-	-	-	8.2±1.0	578±20
DH57	-	-	-	-	11.5±2.0	640±25
DH58	-	-	-	-	11.5±2.0	640±25
DH71	-	-	-	-	11.5±1.0	640±20
GHC						
DH60	-	-	-	-	10.5±1.0	652±10
DH61	-	-	-	-	9.1±2.0	625±12
DH63	-	-	-	-	11.5±1.5	705±25
DH66	-	-	-	-	7.6±1.0	660±12
DH67	-	-	-	-	10.2±2.0	715±5

2379

^a See Figure 3 for samples location. Conditions estimated from Kohn et al. (2001).

2380

^b “-“ not reported.

2381

2382

2383

2384

2385

2386

2387

2388

2389

2390

2391

2392

2393

2394

2395

2396

2397

2398

2399 **Table 2.** P-T data generated from samples collected along the Darondi Khola using garnet
 2400 isopleth thermobarometry.

Sample ^a	Isopleth Core P (± 1 kbar)	Isopleth Core T ($\pm 25^\circ\text{C}$)	Isopleth Rim P (± 1 kbar)	Isopleth Rim T ($\pm 25^\circ\text{C}$)
Lower LHF				
DH17	4.5	540	4.5	560
DH19	4.0	520	4.8	550
Middle LHF				
DH22	4.8	540	6.0	580
DH23	5.1	525	6.0	580
DH26	6.5	550	5.5	560
DH75A	6.8	540	6.5	580
DH75B	7.5	550	8.8	590
Upper LHF				
DH51	- ^b	-	7.0	650
DH58	6.0	550	-	-
GHC				
DH60	-	-	7.5	570
DH61	7.0	580	7.5	600
DH63	-	-	10.5	650
DH66	-	-	7.5	550

2401 ^a See Figure 3 for sample locations.

2402 ^b “-“ not reported.

2403

2404 **Table 3.** Bulk rock compositions (wt%) from lower and middle LHF samples.

Analyte/Sample ^a	DH17	DH19	DH22/23	DH26	DH30	DH75A	DH75B
SiO ₂	45.39	66.04	45.22	76.04	50.89	70.24	68.75
Al ₂ O ₃	27.31	16.36	28.09	11.79	27.80	12.79	8.16
Fe ₂ O ₃ (T)	9.18	7.12	6.37	3.52	6.11	4.98	3.78
MnO	0.10	0.17	0.20	0.05	0.02	0.02	0.02
MgO	2.81	1.88	1.50	1.24	2.03	1.78	1.52
CaO	0.30	0.44	0.51	0.58	0.20	0.39	0.46
Na ₂ O	1.07	0.45	1.57	3.54	1.44	1.14	1.51
K ₂ O	7.72	5.14	7.26	1.22	6.12	2.97	1.99
TiO ₂	0.86	0.52	0.86	0.40	0.79	0.49	0.35
P ₂ O ₅	0.11	0.16	0.13	0.11	0.14	0.09	0.07
LOI	n.m.	2.15	n.m.	2.26	5.21	4.89	n.m.
Total	94.8	100.4	91.7	100.7	100.7	99.8	86.6

2405 ^a See Figure 3 for sample locations.

2406

2407

2408

2409

2410

2411

2412 **Table 4.** Bulk rock compositions (wt%) from upper LHF and GHC samples.

Analyte/Sample ^a	DH51	DH58B	DH60	DH61	DH63	DH66	DH67
	LHF samples				GHC samples		
SiO ₂	66.13	55.66	71.51	55.47	69.01	68.35	79.92
Al ₂ O ₃	15.14	23.82	12.62	19.54	13.88	10.47	9.01
Fe ₂ O ₃ (T)	5.29	4.48	5.80	7.76	6.69	5.44	3.57
MnO	0.03	0.19	0.04	0.14	0.10	0.07	0.02
MgO	2.31	1.66	2.41	4.71	1.99	2.00	1.65
CaO	0.21	3.38	1.02	2.59	1.15	1.07	1.37
Na ₂ O	0.58	6.46	2.55	4.23	2.46	1.52	2.18
K ₂ O	3.78	2.08	2.68	3.84	2.32	2.53	1.22
TiO ₂	0.52	0.67	0.65	0.99	0.68	0.54	0.62
P ₂ O ₅	0.12	0.01	0.15	0.03	0.15	0.09	0.05
LOI	5.89	n.m.	n.m.	n.m.	n.m.	n.m.	1.28
Total	100	98.4	99.4	99.3	98.4	92.1	100.9

2413 ^a See Figure 3 for sample locations.

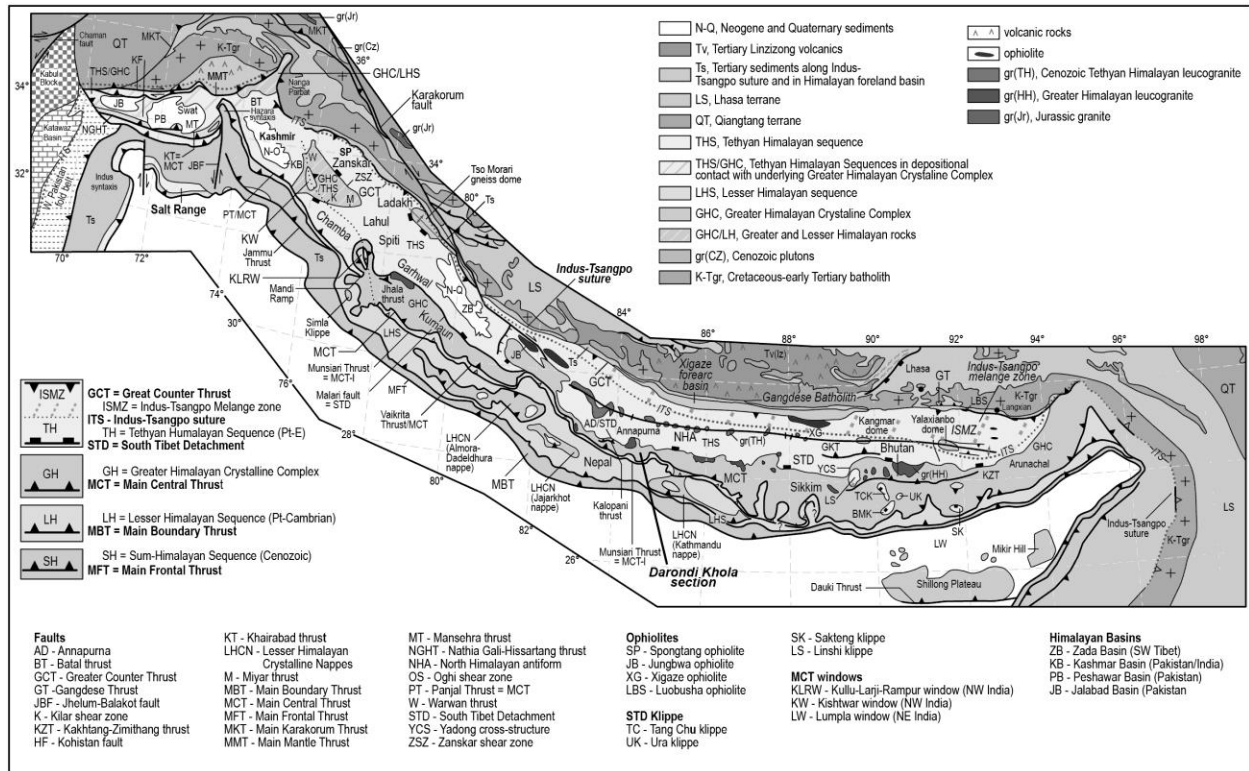


Figure 1. Geological map of the Himalayas after Yin (2006). Geological map of the Himalayas after Yin (2006). See Figure 2 for a cross-section through central Nepal and Figures 3-5 for the sample transect taken across the MCT shear zone along the Darondi Khola. See supplementary files for this figure in color.

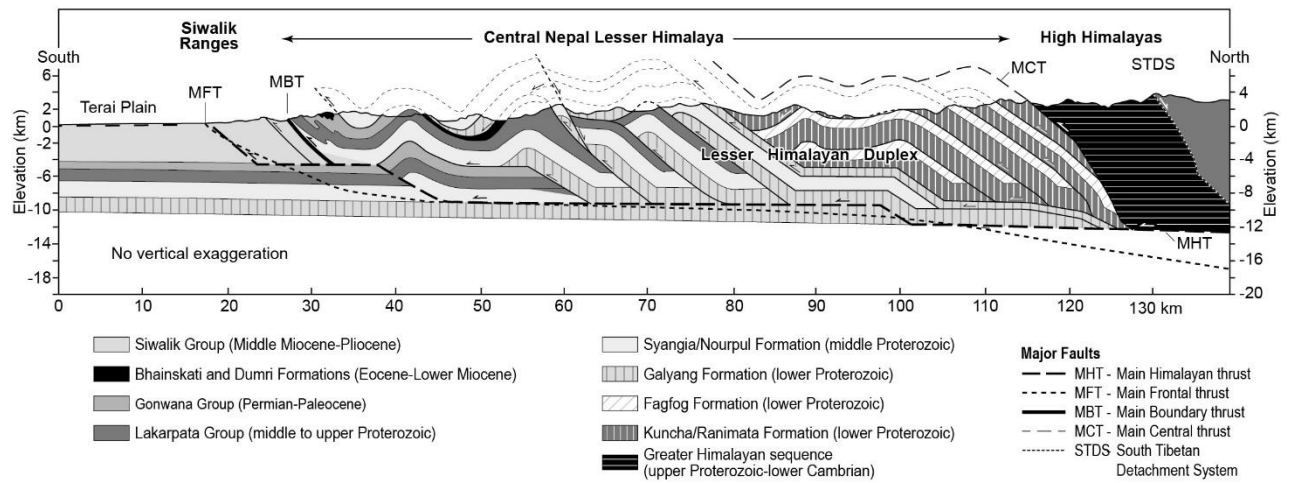


Figure 2. Generalized cross-section through the Himalayas in central Nepal after DeCelles (2015) and Robinson et al. (2006). See additional cross-sections in the range in DeCelles et al. (2020).

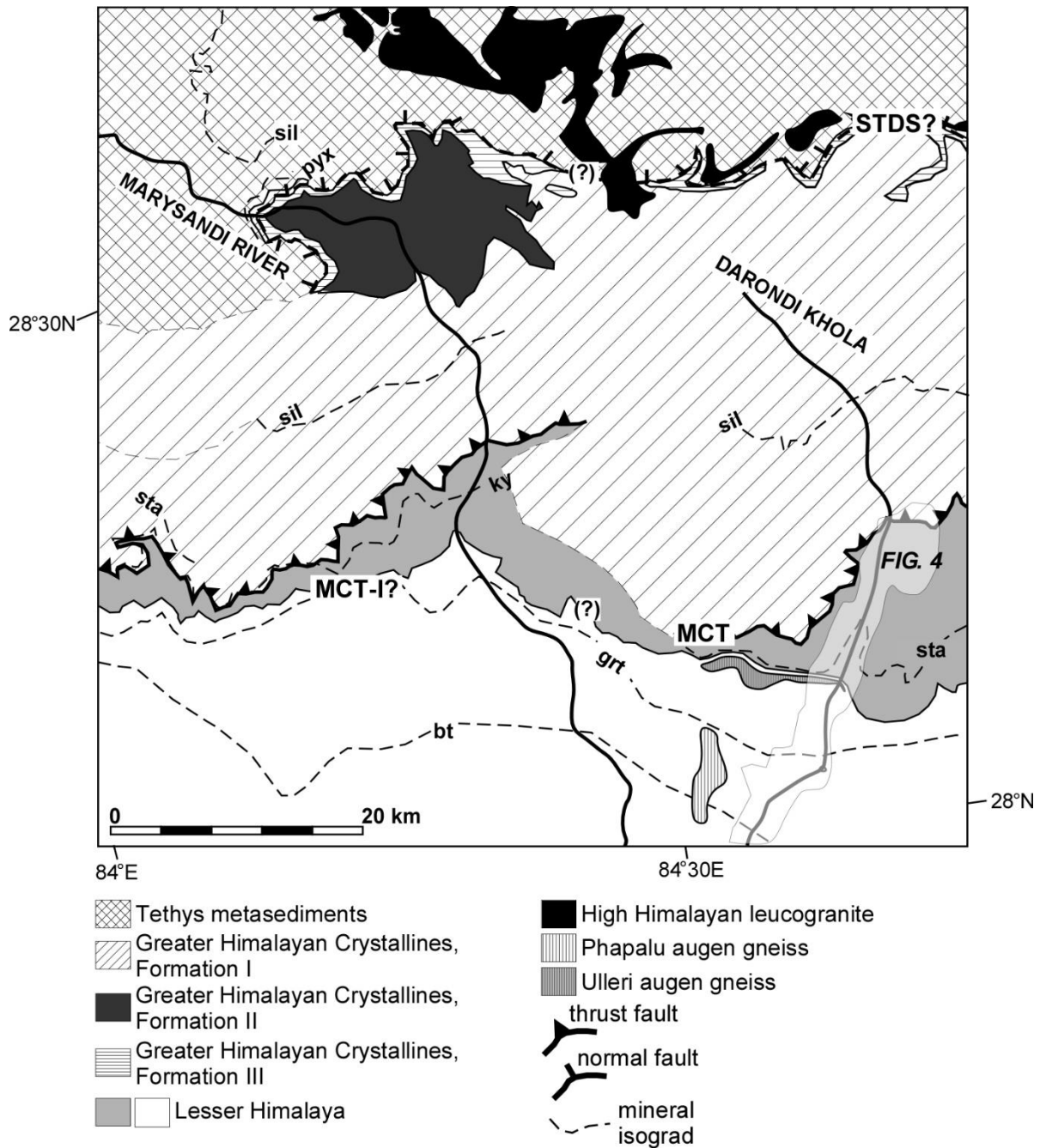


Figure 3. Generalized geological map of the Annapurna-Manaslu-Ganesh region of central Nepal after Colchen et al. (1980). Isograds are dashed and labeled: bt= biotite, grt= garnet; ky= kyanite; sta= staurolite; sil= sillimanite; pyx= pyroxene, carbonate lithologies. STDS? = the presence of the South Tibetan Detachment is debated; MCT= Main Central Thrust; MCT-I?= the presence of Arita's (1983) thrust at the base of the MCT shear zone is debated.

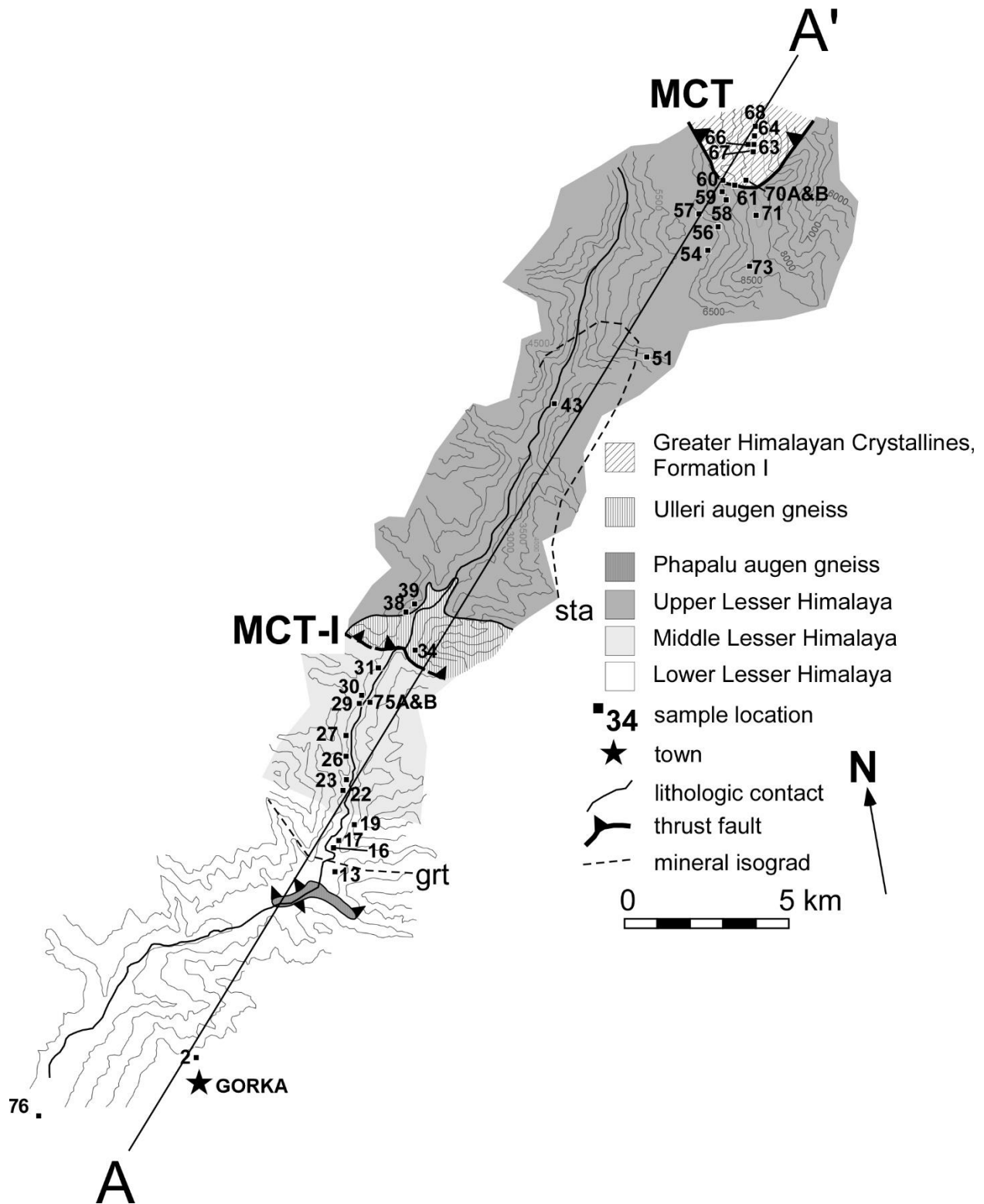


Figure 4. Sample location map from rocks collected along the Daroni Khola. The contour interval is 500 ft. See Figure 3 for the location of this transect on the geological map of the Himalayas. Samples are indicated by "DH#" in the text. Isograds are dashed and labeled (grt=garnet; stau= staurolite). See figure 5 for a cross-section along A-A'.

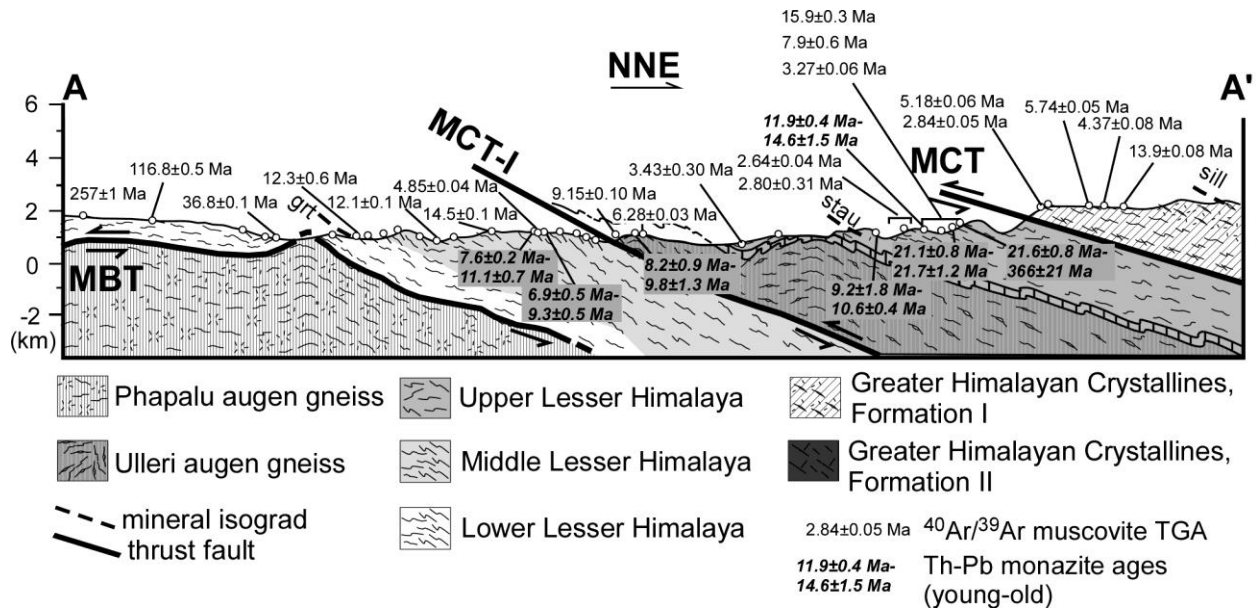


Figure 5. Cross-section across the Darondi Khola section showing available muscovite $^{40}\text{Ar}/^{39}\text{Ar}$ and Th-Pb ages after Catlos et al. (2001). See Figure 4 for line of section.

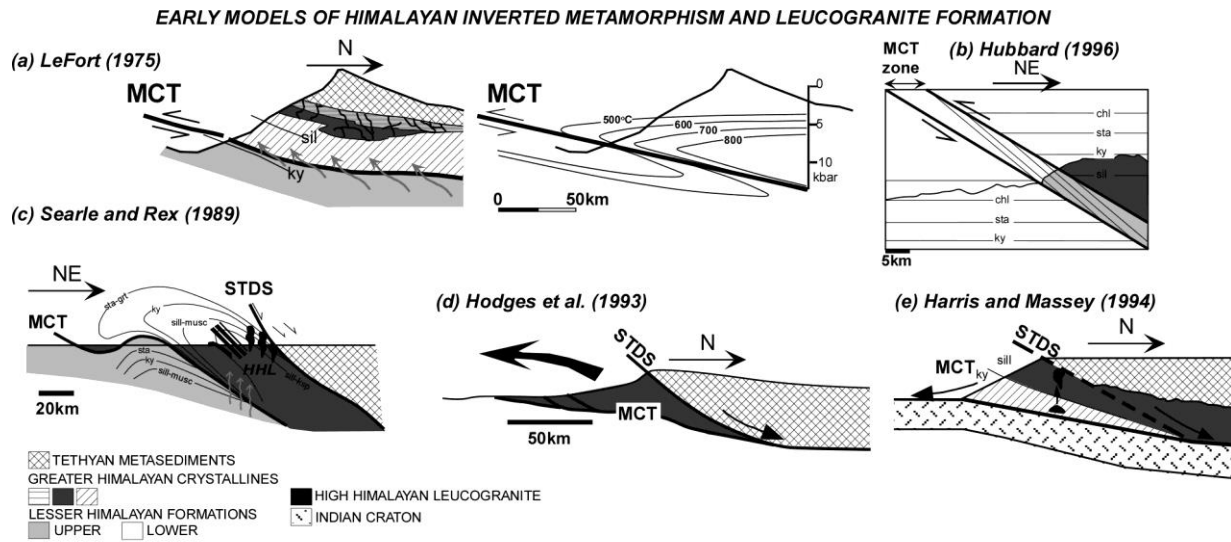


Figure 6. Cross-sections of early models of Himalayan inverted metamorphism and leucogranite formation. (A) The “hot-iron” model of LeFort 1975. (B) Juxtaposing right-way-up metamorphic isograds after Hubbard (1996). (C) A combination of models in panels (A) and (B) after Searle and Rex (1989). Wedge extrusion models after (D) Hodges et al. (1993) and (E) Harris & Massey (1994).

EARLY MODELS OF HIMALAYAN INVERTED METAMORPHISM AND LEUCOGRANITE FORMATION

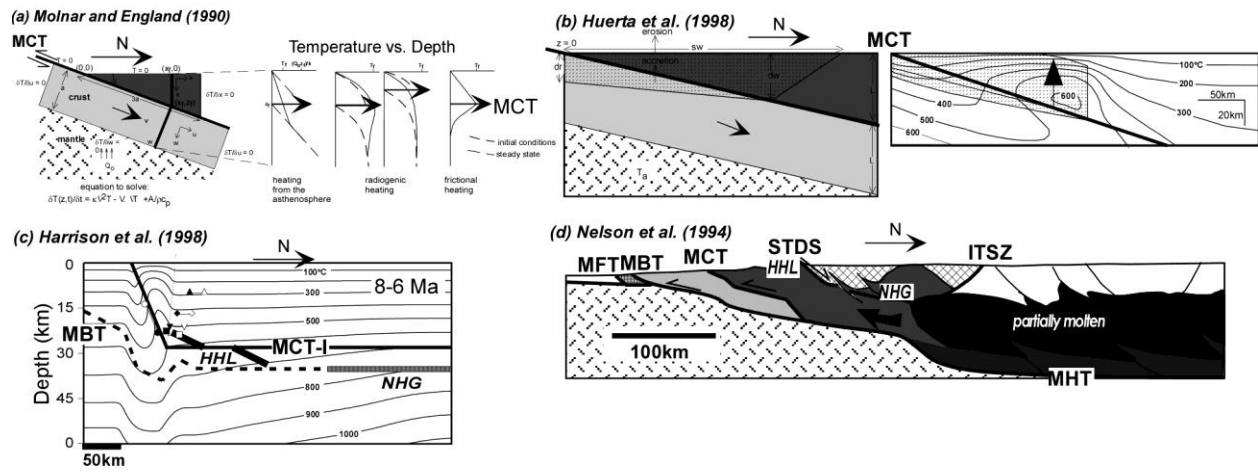


Figure 7. Cross-sections of early kinematic models of Himalayan inverted metamorphism and leucogranite formation. (A) After Molnar and England (1990). (B) After Huerta et al. (1998). (C) After Harrison et al. (1989). (D) After Nelson et al. (1996).

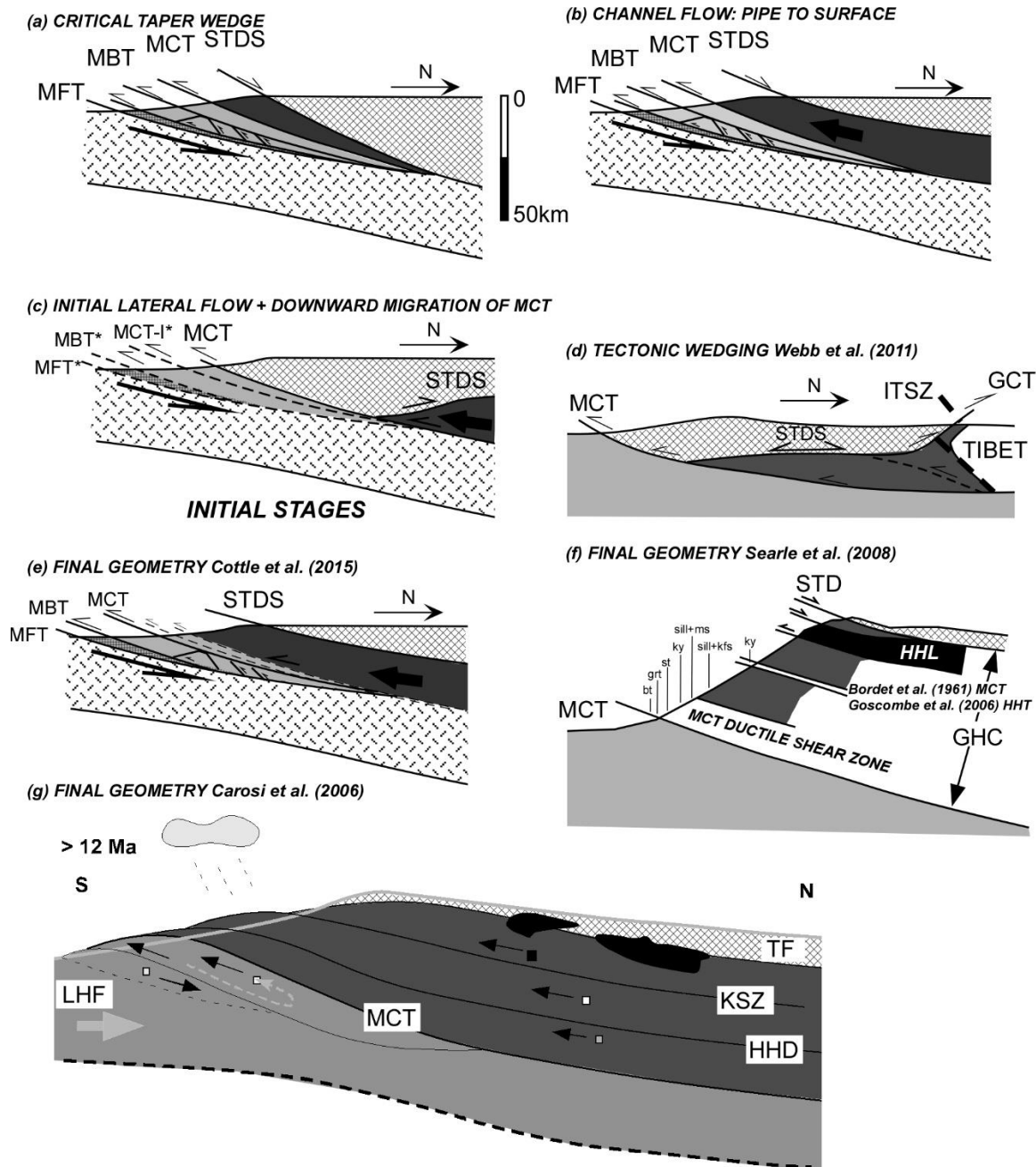
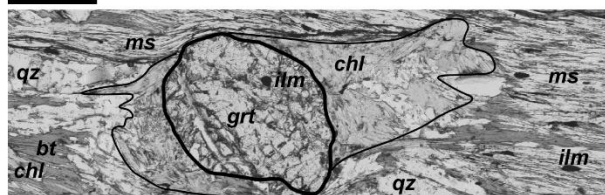
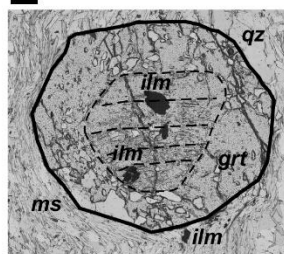


Figure 8. (A) An illustration of the critical taper model. (B) Schematic of channel flow and wedge extrusion. (C) A combination of critical taper and tectonic wedging of the GHC. A “*” indicates an incipient fault. (D) Illustration of GHC tectonic wedging after Webb et al. (2011). Panels (E) and (F) show the final geometry of the range, which has affected the position and definition of the MCT. Panel (G) showing the development of the MCT shear zone as rocks shown as squares within the footwall accrete to the hanging wall of the MCT. Faults within the GHC include the Kalopani shear zone (KSZ) and High Himalayan discontinuity (HHD). Panels (A), (B), (C), and (E) are after Cottle et al. (2015), panel (F) is after Searle et al. (2008), and panel (G) after Carosi et al. (2006).

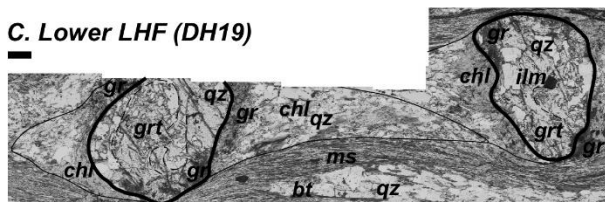
A. Lower LHF (DH17)



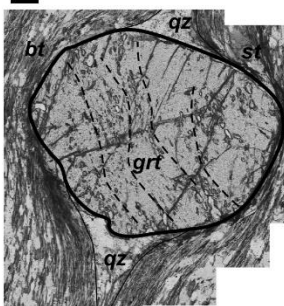
B. Mid-LHF DH30



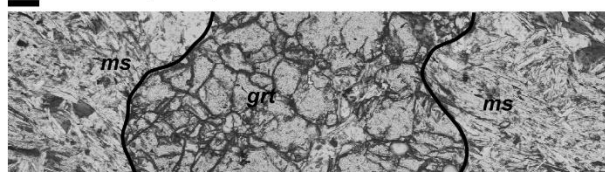
C. Lower LHF (DH19)



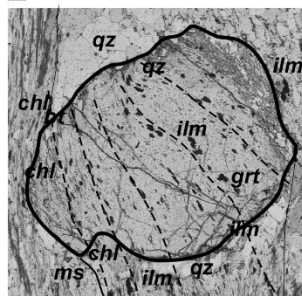
D. Mid-LHF (DH51)



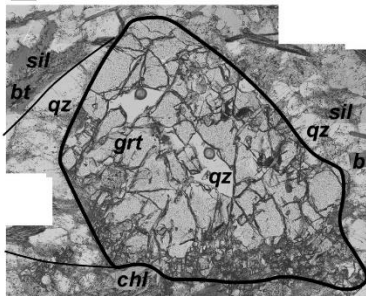
E. Mid-LHF (DH23)



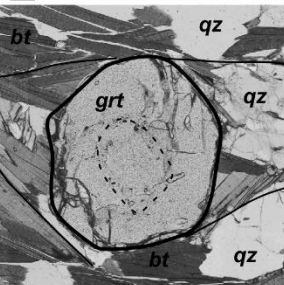
F. Mid-LHF DH75B



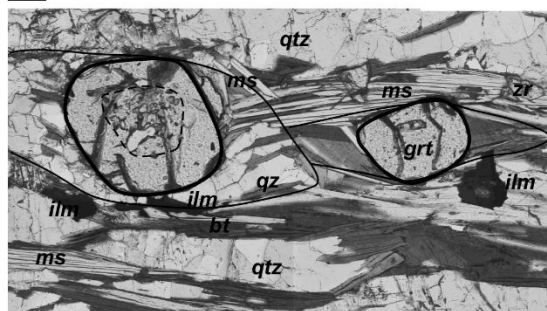
G. Upper LHF (DH58)



H. GHC (DH61)



I. GHC DH63



J. GHC DH67

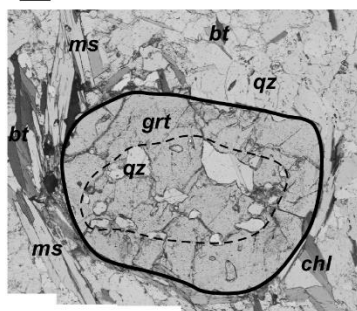


Figure 9. Selected petrographic (plane-polarized light) images of samples along the Darondi Khola showing the relationship of the garnet porphyroblasts and rock textures. Garnets are outlined using bold lines. Pressure shadows and inclusion trails are indicated by lighter and dashed lines, respectively. Mineral abbreviations after Whitney and Evans (2010). Panels are labeled with the sample numbers. The scale bar for each image is 200 μ m. See Figures 4 and 5 for sample locations. See supplementary files for this figure in color.

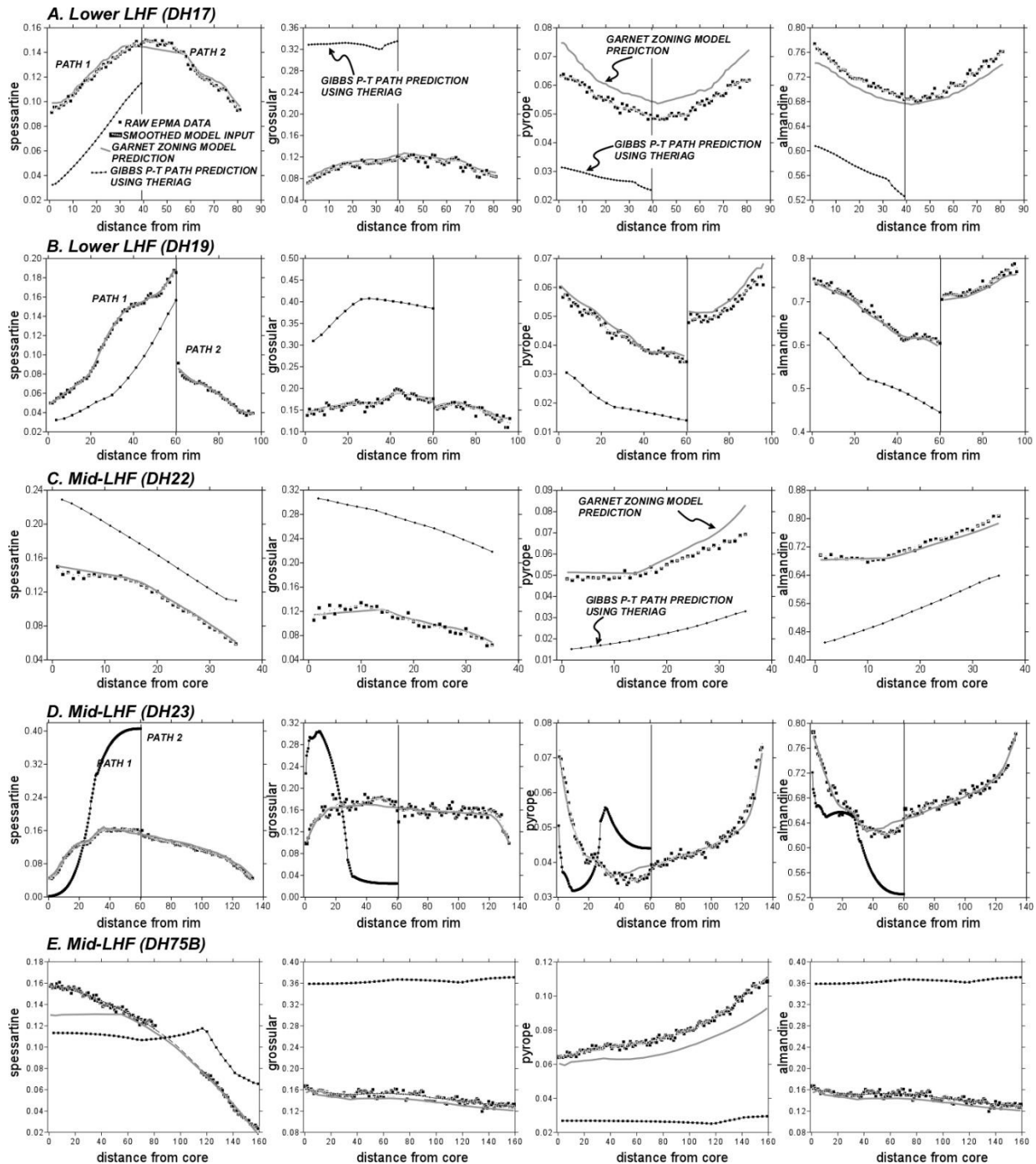


Figure 10. Compositional transects across garnets in lower LHF samples (A) DH17 and (B) DH19, and middle LHF samples (C) DH22, (D) DH23, and (E) DH75B. Distance is in analytical points, and the spacing between the points is $\sim 20\mu\text{m}$. The larger black squares are the raw electron microprobe data, whereas the smaller black squares near the EPMA data points are the smoothed data used for input into the model to generate the high-resolution P-T paths. The high-resolution P-T paths predict garnet zoning, which is shown by the bold gray lines. TheriaG was used to predict the garnet zoning for the Gibb's P-T paths, and these are also indicated.

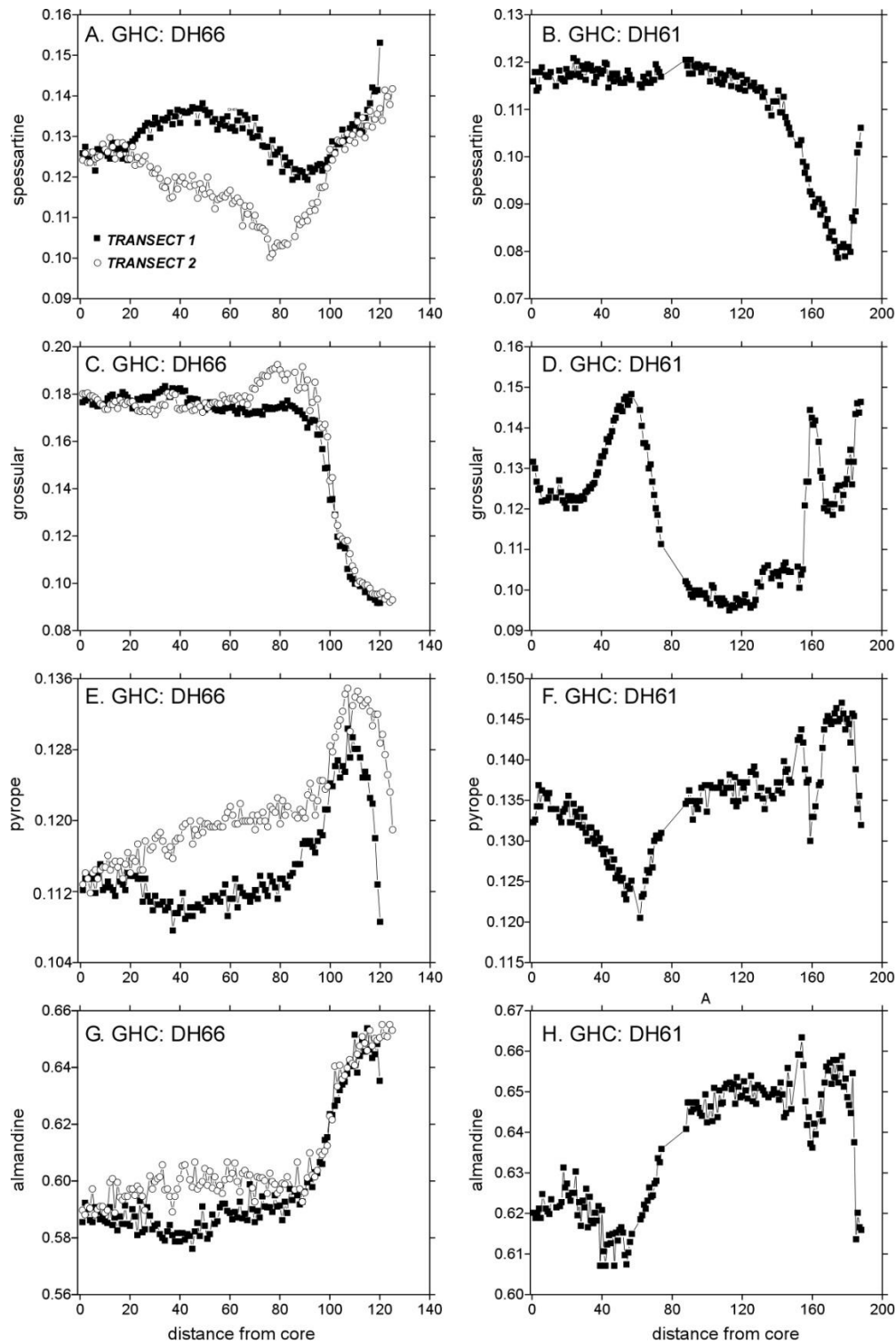


Figure 11. Compositional transects across garnets in GHC samples DH66 (two transects) in (A) spessartine, (C) grossular, (E) pyrope, and (G) almandine. Panels (B), (D), (F), and (H) are compositional transects in spessartine, grossular, pyrope, and almandine, respectively, across a garnet in sample DH61. Distance from the garnet core is in analytical points, and the spacing between the points is $\sim 20\mu\text{m}$.

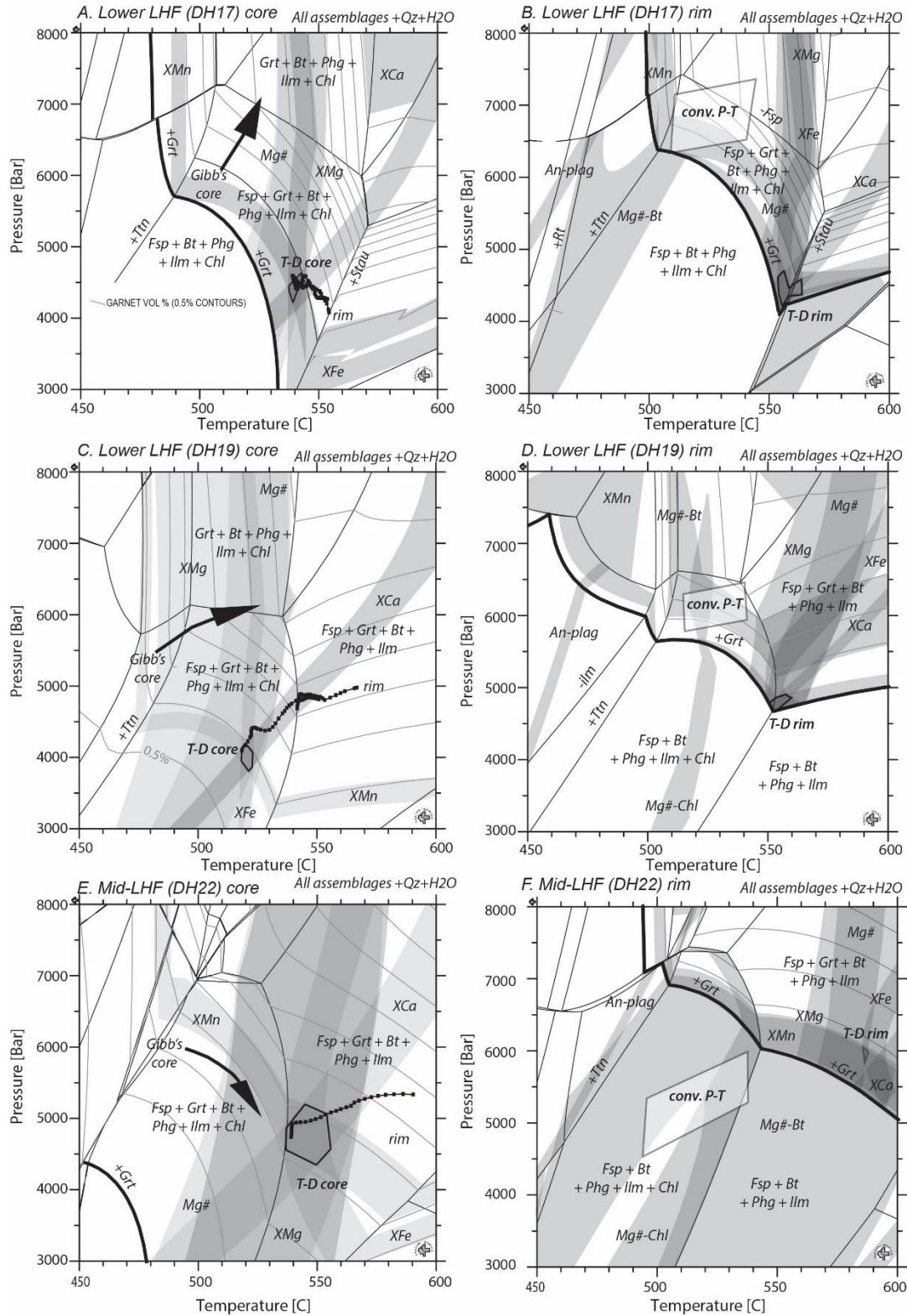


Figure 12. Isochemical phase diagrams from lower LHF samples DH17 (A) garnet core and (B) garnet rim, DH19 (C) core and D (rim), and mid-LHF sample DH22 (E) core and (F) rim. See text for entire figure caption.

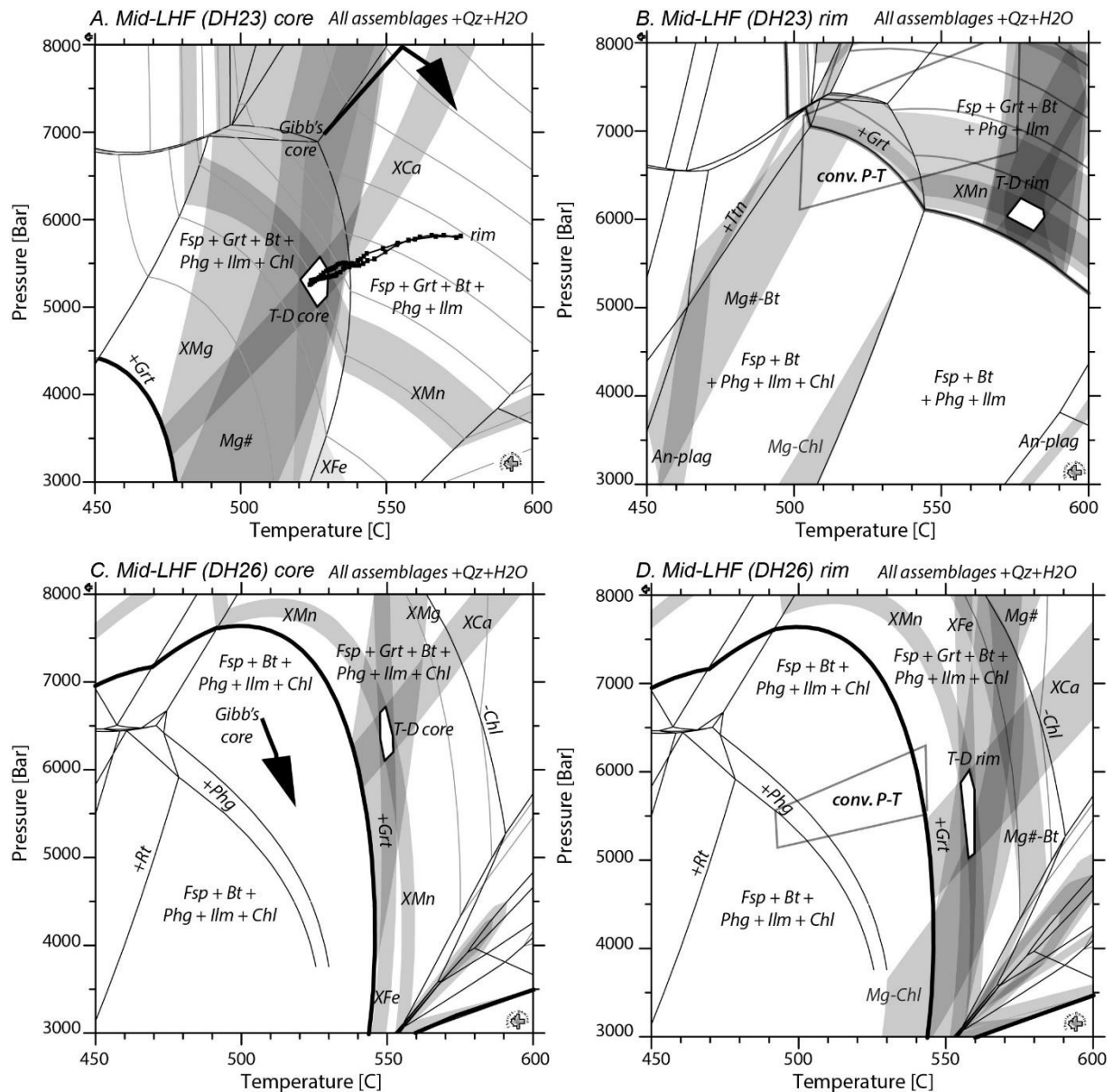


Figure 13. Isochemical phase diagrams from middle LHF samples DH23 (A) garnet core and (B) rim and DH26 (C) core and (D) rim. See Figures 4 and 5 for sample locations. Detailed caption is the same as in Figure 12. High-resolution P-T paths for sample DH23 were generated from two garnet core-to-rim transects after the approach of Moynihan & Pattison (2013). These are compared to the P-T paths obtained using the Gibb's method for the samples using the same data by Kohn et al. (2001). No data was available for the garnet transect for sample DH26, so a high-resolution P-T path was not created. In this case, the rock bulk composition (Table 3) was used for both core and rim panels.

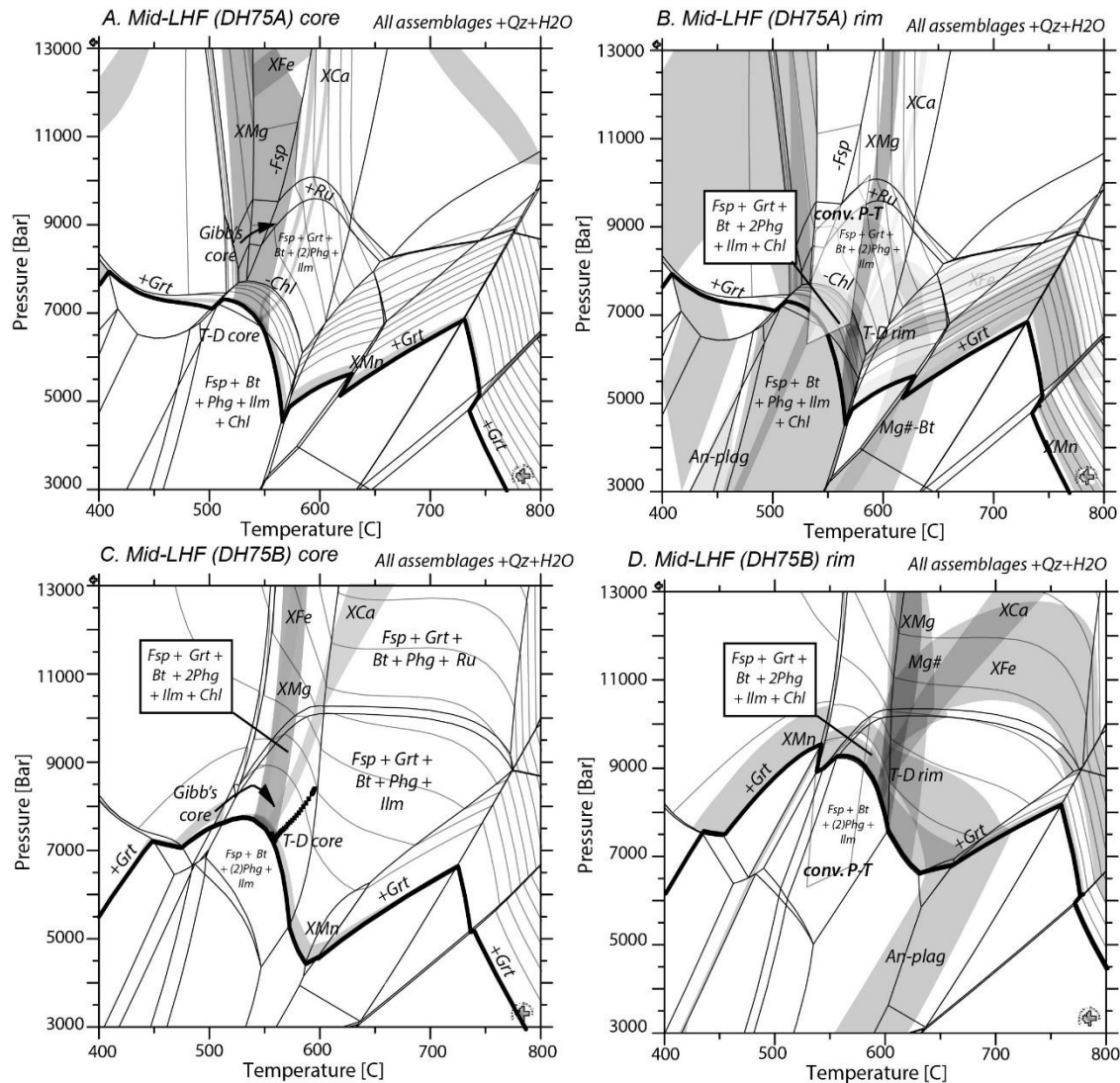


Figure 14. Isochemical phase diagrams from middle LHF samples DH75A (A) garnet core and (B) rim and DH75B (C) core and (D) rim. See Figures 4 and 5 for sample locations. Detailed caption is the same as in Figure 12. High-resolution P-T paths for sample DH75B were generated from garnet core-to-rim transects after the approach of Moynihan & Pattison (2013). These are compared to the P-T paths obtained using the Gibb's method for the samples using the same data by Kohn et al. (2001). The Gibb's path was also reported for sample DH75A. The starting point of the Gibb's P-T paths is labeled with "Gibb's core." The isochemical phase diagram for the garnet rim in sample DH75B was created using the final effective bulk composition generated by Theriak-Domino. In this case, isopleths for the garnet compositions reported for garnet rims are overlain on the diagram, as well as matrix mineral compositions isopleths for ± 0.01 An-content for plagioclase (Kohn et al. 2001). Intersecting isopleths are indicated by the polygon and labeled as "T-D rim." No data was available for the garnet transect for sample DH75A, so a high-resolution P-T path was not created, and the rock bulk composition (Table 3) was used for both core and rim panels. In the rim panels, data are compared to the conventional P-T conditions for the samples (grey polygon) using the same data reported by Kohn et al. (2001).

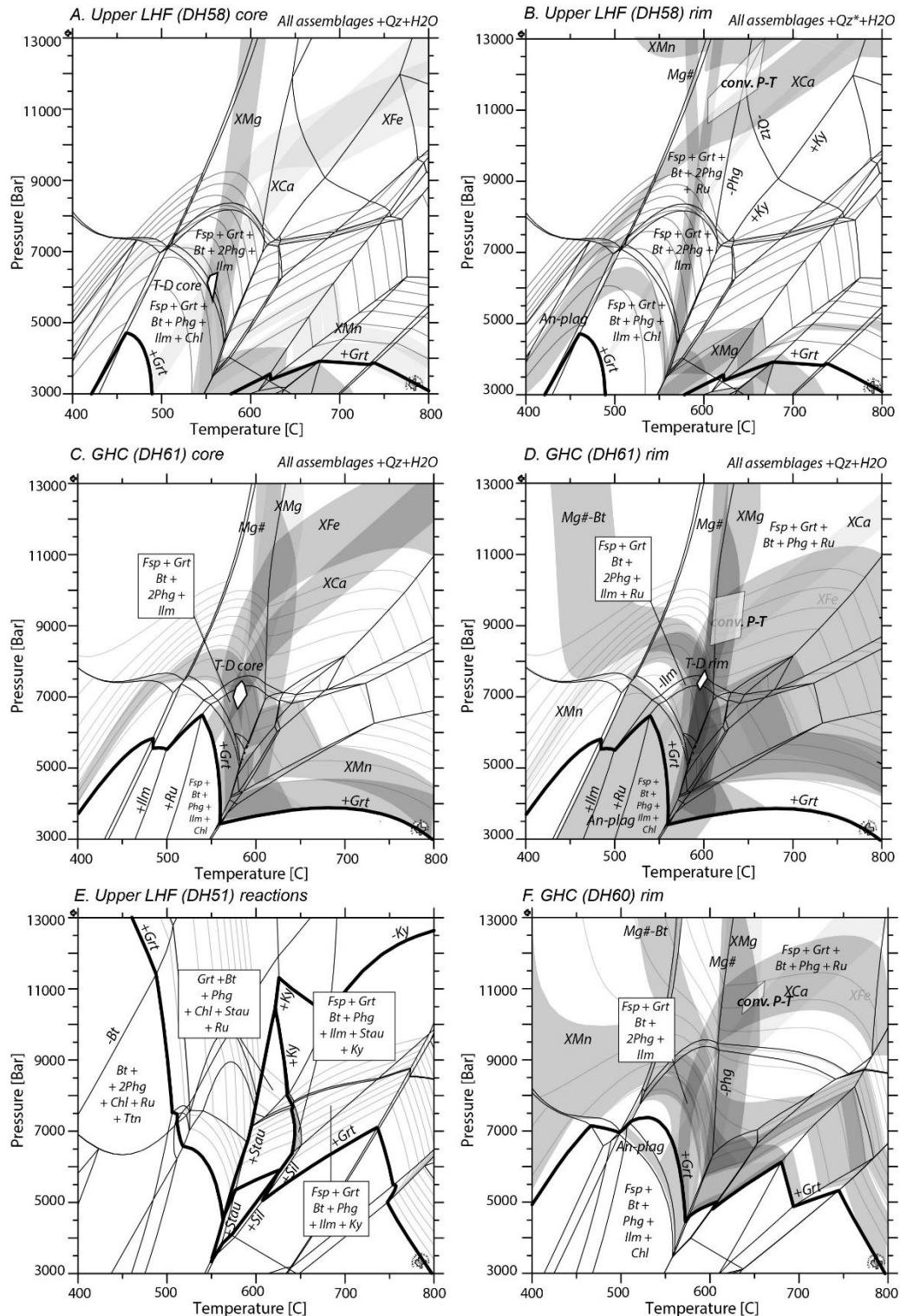


Figure 15. Isochemical phase diagrams from upper LHF samples DH58 (A) garnet core and (B) rim and (E) DH51 showing the mineral reactions only. The figure also includes isochemical phase diagrams from GHC sample DH61 (C) core and (D) rim, and DH60 (F) garnet rim data only. See text for detailed caption.

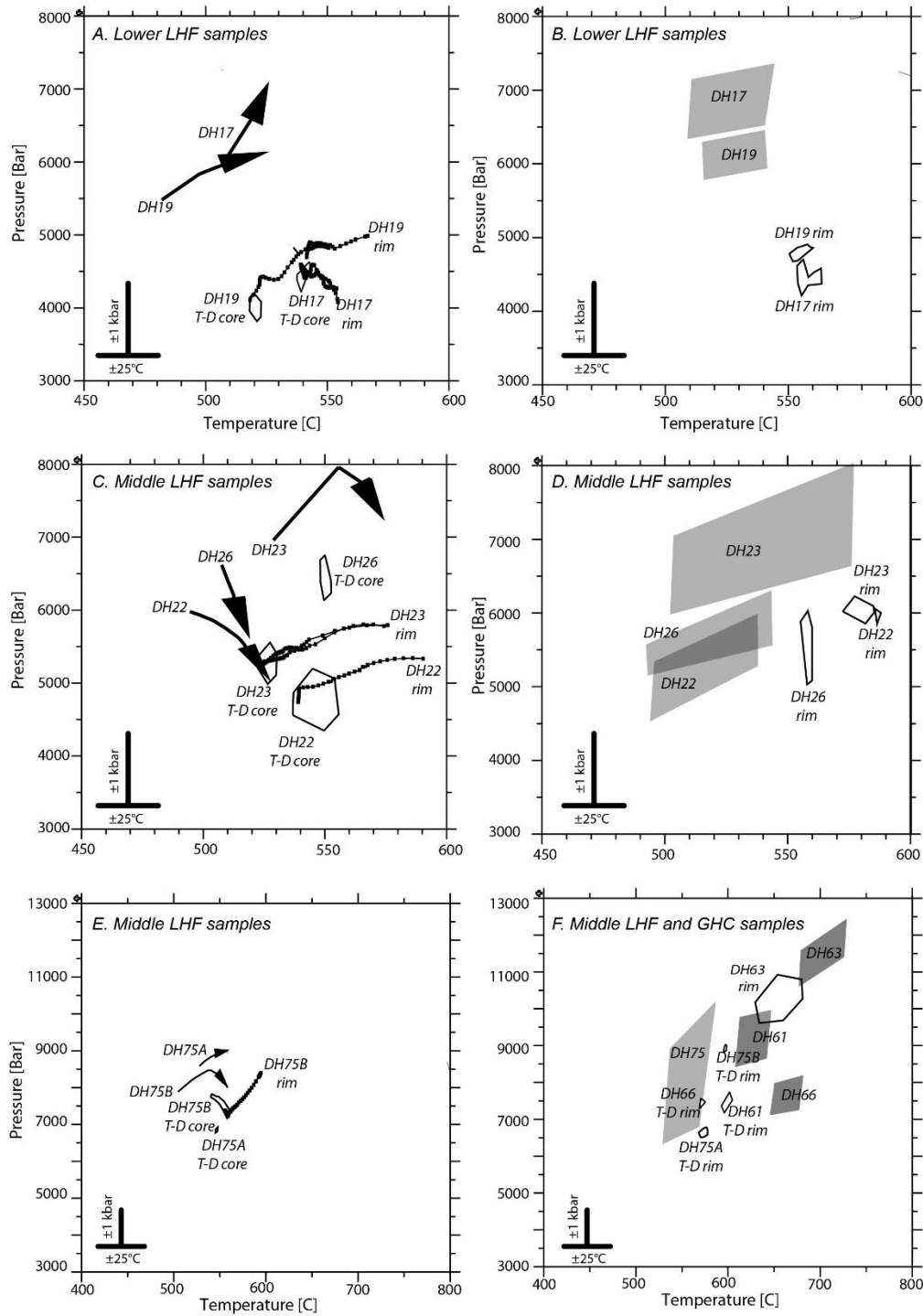


Figure 17. Summary of the P-T conditions and paths reported in Figures 12-16. In panels (A), (C), and (E), Gibb's P-T paths are shown as bold arrows and high-resolution P-T paths are labeled with core and rim points. In panels (B), (D), and (F), rim data generated using isopleth (white polygons) and conventional thermobarometry (grey polygons) are compared. Uncertainty scales in T ($\pm 25^\circ\text{C}$) and P (± 1 kbar) are shown as insets in each panel.

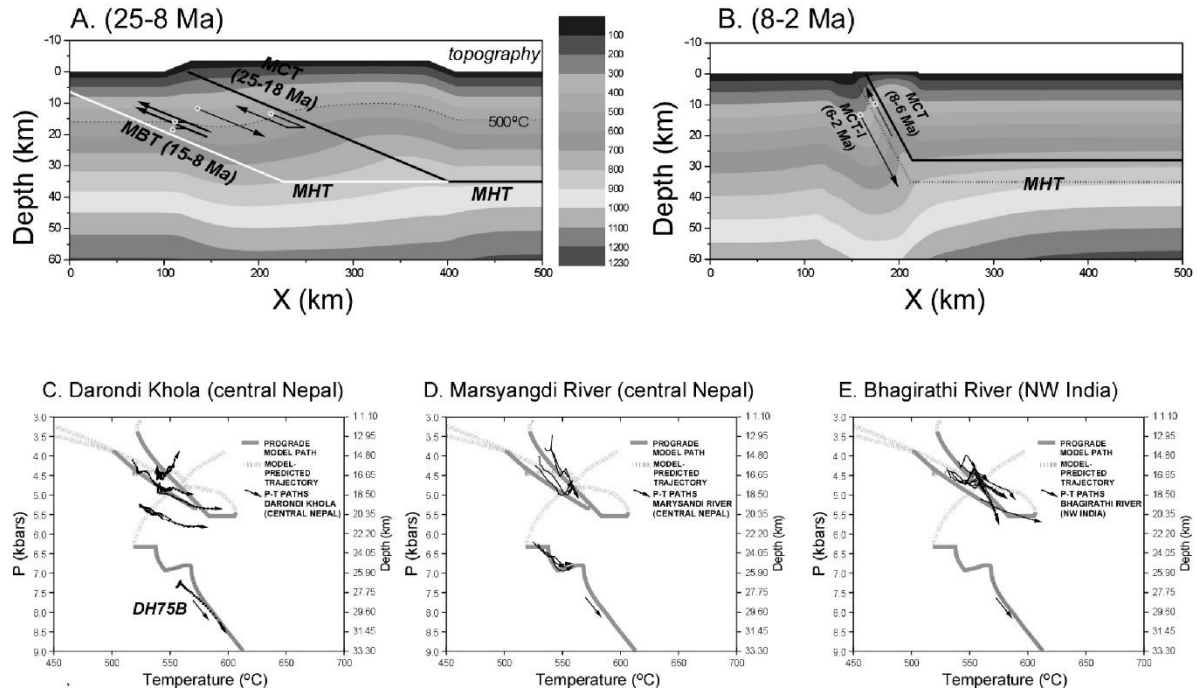
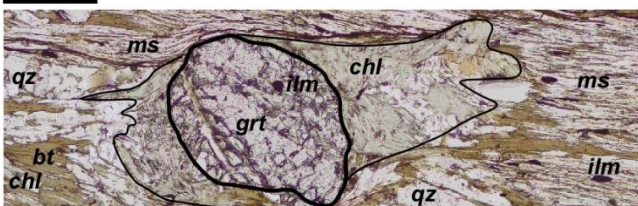
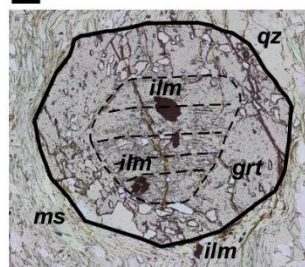


Figure 18. (A) Thermal-kinematic model cross-section after Catlos et al. (2018) showing the MCT (dark line) and MBT (white line) from 25 to 8 Ma. The MCT and MBT sole into the MHT at depth. Isothermal sections in degree increments are indicated by the scale bar. The isotherms show the thermal situation at 18 Ma after MCT slip. Example sample trajectories on the diagram are represented by arrows with dots at the initial and heads at the final position. The MCT is active from 25 to 18 Ma, whereas slip transfers to the MBT from 15 to 8 Ma. (B) The model cross-section of the reactivation of the MCT shear zone from 8 to 2 Ma. Both the MCT and MCT-I sole into the MHT at depth. This panel represents the thermal situation at 6 Ma right before the development of MCT shear zone inverted metamorphism. Example sample trajectories are shown. (C) P-T diagram showing the trajectories of the model predictions for samples panels A and B and high-resolution P-T paths for the Darondi Khola samples. Sample DH75B is identified. Panels (D) and (E) show the same model predictions but high-resolution P-T paths from the Marsyangdi River (Catlos et al., 2018) and Bhagirathi River transects (Catlos et al., 2020). See supplementary files for this figure in color.

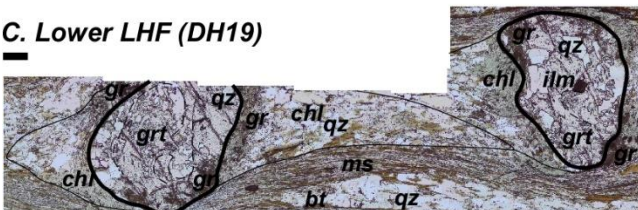
A. Lower LHF (DH17)



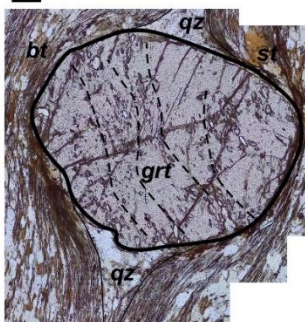
B. Mid-LHF DH30



C. Lower LHF (DH19)



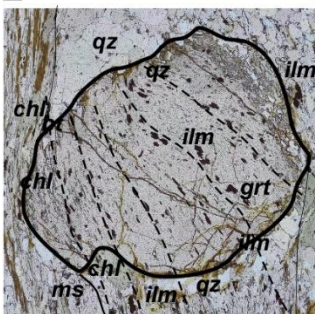
D. Mid-LHF (DH51)



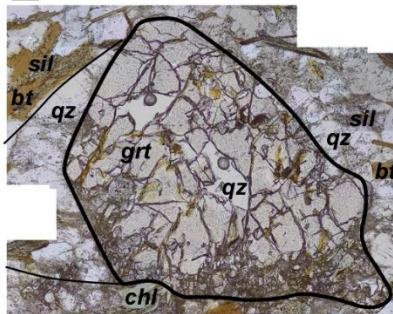
E. Mid-LHF (DH23)



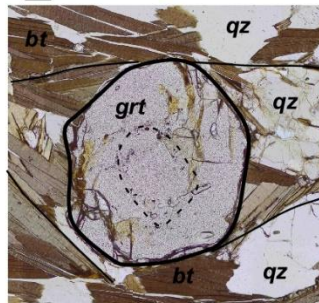
F. Mid-LHF DH75B



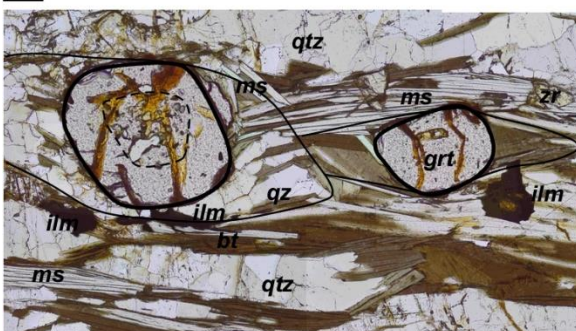
G. Upper LHF (DH58)



H. GHC (DH61)



I. GHC DH63



J. GHC DH67

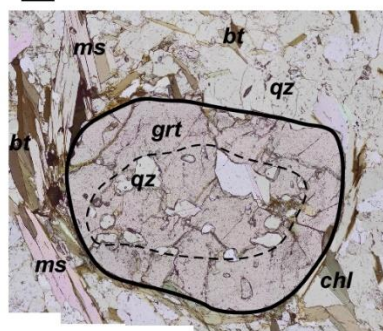


Figure S9. Selected petrographic (plane polarized light) images of samples along the Darondi Khola showing the relationship of the garnet porphyroblasts and rock textures. Garnets are outlined using bold lines. Pressure shadows and inclusion trails are indicated by lighter and dashed lines, respectively. Mineral abbreviations after Whitney and Evans (2010). Panels are labeled with sample number. The scale bar for each image is 200 μm . See Figures 4 and 5 for sample locations.